Techniques for the Analysis and Understanding of Cosmic Evolution

by

Matthew John Kolopanis

A Dissertation Presented in Partial Fulfillment
of the Requirements for the Degree
Doctor of Philosophy

Approved March 2018 by the
Graduate Supervisory Committee:

Judd Bowmann, Co-Chair
Philip Mauskopf, Co-Chair
Ralph Chamberlin
Cecillia Lunardini
Tanmay Vachaspati

ARIZONA STATE UNIVERSITY

May 2018

ABSTRACT

The Cosmic Microwave Background (CMB) has provided precise information on the evolution of the Universe and the current cosmological paradigm. The CMB has not yet provided definitive information on the origin and strength of any primordial magnetic fields or how they affect the presence of magnetic fields observed throughout the cosmos. This method searches for Faraday Rotation (FR) and specifically uses polarized CMB photons as back-light to cross-correlate with pre-existing rotation measure (RM) maps. This cross-correlation is an alternative approach compared to many optimal single- and multi-frequency power spectrum estimators. I find that current generation CMB experiments may be not sensitive enough to detect FR but next generation experiments should be able to make highly significant detections. Identifying FR with the CMB will provide information on the component of magnetic fields along the line of sight of observation.

The 21cm emission from the hyperfine splitting of neutral Hydrogen in the early universe is predicted to provide precise information about the formation and evolution of cosmic structure, complementing the wealth of knowledge gained from the CMB.

21cm cosmology is a relatively new field, and precise measurements of the Epoch of Reionization (EoR) have not yet been achieved. In this work I present 2σ upper limits on the power spectrum of 21cm fluctuations ($\Delta^2(k)$) probed at the cosmological wave number k from the Donald C. Backer Precision Array for Probing the Epoch of Reionization (PAPER) 64 element deployment. I find upper limits on $\Delta^2(k)$ in the range $0.3 < k < 0.6h$ Mpc^{-1} to be (650 mK)^2, (450 mK)^2, (390 mK)^2, (250 mK)^2, (280 mK)^2, (250 mK)^2 at redshifts $z = 10.87$, 9.93, 8.91, 8.37, 8.13, and 7.48 respectively.

Building on the power spectrum analysis, I identify a major limiting factor in detecting the 21cm power spectrum. This work is concluded by outlining a metric to

evaluate the predisposition of redshifted 21cm interferometers to foreground contamination in power spectrum estimation. This will help inform the construction of future arrays and enable high fidelity imaging and cross-correlation analysis with other high redshift cosmic probes like the CMB and other upcoming all sky surveys. I find future arrays with uniform (u, v) coverage and small spectral evolution of their response in the (u, v, f) cube can minimize foreground leakage while pursuing 21cm imaging.

To my loving and supportive wife Krista.

ACKNOWLEDGMENTS

The fallacious assumption this work is the result of my personal research and experience would do great injustice to every person which has helped me throughout my studies.

I foremost would like to thank Philip Mauskopf for introducing me to the world of sub-millimeter astronomy and cosmic microwave background research.

This work would not have been possible without Judd Bowmann who's continued support and trust has allowed me to fulfill these research endeavors.

I would especially like to thank Daniel C. Jacobs who has acted as guide and mentor in the wonderful world of HI intensity mapping and radio astronomy.

I would like to extend my gratitude to Adam Beardsley, Bryna Hazelton, and Miguel Morales who have provided continual and enlightening conversations and support in my research into imaging based 21cm power spectrum. Without their unique insights and experience my final chapter and project concerning the optimization of radio arrays would not be possible.

This work would not have been possible without the help and support of the PAPER and HERA teams, including: James Aguirre, Adam Beardsley, Chris L. Carilli, Carina Cheng, Joshua S. Dillon, Bryna Hazelton, Piyanat Kittiwisit, Saul Kohn, Joshua Kerrigan, Adam Lanman, Adrian Liu, Miguel Morales, Aaron Parsons, Jonathon Pober,and many others.

Finally the experience and world of graduate studies would not have been as wonderful and informative without my lab and office partners at Arizona State University: Jacob Burba, Michael Busch, Edward Buie II, J'Neil Cottle, Francis Duplessis, Samuel Gordon, Jeff Hyde, Hank Lamm, Nivedita Mahesh, Jayden Newstead, Genady Pilyavsky, and Nithyanandan Thyagarajan.

TABLE OF CONTENTS

LIST OF TABLES

LIST OF FIGURES

PREFACE

This dissertation is the collection of works done and on going research towards the advancement of understanding cosmic evolution. My experiences have varied from studying the imprint of large scale magnetic fields on the cosmic microwave background (CMB) to searching for the 21cm line emitted by neutral Hydrogen to probe structure formation and the universal transition from neutral to ionized gas known as the Epoch of Reionization (EoR). The knowledge and comsic evolution probed by these phenomena span from the very beginning of the universe up to through the first Gyr of cosmic history. The interactions of matter and energy during this relatively short period formed the basis for information impacted onto the distribution and statistical properties of galaxies we observe today.

My research is presented in cosmological chronological order.

The work begins with a study of a new technique which measures the Faraday Rotation (FR) in CMB photons propagating through the plasmas of the early universe and those created in our own Galaxy[1]. Detecting and characterizing Faraday Rotation would probe the structure of cosmic magnetic fields oriented along the light of sight towards the observer. Previous studies have focused on an estimator based on the polarized power spectrum, but in this work I investigate how Faraday Rotation manifests in map space and searches for correlations between different polarized maps. A new cross-correlation estimator is introduced and the prospect of detecting Galactic Faraday Rotation for current CMB experiments is discussed. Due to the small amplitude of the Faraday Rotation signal, it is expected that this correlation

---

[1]This chapter comes from a published work: Kolopanis, M., P. Masukopf and J. Bowmann "Detectability of Galactic Faraday Rotation in multiwavelength CMB observations", MNRAS**473**, 4795-4804 (2018).

should be weakly detectable by next generation arrays and a strong detection should be possible by a telescope like the CMB-S4 (a next generation all sky CMB experiment expecting high sensitivity and high spatial resolution).

The focus of this document then moves forward in cosmic time. No longer studying the CMB photons from the early universe but instead on the 21cm photons emitted from neutral Hydrogen after recombination. Traveling over vast cosmic distances, these photons are redshifted to meter wavelengths as observed from Earth. The radio telescopes built to search for these photons and the spatial and spectral fluctuations of their signal (similar to CMB anisotropies) are commonly interferometers. One such radio interferometer focused on in this work is the Donald C. Backer Precision Array for Probing the Epoch of Reionization (PAPER). Detecting the power spectrum from reionization would help constrain the types of luminous bodies which caused the pervasive neutral Hydrogen to globally re-ionize for the first time since recombination. The latest upper limits on the power spectrum from reionization from PAPER across multiple redshift bands is the next chapter of this work.

One lesson learned from current generation experiments is the array design (both the antenna placement and shape of the primary beam) strongly influences how foregrounds mix with the cosmological background. Looking to the future, arrays designed to image the epoch of reionization must achieve a high dynamic range of foreground isolation to properly disentangle the two signals. The last work presented here outlines a method used to quantify the amount of inherent contamination in power spectrum estimation for a given array configuration. Minimizing inherent foreground contamination eases the analytical challenges associated with detecting the power spectrum from the EoR, making maps of the evolution of neutral Hydrogen, and enables cross correlation with other surveys at high redshifts.

Chapter 1

INTRODUCTION

How complex cosmic structure emerges from the mostly uniform and smooth distribution of matter and energy after the Big Bang is one of the most exciting and difficult questions to answer in cosmology and astrophysics. The precise study of the Cosmic Microwave Background (CMB) over the past 50 years has been a powerful tool to help answer this question. The small density fluctuations which seeded the gravitational collapse of cosmic hydrogen to form these structures, and the effects of evolving cosmic structure, are imprinted on CMB photons.

Continued studies of the CMB are hoping to shed further light on both the intricate physics occurring during the first moments of the universe and the small perturbations in the CMB from interactions with cosmic structures. These photons, however, cannot be the only tool used to study the evolution of the universe since they provide almost no information on the times between recombination and reionization.

The 21cm emission from the hyperfine splitting of hydrogen provides a unique perspective on structure formation, especially near the end of the cosmic dark ages when the Epoch of Reionization (EoR) occurred. This radiation is predicted to exist even during the cosmic dark ages as an absorption signal After decoupling from the CMB, cosmic hydrogen is predicted to absorb 21cm photos during the cosmic dark ages; allowing for the study of a large volume of space-time even before the 21cm signal moves into emission.

1.1 The Cosmic Microwave Background

1.1.1 Physics of the CMB

The small scale density fluctuations on the mostly uniform structure of the CMB are known as anisotropies. CMB anisotropies can be categorized into one of two groups: primary and secondary anisotropies. A primary anisotropy refers to a physical interaction happening at or before the surface of last scattering. The surface of last scattering is the time when photons decouple from baryonic matter and neutral atoms form. Conversely, secondary anisotropies are any interaction which occurs to a CMB photon between the surface of last scattering and when it is observed.

The study of primary anisotropies provides insights on the primordial state of the universe; defining the current cosmological paradigm.

Compton Scattering couples photons and baryons in the early universe (before recombination; z > 1100) into what is often referred to as a photon-baryon fluid (Hu, 1996). An in depth discussion of the dynamics of this fluid is found in Hu 1996, Hu and White 1997b. Here we provide and overview of the some of the major interactions in the photon-baryon fluid resulting in its characteristic shape and polarization of the CMB photons.

1.1.1.1 Baryon Acoustic Oscillations

The short time between individual Compton scatter events corresponds to an optically thick universe and is exploited in Hu 1996, Peebles and Yu 1970 and Hu and

Sugiyama 1994 in order to write the equation of motion of the temperature of the photons to first order as:

$$\frac{d}{d\eta}(1+R)\dot{\Theta}_0 + \frac{k^2}{3}\Theta_0 = -\frac{k^2}{3}(1+R)\Psi - \frac{d}{d\eta}(1+R)\dot{\Phi} \tag{1.1}$$

Where η in the conformal time, and dots correspond to derivatives with respect to η. Θ_0 is the isotropic temperature fluctuation, Ψ is the gravitational potential, Φ is the potential of perturbative space curvature, R is the ratio of the the photon and baryon momenta, and k corresponds to a Fourier mode.

This equation can again be approximated by ignoring the time dependence of the two potentials and the momentum ratio R, and defining the sound speed in the fluid as $c_s = \frac{1}{\sqrt{3(1+R)}}$:

$$\ddot{\Theta}_0 + k^2 c_s^2 \Theta_0 = -\frac{1}{3}k^2\Psi \tag{1.2}$$

This is a simple harmonic oscillator with a gravitational driving term. The gravitational potential is dominated by the contribution from dark matter. As a result, these spherical harmonic oscillators coalesce around dark matter over-densities. The initial condition $\dot{\Theta}_0(0) = 0$ is attributed to lockout of spatial modes during inflation. The first order solution to the temperature fluctuations are then:

$$\Theta_0(\eta) \sim (\Theta_0(0) + (1+R)\Psi)\cos{(kc_s\eta)} - (1+R)\Psi \tag{1.3}$$

It is convenient to define the effective (observed) temperature field, $\Theta + \Psi$. It is the cumulative effect of the temperature perturbations and any gravitational Doppler shifts on the photons. The observed temperature can be written:

$$[\Theta_0 + (1+R)\Psi](\eta) \sim (\Theta_0(0) + (1+R)\Psi)\cos{(kc_s\eta)} \tag{1.4}$$

3
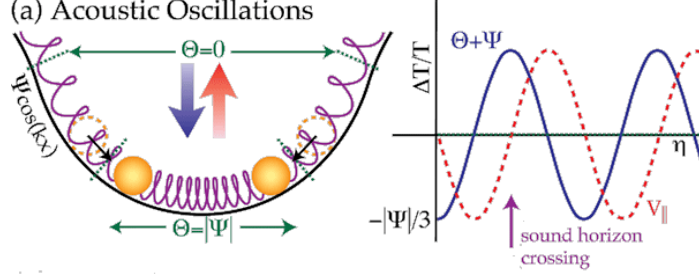
Figure 1: Visual representation of Baryon Acoustic Oscillations. Image adapted from Hu (1996).

While the approximation of static potentials only holds in regimes where non-relativistic matter dominates the equation of state (Hu, 1996), this gives an intuitive, first order understanding of the motion of the photon-baryon fluid. Gravitational over-densities drives the fluid to collapse and photon pressure acts as a restorative force on the fluid. The combination of these effects is an oscillator. Figure 1 provides a visual representation of this effect as seen in Hu (1996).

The resonances of these oscillations are imprinted in CMB during recombination on size scales $\theta \sim \lambda/D(z)$ where D(z) corresponds to the comoving distance from the observer to redshift z, and λ refers to the wavelength of the inhomogeneity of the temperature field Θ_0. This relation also holds in Fourier space: $\ell \sim D(z)k$. Following the work of Hu (1996), the size can be approximated in the regime assumed above.

Determining where local maxima and minima in the observed temperature occur is the crucial step in finding the angular size of these features. These extrema in Equation 1.4 coincide with the extrema of the cosine term, namely $k_n = n\pi/s_*$. Here n is an integer and $s_* = \eta_*/\sqrt{3}$ is the distance sound can travel by recombination. The distance to recombination: $D(z_*)$ or $D_* = \eta_0 - \eta_* \approx \eta_0$ where $\eta_0 = \eta(z = 0)$. In a flat matter dominated universe, $\eta \approx (1 + z)^{-1/2}$. The corresponding size scale is then:

$$\ell_n \approx \eta_0 \frac{n\sqrt{3}\pi}{\eta_*} \sim n\pi\sqrt{3}\sqrt{1 + z_*} \tag{1.5}$$

4

Recombination occurs near $z_* \sim 1100$, this corresponds to $\ell_1 \approx 200$ for the first spectral peak in Fourier space ($\ell_{n=1}$) or $2°$ on the sky. These approximations are validated by observing the first acoustic peak in seen in Figure 5 does indeed occur at $\ell \approx 200$.

1.1.1.2 Thompson Scattering and Damping

In regions of the photon-baryon fluid where the universe can become optically thin, it is possible for "slippage of photons past baryons" to occur (Hu, 1996, Hu and White, 1997a). This "slippage" dissipates some of the primordial fluctuations at small angular scales and results from a shear viscosity and heat conduction in the photon-baryon fluid (Weinberg, 1971).

The exact form of the damping can be found in Hu (1996), where it is shown that the oscillations are dampened by a factor $e^{-k^2 \frac{\dot{\tau}}{\eta}}$. Here the differential optical depth: $\dot{\tau} = n_e \sigma_T a$, where n_e is the electron number density, σ_T the Thompson Scattering cross-section, and a is the scale factor.

The photons in this optically thin region, and also where a temperature quadrapole anisotropy exists, can undergo Thompson scattering to result in a net linear polarization (Hu and White, 1997a, Kosowsky, 1999). A graphic representation of this effect is shown in Figure 2. The quadrapole temperature anisotropy originates from gradients in the photon fluid velocity and the resulting Thompson Scattering actually acts to destroy this gradient (Hu and White, 1997a,b). The combined effects result in a net linear polarization at a level of 10% compared to the scale of the temperature fluctuations Hu and White (1997a).

As discussed in Hu and White (1997a), the scalar temperature perturbations
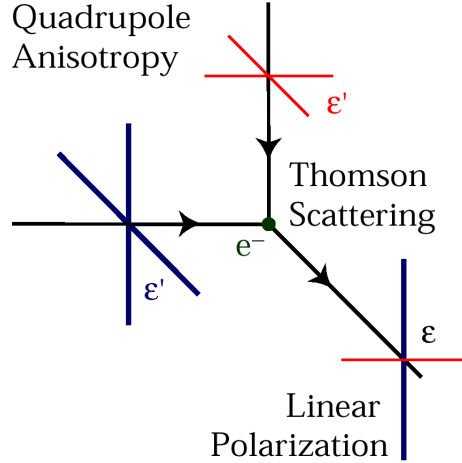
Figure 2: An illustration of linear polarization resulting from Thompson Scattering in a quadrapolar anisotropy. Thick and thin lines represent hot and cold radiation, respectively. Image adapted from Hu and White (1997a)

resulting in Thompson scattering create predominantly E-mode polarization. E-mode polarization is defined as a pattern whose spherical harmonic decomposition have parity $(-1)^{\ell}$. This is discussed further in Appendix A

For an extended analysis of primordial perturbations and primary anisotropies refer to Hu (1996), Hu and White (1997a,b), Hu and Dodelson (2002).

1.1.1.3 Secondary Anisotropies

As stated above, secondary anisotropies are the results of interactions CMB photons have with cosmic structure between when they decouple during recombination and when they are observed at the present day.

The dedicated study of these foreground interactions can provide knowledge on the evolution of the gravitational fields of structure through lensing (Blanchard and Schneider, 1987) and the Integrated Sachs-Wolfe effect (Sachs and Wolfe, 1967).
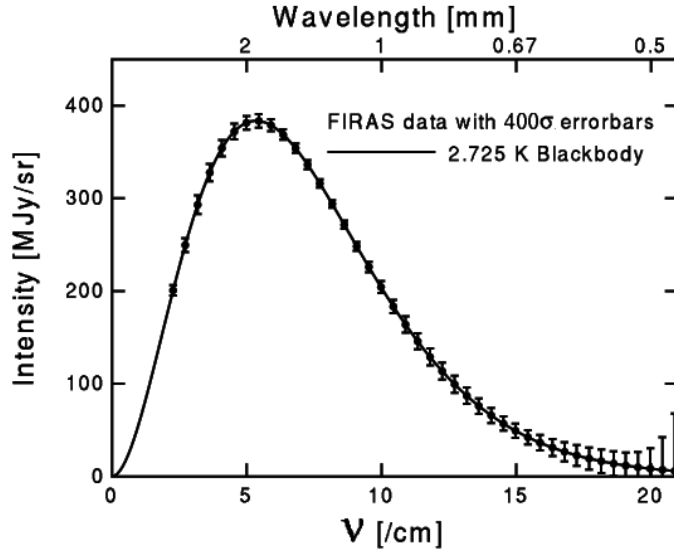
Figure 3: FIRAS data of CMB blackbody spectrum. Data deviates from model by less than 0.03%. Note error bars are 400σ (Mather *et al.*, 1994). Figure courtesy of Edward Wright (UCLA).

Properties of ionized regions (temperature, bulk velocity, etc) can also be discerned from studying interactions like the Sunyaev-Zeldovich effect (Sunyaev and Zeldovich, 1972).

Large scale ionized regions can even create a second source of polarized photons in the CMB. The combination of the Doppler effect and an additional quadrapole anisotropies in CMB photons from locally hot and cold regions enter ionized areas (Hu and White, 1997a, Hu, 2000). This is most prominent during the Epoch of Reioinzation (EoR) when the intergalactic medium ionizes for the first time since recombination (Reichardt, 2015, Blanchard and Schneider, 1987)

1.1.2   CMB Detection History

Having developed some background on the physics of the CMB and how it interacts with cosmic structure through magnetic fields, we turn our attention to the major developments in its detection.

The initial flight of COBE in 1994 provided the first detection of anisotropies at a scale of 10^{-5} in the CMB. It also detected the CMB as a near perfect black body at a temperature of $2.726 \pm .010\ K$ with a 95% confidence level (Mather *et al.*, 1994). The CMB flux as a function of wavelength as observed by the COBE FIRAS instrument is shown in Figure 3. Note in this figure, the data is show with 400σ errorbars and deviates from the model of a blackbody by less than 0.03%.

After this detection by COBE, multiple ground and balloon based experiments began attempting to precisely characterize the anisotropies in the CMB power spectrum. These experiments include but are not limited to: DASI (Halverson *et al.*, 2002), MAXIMA (Hanany *et al.*, 2000), BOOMERANG (de Bernardis *et al.*, 2000), CBI (Padin *et al.*, 2001), and Archeops (Benoit *et al.*, 2003).

Many experiments presented limits on the acoustic peaks in the CMB power spectrum, but the first major agreement between experiments on the amplitude and position of the first peak occurred near 2002 from the findings of DASI, BOOMERANG, MAXIMA, and the CBI. The findings from these experiments is illustrated in Figure 4. Errorbars denote 1σ uncertainty in this image.

Our understanding of the CMB continues to improve as more precise all sky maps are created by WMAP as recently as 2013 (Bennett *et al.*, 2013) and the PLANCK satellite beginning in the same year and as recently as 2015 (Planck Collaboration *et al.*, 2016a). These all sky maps provide a wealth of information for the large scale
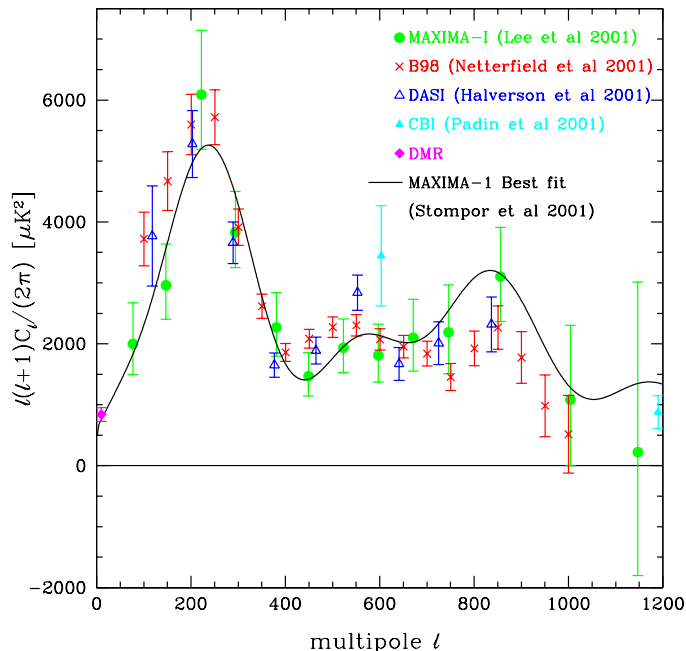
Figure 4: Detections of the CMB angular power spectrum from DASI, BOOMERING, MAXIMA, CBI and COBE. These detections are the first to show good agreement on the position and amplitude of the first angular peaks. Errorbars represent 1σ uncertainty. Image adapted from Stompor *et al.* (2001), Lee *et al.* (2001)

anisotropies (low ℓ) of the CMB, while ground based telescopes continue to gather information on the extremely small scale (high ℓ) structure.

The current cosmological paradigm is reviewed in detail in (Planck Collaboration *et al.*, 2016e). Here we provide an overview of the current paradigm and its as seen through PLANCK. The best fit models of the CMB include a universe dominated by a cosmological constant (Λ) and whose matter consists primarily of non-interacting (cold) dark matter. The so called standard ΛCDM cosmological model fit to PLANCK 2015 data is displayed in Figure 5 and the polarization power spectrum and temperature-polarization cross power spectrum are displayed in Figure 6.

The expansion of the universe, according to the laws of general relativity, is

9
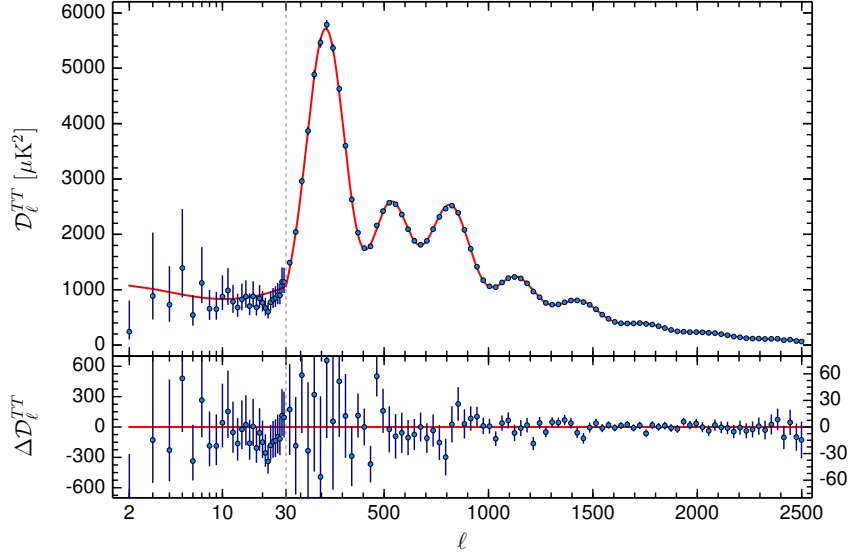
Figure 5: Temperature auto power spectrum of the CMB. Over plot is the best fit model and deviations of PLANCK temperature data. Here $D_\ell = \frac{\ell(\ell+1)}{2\pi}C_\ell$. Image from Planck Collaboration *et al.* (2016a)
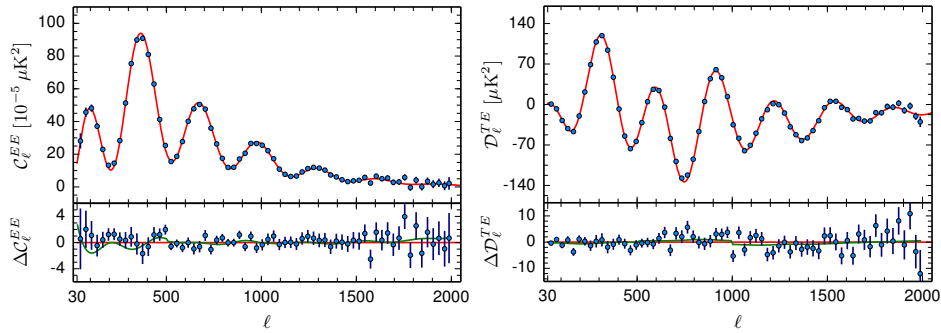
Figure 6: Left: Planck EE auto power spectrum with best fit model overplot and deviations below. Right: TE (temperature E-mode) cross power spectrum from planck 2015 with best fit model overplot and deviations below. Images from Planck Collaboration *et al.* (2016a)

expressed dynamically in terms of the scale factor, $a(t)$, which is set to 1 at present day. The Hubble constant, $H_0 = 100h$ km sec^{-1} Mpc^{-1}, describes the rate at which space is currently expanding with $h \approx .67$. The curvature of the universe depends on whether the total density is less than (positive curvature; open universe), equal to (no curvature, flat universe), or greater than (negative curvature; closed universe) the critical density, $\rho_c = 1.88h^2 \times 10^{-29} g$cm^{-3} (Hu and Dodelson, 2002).

Different components of the universe are generally described in units of the critical density and defined as Ω_i for the ith component. The standard components used in models consist of: radiation Ω_r, barionic matter Ω_b, cold dark matter Ω_c, the cosmological constant Ω_Λ. From these components, the total matter component is defined as $\Omega_m = \Omega_c + \Omega_b$ and the spatial curvature as: $\Omega_k \equiv 1 - \sum_i \Omega_i$.

Other parameters fit by the standard cosmological model include: the scale of the Baryon Acoustic Oscillations θ_{MC}, the optical depth to reionziation τ, the amplitude of matter fluctuations over 8 h^{-1} Mpc scales σ_8, the amplitude of the primordial power spectrum A_s, and the power law of initial density perturbations n_s.

While some parameters can only be fit degenerately with strictly CMB data ($\Omega_i h^2$, A_s and τ, etc), it is possible to break these degeneracies with help from surveys of galaxies, and supernovae. The best fit cosmological parameters from PLANCK can be found in Table 1.

1.1.3 Current CMB results

The era of precision cosmology with the CMB is possible with the increasingly sensitive maps of the temperature and polarization signals collected by current and future microwave telescopes like PLANCK (Planck Collaboration *et al.*, 2016a), the

Parameter	Planck Fit
$\Omega_b h^2$	$.02225 \pm 0.00016$
$\Omega_c h^2$	0.1198 ± 0.0015
$100\theta_{MC}$ ..	1.04077 ± 0.00032
τ	0.079 ± 0.017
$ln(10^{10}A_s)$	3.094 ± 0.034
n_s	0.9645 ± 0.0049
h	$.6727 \pm .0066$
Ω_m	$0.3156 \pm .0091$
σ_8	0.832 ± 0.0013
$10^9 A_s e^{-2\tau}$	1.882 ± 0.012

Table 1: Best fit cosmological parameters from PLANCK. The fit parameters are taken from the whole likelihood (TT+TE+EE+lowP) fitting from Planck Collaboration *et al.* (2016e).

Wilkinson Microwave Anisotropy Probe (WMAP; Bennett *et al.* 2013), The South Pole Telescope (SPT; Benson *et al.* 2014), BICEP/KECK (Ahmed *et al.*, 2014), The Atacama Cosmology Telescope (ACT; Calabrese *et al.* 2014), and SPIDER (Fraisse *et al.*, 2013). Analysis of these signals provides increasingly confident constraints on cosmological models, and insights on the origins and evolution of the universe.

Continuing advances to hardware and analysis techniques has enabled CMB experiments to push to towards the detection of lower powered signals. Recent cross correlation between CMB maps and galaxy lensing surveys have detected B-mode polarization in the CMB from gravitational lensing (van Engelen *et al.*, 2015, Hanson *et al.*, 2013).

Increased sensitivity also requires a better understanding of foregrounds when performing autocorrelations with a single telescope. The analysis and detection of B-Mode signal in BICEP2 and Keck Array Collaborations *et al.* (2015) from BICEP2, while appearing genuine with their analysis and tests, was later found to be the result

of polarized dust emission during a joint analysis of BICEP2 and PLANCK data (BICEP2/Keck and Planck Collaborations *et al.*, 2015).

The CMB continues to be a powerful tool to investigate and understand the Universe. The formation and evolution of cosmic magnetic fields, however, is not as easily probed by studying CMB anisotropies. The predicted small magnitude (Planck Collaboration *et al.*, 2016d) and angular power (Kosowsky *et al.*, 2005) of primordial magnetic fields require extremely precise measurements of CMB polarization or the correlation of the CMB with other probes of magnetic fields.

1.1.4   Cosmic Magnetic Fields and Faraday Rotation

Polarized photons propagating through non-relativistic plasmas with magnetic field components oriented along the direction of propagation will undergo a rotation of the linear polarization angle

$$\theta(\hat{\mathbf{n}}) = \lambda^2 \alpha_{RM}(\hat{\mathbf{n}}) = \frac{3}{16\pi^2 e} \lambda^2 \int \dot{\tau} \mathbf{B} \cdot d\mathbf{l} \tag{1.6}$$

where α_{RM} is the Faraday Rotation measure, a measure of the amount of rotation undergone by a photon of wavelength λ, $\hat{\mathbf{n}}$ is the direction along the line of sight, e is the charge of an electron, $\dot{\tau}$ is the differential optical depth, and $\mathbf{B}$ is the comoving magnetic field integrated along the comoving length $d\mathbf{l}$ along the trajectory of the photon (De *et al.*, 2013).

Faraday Rotation of CMB photons can cause detectable effects where large magnetic fields exist or where small magnetic fields are coherent over extended cosmic distances(De *et al.*, 2013). For very large magnetic fields, or incoherent magnetic fields near cosmic structure, Faraday Rotation can also cause depolarization of CMB photons (Scóccola *et al.*, 2004).

13

The study of Faraday Rotation can be effective in providing insights on primordial and cosmic magnetic fields. Using the CMB, a pervasive polarized source of photons, as a backlight to construct estimators of Faraday Rotation will provide insights on the cosmic magnetic fields oriented along the direction towards the surface of last scattering.

The exact mathematical formalism of the changes to the CMB photons from FR, both in image and Fourier domains, can be found in Kosowsky and Loeb (1996), Kosowsky *et al.* (2005), Gluscevic *et al.* (2009) and is reviewed briefly in Appendix B. To summarize briefly, FR manifests in Fourier space as a convolution of the polarized E- and B-modes with the α_{RM} modes. This convolution also causes some E-modes to transform into B-modes and vice versa.

This transfer of power from E-mode to B-mode induces a non-zero EB and TB correlation since primordial T and E are correlated through baryon acoustic oscillations and Thompson scattering (De *et al.*, 2013).

With the known mixing of E- and B-modes, estimators of the power spectrum of Faraday Rotation can be created by considering the cross correlations of T, E, and B modes using both a single frequency and multi-frequency power spectra (De *et al.*, 2013, Pogosian, 2014).

Recent results place upper limits on primordial Faraday Rotation at levels comparable to know Galactic FR. Disentangling the two contributions is necessary in order to aid further FR studies. This is illustrated in Figure 7. The proper study and characterization of cosmic and primordial magnetic fields and the constraints set by current and future CMB experiments (Planck Collaboration *et al.*, 2016d) are integral in answering these questions.

The origins of cosmological magnetic fields, however, are not well known. Many
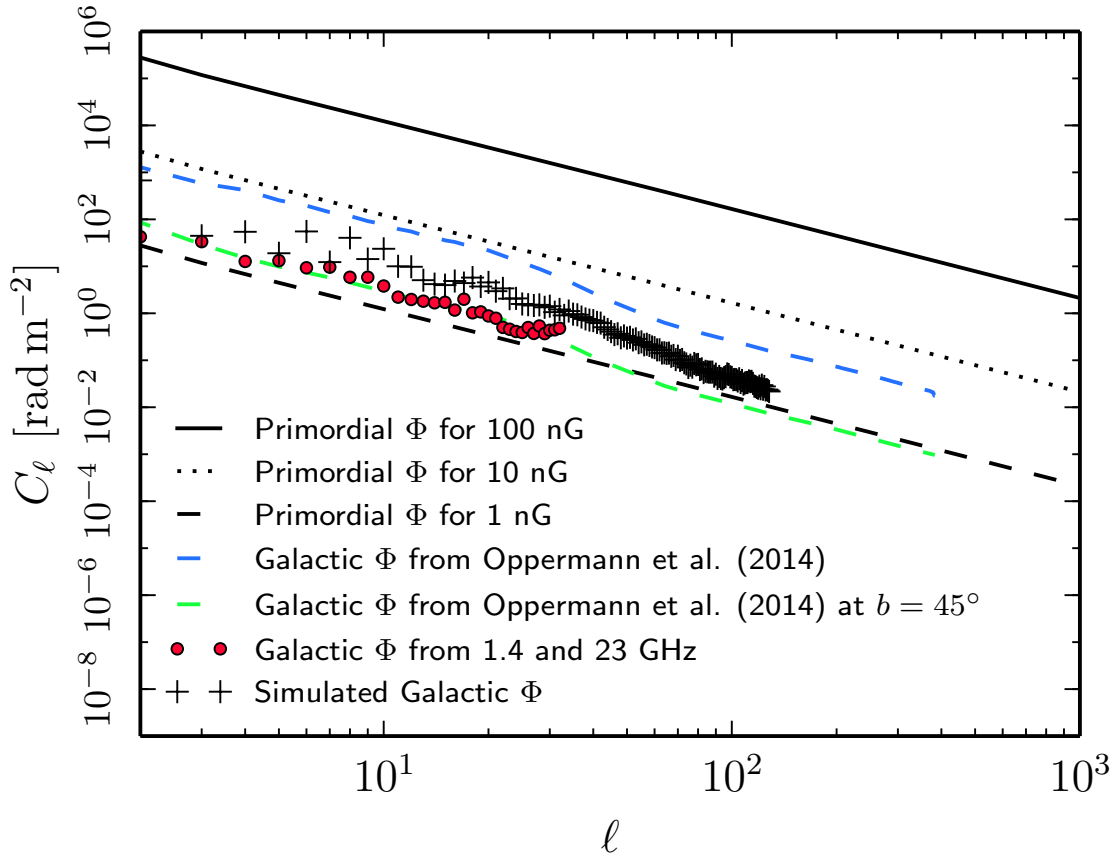
Figure 7: Comparison of expected power of Faraday Rotation from 1,10,100 nG primordial magnetic fields with foreground rotation from galactic and extra galactic contributions. Image from Planck Collaboration *et al.* (2016d)

theories have been speculated as to the origin of primordial magnetic fields (e.g. Vachaspati (1991), Widrow (2002), Ratra (1992), Quashnock *et al.* (1989)). Determining also how these primordial fields affect the evolution of structure and galaxies is also a subject of intensive study (Wasserman, 1978, Ryu *et al.*, 2012, Shibusawa *et al.*, 2014).

With continued research and improving sensitivity, the study of cosmic magnetic fields through FR will provide complementary information to studies concentrating on astrophysical effects coupled to the magnetic field perpendicular to the line of sight.

Using the CMB as a back-light will enable the study of magnetic fields through a various cosmic eras and comparison with FR probes from closer sources (like polarized radio surveys) can inform on the evolution of cosmic magnetic fields.

1.2 The Epoch of Reionization

The CMB provides a wealth of information about the origin and history of the universe. However it can only provide limited insight on the Cosmic Dark Ages and the evolution of cosmic structure during the Epoch of Reionization (EoR). An additional tool is required to study the evolution of the cosmic hydrogen leading up to the global ionization of the intergalactic medium. The emission of 21cm photons from hydrogen due to the spin-flip of the electron relative to the proton can be a powerful tool to probe the eras when few other photons were emitted (Furlanetto *et al.*, 2006). A cartoon representation of this process is illustrated in Figure 8. While this spin-flip transition is forbidden by quantum theory (the expected half life is nearly 11 million years), the vast quantity of hydrogen in the early universe allows for detectable levels of this type of radiation.

I follow the work of Furlanetto *et al.* (2006) to describe the physics of reionization and the challenges faced by radio experiments observing the globally redshifted 21cm line. We refer the reader to the aforementioned work for a detailed analysis of the topics referred to here.

Refer to Appendix C for a definition of important terms to the subject of reionization and the 21cm line.

While there are a multitude of physical processes which contribute to the thermo-
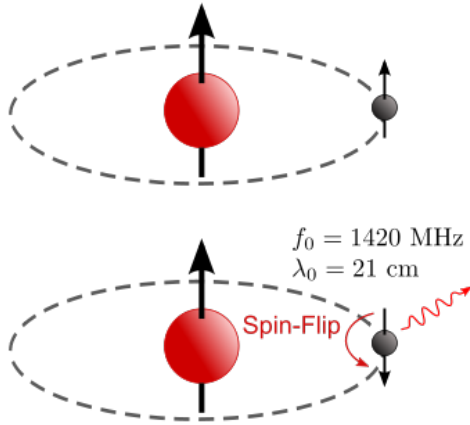
Figure 8: A cartoon representation of the hyperfine transition of Hydrogen between the singlet and triplet spin states resulting in the emission of a 21cm photon. Image adapted from https://commons.wikimedia.org/wiki/File:Hydrogen-SpinFlip.svg

dynamic evolution of the Intergalactic Medium (IGM [2]), we consider only two of the major processes: heating and the reionization mechanisms. These are of particular interest since the type of heating of the IGM contributes to the overall 21cm signal and the driving mechanisms of reionization affect the variance of the 21cm signal.

1.2.1 Probes of HI

There are a number of tools which can be used to gain insight on the ionization history of the universe. The absorption of photons whose energy lies above the Lyα line of hydrogen cause a trough in the spectra of luminous bodies in the early universe (Gunn and Peterson, 1965).

---

[2]Furlanetto *et al.* (2006) notes the IGM is not a completely valid term for the pervasive hydrogen in this era before large scale structure formed. We continue to use it to describe both the pervasive hydrogen before structures form and the true IGM after.
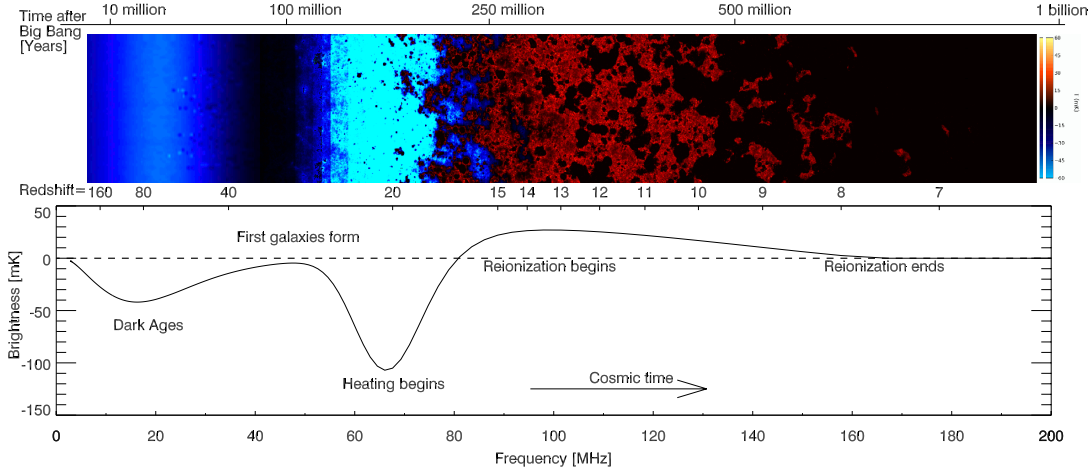
Figure 9: Top: A two dimensional representation of the fluctuations of the 21cm signal created from simulations in (Santos *et al.*, 2008). The color scale represent the strength of the 21cm signal during absorption (blue) and emission (red). Bottom: A visual representation of a the differential brightness between 21cm emission and the CMB during a possible reionization history. The initial separation dip of the brightness temperature corresponds to the time when Compton heating becomes inefficient. The resulting dip allows for absorption of photons by hydrogen. The "Heating" in the figure indicates the time when X-Ray heating becomes dominant. A positive differential brightness allows for the emission of 21cm photons. Images adapted from Pritchard and Loeb (2012).

The presence of the so called Gunn-Peterson trough in high redshift quasars and its absence at redshifts below $z \sim 6$ indicates the presence of a phase shift in cosmic hydrogen from a neutral to ionized state around this time (Becker *et al.*, 2001, Dijkstra, 2016).

The "reionization bump" in CMB polarization power spectrum created during the EoR can also be used to break the degeneracy of fitting A_s and τ (the optical depth to reionization) in CMB analysis. Knowing the optical depth to reionization can also be used to constrain the redshift of reionization (Planck Collaboration *et al.*, 2016e, Reichardt, 2015).

Here I will specifically consider the 21cm photons emitted from neutral hydrogen. This signal is independent of other astrophysical effects like star formation. Unlike the

blackbody radiation of the CMB, the statistics of 21cm photons evolve with redshift. Instead of a single image or snapshot, 21cm observations can create cubes of images, mapping the entire evolution of neutral hydrogen.

1.2.2 The Spin Temperature

The emission of 21cm photons can be characterized by the evolution of the spin temperature (excitation temperature) of hydrogen. The CMB blackbody acts as background light for 21cm photons. Since the emission is already in radio wavelengths, the Rayleigh-Jean limit of the CMB photons can be used to describe the observed brightness along the line of sight:

$$T_b(\nu) = T_S(1 - e^{-\tau_\nu}) + T_{CMB}e^{-\tau_\nu} \tag{1.7}$$

where T_S is the spin temperature (excitation temperature) of neutral hydrogen, and τ_ν is the optical depth along the line of sight for an observed frequency ν.

The contrast between the 21cm emission and the background CMB will be observable between regions with a clear line of sight to the CMB[3] and those obstructed by a hydrogen cloud.

The differential brightness temperature between the 21cm emission and the CMB at redshift z can be written as (Furlanetto *et al.*, 2006, Pritchard and Loeb, 2012)

---

[3]As noted in Furlanetto *et al.* (2006), these sight lines are not always physical but the hypothetical knowledge of the CMB still allows for this comparison.

$$\delta T_b(\nu) = \frac{T_S - T_{CMB}(z)}{1+z}(1 - e^{-\tau_\nu})$$

$$\approx 9x_{HI}(1+\delta)(1+z)^{1/2} \times \qquad\qquad (1.8)$$

$$\left[1 - \frac{T_{CMB}(z)}{T_S}\right]\left[\frac{H(z)/(1+z)}{dv_\parallel/dr_\parallel}\right] \text{mK}$$

Note that this depends on the fractional matter over-density $(1 + \delta)$ and the gradient of the peculiar velocity along the line of sight $(dv_\parallel/dr_\parallel)$.

This contrast becomes saturated when $T_S \gg T_{CMB}$ a time of 21cm emission and can become potentially large and negative when T_S is small (a time of absorption).

The source of the 21cm signal is apparent as a contrast between the excitation of hydrogen atoms versus the underlying CMB backlight. But what drives the evolution of T_S?

Equating the rates at which hydrogen atoms move between the singlet and triplet states as in Furlanetto et $al.$ (2006) will allow a correlation between the spin temperature and the temperature of the IGM. The main mechanisms changing the state of hydrogen are 21cm emission, collision with other atoms, and free protons and electrons as well as scattering from UV and CMB photons.

This modeling is accomplished in (Field, 1958) to determine the dependence of T_S:

$$T_S^{-1} = \frac{T_{CMB}^{-1} + x_c T_K^{-1} + x_\alpha T_\alpha^{-1}}{1 + x_c + x_\alpha} \qquad\qquad (1.9)$$

where x_α and x_c are the coupling coefficients of UV scattering and collision respectively, T_K is the kinetic temperature of the IGM and T_α is the temperature of the Lyα background. These coupling constants and T_α are calculated in Furlanetto et $al.$ (2006).

Figure 9 provides one possible scenario of the different in brightness tempera-

ture between 21cm emission and the CMB. The differential brightness is driven by absorption when negative and emission when positive.

1.2.3 Heating

In an expanding universe, the evolution of the temperature of the IGM, T_k, can be expressed as the sum of cooling from expansion and heating from outside mechanisms (Furlanetto *et al.*, 2006):

$$\frac{dT_k}{dt} = -2H(z)T_k + \frac{2}{3}\sum_i \frac{\epsilon_i}{k_B n} \tag{1.10}$$

where ϵ_i is the energy injected per second per unit volume from the ith source and k_B is the boltzmann constant. After recombination, photons and baryons decouple and the expansion of the universe allows for the diffusion and cooling of the IGM relative to the CMB.

1.2.3.1 Compton Heating

While the global ionized fraction, $\bar{x}_i$, and the photon energy density, $u_\gamma \propto T_{CMB}^4$, are still large, Compton scattering between CMB photon and residual free electrons acts to heat the neutral hydrogen.

This contribution to heating can be calculated as the drag force the CMB exerts on a thermal distribution of free electrons. Seager *et al.* (1999) and J. E. Peebles (1993) show this to be:

$$\frac{2}{3}\frac{\epsilon_{comp}}{k_B n} = \frac{\bar{x}_i}{1 + f_{HE} + \bar{x}_i}\frac{(T_{CMB} - T_K)}{t_\gamma} \tag{1.11}$$

where $t_\gamma \equiv (3m_e c)/(8\sigma_T u_\gamma)$ is the Compton cooling time and f_{HE} is the fraction of Helium. The Compton scattering will draw the temperature of the IGM towards equilibrium with the CMB during this time. While this effect is dominant, the IGM will cool at a similar rate to the CMB, $T_k \propto (1 + z)$.

The temperature of the IGM will behave like an adiabatically expanding non-relativistic gas, $T_k \propto (1 + z)^2$ when Compton scattering is no longer a major contributing heating mechanism.

The time when Compton heating is import occurs before the representation in Figure 9. The decoupling of T_k and T_{CMB}, and initial cooling is already underway near redshift 160 during what is known as the Dark Ages.

The period of absorption following this decoupling is driven by Lyα scattering off hydrogen and dominating Equation 1.9.

1.2.3.2   X-Ray Heating

The formation of non-linear structure and the ignition of the first luminous bodies allows for the production of X-Rays in the early universe. Since X-Rays have a long mean free path, they are an excellent candidate for IGM heating (Pritchard and Loeb, 2012, Furlanetto *et al.*, 2006).

The contributions of X-rays to heating ($f_{X,h}$), ionization ($f_{X,ion}$) and excitation ($f_{X,coll}$) can be calculated exactly for a given energy level of X-rays (Shull and van Steenberg, 1985, Chen and Kamionkowski, 2004). However, there are challenges in determining the exact amount of X-rays in the early universe. In the local universe, star formation rate (SFR) has a strong correlation with the luminosity of X-Rays. Assuming this correlation can be extrapolated to the early universe (Grimm *et al.*,

2003, Ranalli *et al.*, 2003, Gilfanov *et al.*, 2004, Glover and Brand, 2003) , it is possible
to approximate the luminosity of X-Rays:

$$L_X = 3.4 \times 10^{40} f_X \left(\frac{SFR}{1\text{M}_\odot \text{ yr}^{-1}} \right) \text{erg s}^{-1} \tag{1.12}$$

where f_X is a renormalization factor which is unknown but may be approximated.
Other factors upon which the energy released into the IGM from X-Rays may depend
are the efficiency at which stars are formed ($f_\star$) and SFR is proportional the the rate
at which gas collapses into virialized halos (df_{coll}/dt).

These assumptions allow us to write the contribution to heating from X-rays:

$$\frac{2}{3} \frac{\epsilon_X}{k_B H(z) n} = 10^3 K \ f_X \left(\frac{f_\star}{0.1} \frac{f_{X,h}}{0.2} \frac{df_{coll}/dz}{0.01} \frac{1+z}{10} \right) \tag{1.13}$$

According to these assumptions, X-Rays will be contributing a large amount of energy
to the heating of the IGM.

This period around $z \sim 20$ in Figure 9 denoted "Heating Begins" is when x-ray
heating drives the spin temperature from a period of absorption to emission. This
emission is eventually quenched as reionization continues and the IGM becomes fully
ionized.

It is also possible to write the heating contributions from Lyα and shock. While
these mechanisms are important to astrophysics and structure formation, their pure
heating is considered negligible compared to X-Rays and is not discussed in detail
here (Furlanetto *et al.*, 2006).

1.2.4   Ionization and the IGM

The evolution of the ionization fraction, x_i, and spatial fluctuations in x_i along
with matter density fluctuations define the variations in the 21cm emission described

above. These variation makes the detection of the power spectrum of 21cm photons possible. The power spectrum is addressed later in Appendix E.

UV photons emitted from their host galaxies are considered the main mechanism driving the reionization of neutral hydrogen. The rate at which $\bar{x}_i$ changes, must be proportional to interactions with these photons and also the possible recombination of ionized atoms:

$$\frac{d\bar{x}_i}{dt} = \zeta_{UV}(z)\frac{df_{coll}}{dt} - \alpha C(z, \bar{x}_i)\bar{x}_i(z)n_e(z) \tag{1.14}$$

Where $\zeta_{UV}(z)$ is the ionizing efficiency of UV photons at redshift z. This term, along with the recombination coefficient, α, the clumping factor, $C(z, \bar{x}_i) = \langle n_e^2 \rangle / \langle n_e \rangle^2$, and the average electron column density, n_e are all discussed in Furlanetto *et al.* (2006) and Pritchard and Loeb (2012). This topic is discussed in detail in Barkana and Loeb (2001), Haiman (2004), Ciardi and Ferrara (2005) and Loeb (2006). It is also possible to include the contribution of ionization from X-Ray photons with a term proportional to $\zeta_{xray}(z)\frac{df_{coll}}{dt}$ and exploring the ionizing efficiency of X-Ray photons and when they become important to this process. This work is explored in Mesinger *et al.* (2013)

1.2.5   Models and Simulations

Unlike the CMB, there is no single robust model of the 21cm power spectrum against which to compare and experiment. For a complete review of the analytic, semi-analytic and numerical work done to model the evolution of $P(\mathbf{k})$ refer to Morales and Wyithe 2010 section 2.2.
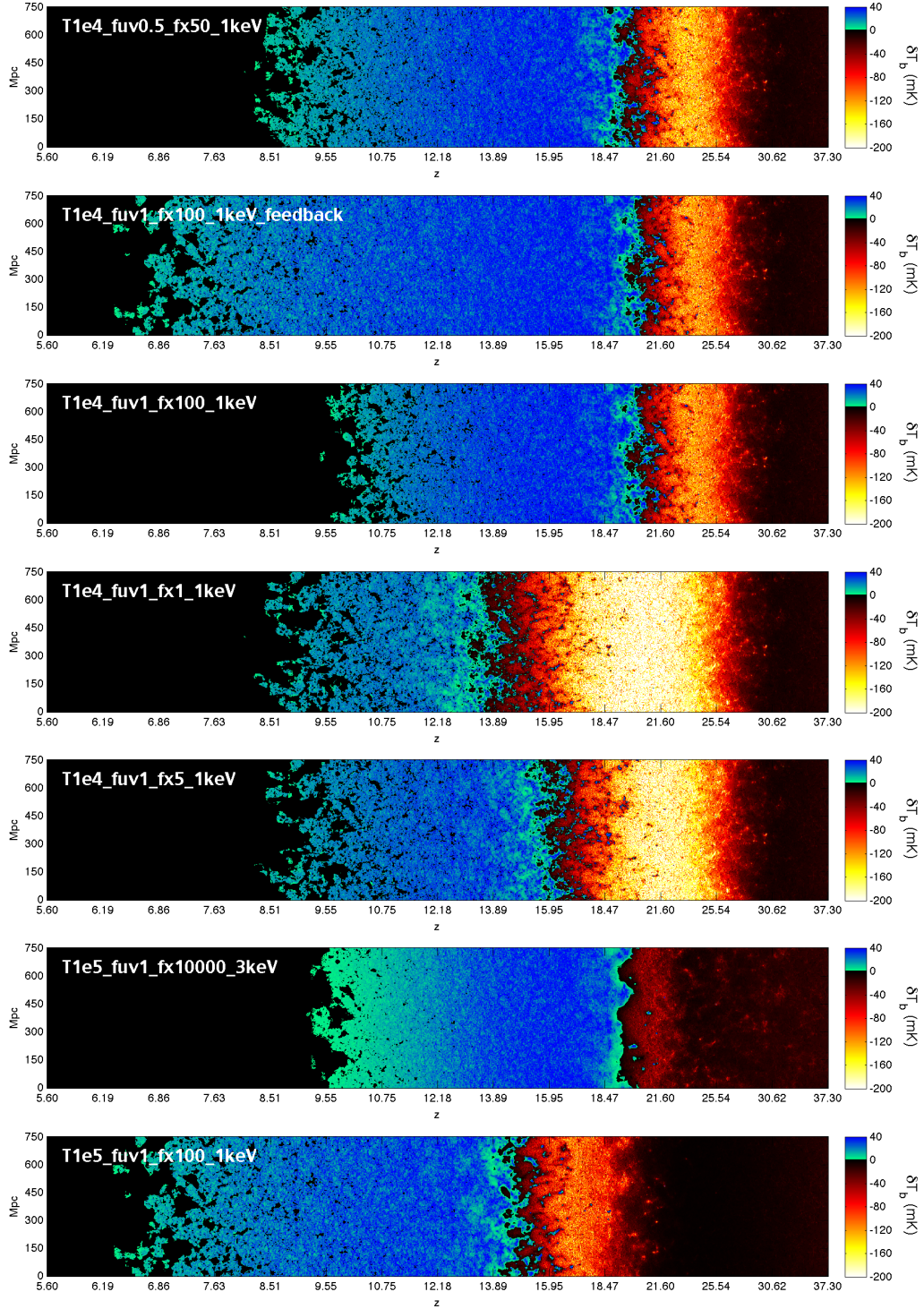
Figure 10: Differential brightness temperature predictions for different scenarios of possible X-ray contributions to ionization. Models parameters include ionizing efficiency of both UV and X-Ray photons, minimum virial temperature and mean photon energy as well as the inclusion of feedback mechanisms. Note both time and color scale are reversed here compared to Figure 9. Image courtesy of Mesinger *et al.* (2013)

25

1.2.5.1 Analytic Models

The bubble model, developed by Furlanetto *et al.* (2004a,b), computes the mass of ionized regions (HII) similar to the excursion set formalism used to compute the dark matter halo mass function. The differences between these models manifests primarily in the barrier used to exclude regions: a constant size is used in the standard formalism and a function of HII region in the bubble model.

In order to compute a power spectrum model from the single point statistics used in the bubble model, Barkana (2007) utilizes two correlated random walks to calculate the power spectrum. This work is expanded in Barkana (2009) to argue that analytic models can be tuned to provide precise predictions of the evolution of the 21cm power spectrum as a function of redshift and used to fit cosmological parameters relevant to the reionization process.

The major lessons learned from analytic models addressed in Morales and Wyithe (2010) include: Large, over-dense regions near sources are ionized first while under-dense regions are ionized by the overlap of growing HII regions, galaxy clustering contributes to increased HII regions beyond expectations of a single ionizing source, and the 21cm fluctuations are inherently non-Gaussian on both large and small scales.

1.2.5.2 Numerical Simulations

The non-linear and non-Gaussian features inherent to reionization ensure precise analytic modeling is both exceedingly difficult and usually dependent on fine tuned initial parameters.

To combat these difficulties, large scale N-body simulations attempt to predict and

model the physics occurring during reionization. Robust simulations must be able to resolve the large scale evolution of HII bubble while also possessing the fine resolution the sources of ionizing radiation (galaxies, quasars). A number of recent simulations (Iliev *et al.*, 2007, Zahn *et al.*, 2007, McQuinn *et al.*, 2007, Shin *et al.*, 2008, Lee *et al.*, 2008, Croft and Altay, 2008) describe the generic features of reionization and established the three points outlined in Morales and Wyithe (2010).

Simulation work by Mesinger *et al.* (2013) also predict the ionizing effects of X-Rays during reionization. While mainly attributed to IGM heating, X-Rays may also contribute to the overall ionization history. The differential brightness temperature as a function of redshift from these ionization scenarios is displayed in Figure 10. Depending on how much X-Rays contribute to ionization and when this occurs, the differential brightness temperature can vary greatly. Some of these simulations also explore the possibility of feedback between the ionizing sources and the heated IGM. The implications and physics of radiative feedback is discussed further in (Mesinger and Dijkstra, 2008, Dijkstra *et al.*, 2004).

1.2.5.3   Semi-Analytic Models

The ability of Mesinger *et al.* (2013) to explore a large phase space of reionization parameters is achieved in part to the semi-numerical ground work laid by Mesinger and Furlanetto 2007, Zahn *et al.* 2007 and Bond and Myers 1996a,b,c.

These semi-analytic models use an excursion-set approach to identify halos in the linear density field and apply a first order perturbation to adjust their locations. Then a filtering technique based on the bubble model is used to estimate ionization based on a source catalog within each halo. Thomas *et al.* (2009) use a large N-body

simulation to construct the ionization field and then apply a library of pre-computed 1D radiative transfer functions to construct HII regions instead of matching a source catalog and filtering.

Both methods of semi-analytic modeling show good agreement as discussed in Morales and Wyithe (2010). The use of these techniques also retain information on the spatial distribution of ionizing sources and structure which is not available with strictly analytic models.

All three types of modeling allow for predictions of the evolution of $P(\mathbf{k})$ as well as predict possible detection scenarios for current and future radio telescopes. Lidz *et al.* (2008) addresses the possibility of detecting 21cm emission with the Murchison Widefield Array (MWA[4]; Bowman *et al.* (2013)). Mesinger *et al.* (2011) introduced the publicly available 21cmFAST[5] code. A fast and customizable code which uses the semi-analytic calculation of reionization to produce models of the 21cm power spectrum.

1.3 Radio Observations

Detecting the 21cm signal, and through it reionization, is possible through a number of methods. Perhaps the simplest idea would be to observe the evolution of x_i directly. A precise measurement of δT_b would be able to map the localized ionization evolution of hydrogen, the 21cm analogue of a CMB anisotropy map.

Measurements of this precision are not available to current radio telescopes however. The radio sky is dominated by synchrotron emission at the radio frequencies used

---

[4]mwatelescope.org

[5]https://github.com/andreimesinger/21cmFAST

to observe δT_b. This emission is orders of magnitude brighter than the predicted underlying 21cm signal. The foregrounds and challenges posed by these experiments are discussed in detail in Morales and Wyithe (2010) and Pritchard and Loeb (2012).

Despite the challenges of observing δT_b directly, there are experiments looking to observe this signal averaged over then whole (observable) sky, $\bar{x}_i(z)$. These so called "global" experiments, like the Experiment to Detect the Global EoR Signature (EDGES[6]; Bowman and Rogers 2010), the Large Aperture Experiment to Detect the Dark Ages (LEDA; Greenhill and Bernardi (2012)), the Shaped Antenna measurement of the background RAdio Spectrum (SARAS; Patra *et al.* (2015)), the Broadband Instrument for Global HydrOgen ReioNisation Signal (BIGHORNS; Sokolowski *et al.* (2015)), and the Sonda Cosmológica de las Islas para la Detección de Hidrógeno NeutroSciHi (SCI-HI; Voytek *et al.* (2014a)) are named for their search for the globally averaged 21cm signal. They are already putting constraints on the duration of reionization (Bowman and Rogers, 2010, Presley *et al.*, 2015, Monsalve *et al.*, 2017). EDGES has recently detected a strong evidence for an absorption trough centered at 78 MHz ($z \sim 17.2$) the first detection of this type from the global experiments (Bowman *et al.*, 2018).

The experiments searching to detect the the differential brightness (δT_b) from the EoR, both in the imaging and power spectrum analysis, include: Giant Metre-wave Telescope (GMRT; Paciga *et al.* (2013)), Precision Array for Probing the Epoch of Reionizaiton (PAPER[7]; Parsons *et al.* (2010)), 21 Centimeter Array (21CMA; Peterson

---

[6]http://www.haystack.mit.edu/ast/arrays/Edges

[7]eor.berkeley.edu

et al. (2004); Wu (2009)), Hydrogen Epoch of Reionziation Array (HERA[8]; DeBoer *et al.* (2016)), MWA, Low Frequency Array (LOFAR[9]; Yatawatta *et al.* (2013)), and Square Kilometre Array (SKA[10]; Mellema *et al.* (2013)).

1.3.1 Challenges of Radio Observations

Many of these experiments use radio interferometers to makes measurements of the sky. The basic principles of radio interferometry are reviewed in Appendix D.

Construction of power spectrum estimators has also come with some challenges for experiments like these. Through the effects of "instrumental mode mixing,"(Parsons *et al.*, 2012) the relatively smooth spectral structure of foreground emissions, which should be restricted to low Fourier Modes in the power spectrum, can contaminate higher Fourier modes beyond the theoretical expectation. The result of this mode mixing creates what is aptly termed the "wedge" in power spectrum estimated by these instruments. This wedge has been observed in numerous simulations and power spectra estimated from data (Datta *et al.*, 2010, Morales *et al.*, 2012, Vedantham *et al.*, 2012, Trott *et al.*, 2012, Hazelton *et al.*, 2013, Pober *et al.*, 2013, Thyagarajan *et al.*, 2013, 2015b,a, Barry *et al.*, 2016).

The wedge is not without limits however, a region of Fourier space still exists theoretically free of foreground signals and ideal for EoR analysis. This "EoR window" consists of a region where spectrally smooth foregrounds do not contaminate the

---

[8]reionization.org

[9]www.lofar.org

[10]skatelescope.org

otherwise isotropic cosmological 21cm signal (Morales *et al.*, 2006, Bowman *et al.*, 2009). This is made possible by the cosmological signal existing isotropically in spherical shells throughout all of Fourier space. A number of analysis pipelines attempt to exploit this fact and focus their analysis in the "EoR window" as a way to avoid foregrounds (Dillon *et al.*, 2013, Parsons *et al.*, 2014, Trott, 2014, Ali *et al.*, 2015, Dillon *et al.*, 2015, Jacobs *et al.*, 2016, Trott *et al.*, 2016).

A number of techniques are also being investigated to remove foreground con-tamination from both point sources and diffuse structure in both image and Fourier domains (Trott *et al.*, 2012, Beardsley *et al.*, 2016, Pober *et al.*, 2016, Line *et al.*, 2017). These techniques all focus on having a precise understanding of either the sky and relevant foregrounds, the baseline response pattern, or some combination of both in order to decrease the contamination of foregrounds to high k-modes.

1.3.2   Current Results

The continued advancements in both the instrumentation and analysis techniques allow current 21cm experiments to place better limits on the 21cm power spectrum from the EoR. A plot of recent limits on the 21cm power spectrum is shown in Figure 11. Though the analysis methods vary from techniques like eigenmode filtering (Dillon *et al.*, 2015), Fringe-Rate Filtering (Parsons *et al.*, 2016, Ali *et al.*, 2015), diffuse foreground subtraction (Beardsley *et al.*, 2016), Optimal Quadratic Estimation (OQE) (Liu and Tegmark, 2011, Trott *et al.*, 2012, Ali *et al.*, 2015, Dillon *et al.*, 2013, Jacobs *et al.*, 2015, Parsons *et al.*, 2014, Dillon *et al.*, 2015, Liu *et al.*, 2014a,b), all these experiments are steadily advancing toward increasingly lower limits on the amplitude of the 21cm power spectrum over a range of redshifts ($6 < z < 12$).
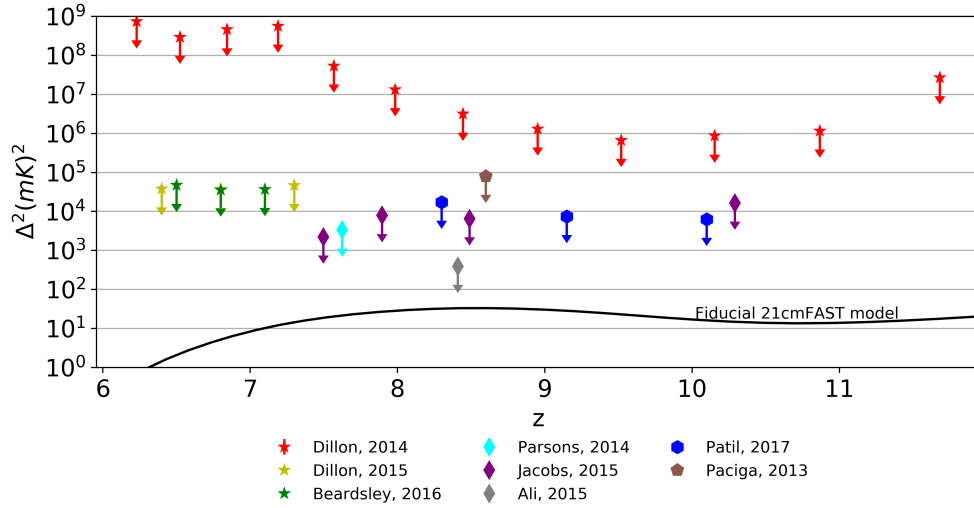
Figure 11: Current best results from many experiments searching for the 21cm power spectrum during reionization averaged in the range $0.1 < k < 0.6$ as of 2017. The theory line on this image is a fiducial 21CMFAST model meant as a reference for expected detection levels.

Recent results from PAPER 64 element deployment are presented in Chapter 3. This analysis and power spectrum estimates are accompanied by an updated version of the plot in Figure 11.

Predictions for the detectability of the 21cm power spectrum are optimistic for the detection with next generation arrays like HERA, and the SKA. HERA has recently begun construction and initial observations in the Karoo desert in South Africa at the previous site for PAPER.

1.4 Probing long wavelength cosmology

The analysis tools, and current results from both the research of the CMB and 21cm emission from neutral hydrogen will form the backbone of the analyses that follows. Chapter 2 outlines a new method of cross correlation to probe for Faraday

Rotation using the CMB as a back-light. This work then presents recent power spectrum estimates from the PAPER 64 element array in Chapter 3 and considers the effects of foreground suppression in power spectrum estimation versus foreground removal in the analysis pipeline. Chapter 4 addresses how foregrounds leak to high Fourier modes in interferometric measurements and introduces a method to evaluate how prone an array is to foreground leakage. The goal of reducing foreground leakage is to produce high fidelity imaging of the EoR and enable power spectrum and cross correlation analysis.

PREFACE TO CHAPTER 2

The following chapter is the published work:

Kolopanis, M., P. Masukopf and J. Bowmann "Detectability of Galactic Faraday Rotation in multiwavelength CMB observations", MNRAS **473**, 4795-4804 (2018).

The text and content of the figures in this chapter match the published MNRAS version of this paper. The formatting of some figures has been altered slightly to fit the page layout of this document.

Chapter 2

DETECTABILITY OF GALACTIC FARADAY ROTATION IN

MULTI-WAVELENGTH CMB OBSERVATIONS: A CROSS-CORRELATION

ANALYSIS OF CMB AND RADIO MAPS

Matthew Kolopanis,[1,2] Philip Mauskopf,[1,2] Judd Bowman[2]
[1]*Department of Physics, Arizona State University, Tempe, AZ 85287*
[2]*School of Earth and Space Exploration, Arizona State University, Tempe, AZ 85287*

Abstract

We introduce a new cross-correlation method to detect and verify the astrophysical origin of Faraday Rotation (FR) in multiwavelength surveys. FR is well studied in radio astronomy from radio point sources but the λ^2 suppression of FR makes detecting and accounting for this effect difficult at millimeter and sub-millimeter wavelengths. Therefore statistical methods are used to attempt to detect FR in the cosmic microwave background (CMB). Most estimators of the FR power spectrum rely on single frequency data. In contrast, we investigate the correlation of polarized CMB maps with FR measure maps from radio point sources. We show a factor of ~ 30 increase in sensitivity over single frequency estimators and predict detections exceeding 10σ significance for a CMB-S4 like experiment. Improvements in observations of FR from current and future radio polarization surveys will greatly increase the usefulness of this method.

2.1 Introduction

Current and future polarized cosmic microwave background (CMB) experiments like PLANCK (Planck Collaboration *et al.*, 2016a), QUIET (Bischoff *et al.*, 2013), WMAP (Bennett *et al.*, 2013), CLASS (Essinger-Hileman *et al.*, 2014), SPT (Benson *et al.*, 2014), SPIDER (Fraisse *et al.*, 2013), and The BICEP/KECK array (Ahmed *et al.*, 2014, BICEP2 and Keck Array Collaborations *et al.*, 2015) image the cosmic microwave background with increasing sensitivity. In particular, these experiments are improving the sensitivity to the polarized E-mode signal and providing better wavelength coverage (30–220 GHz) compared to previous generations of CMB experiments. The first B-mode signals have also been detected via the lensing B-modes in a cross-correlation from SPT (Hanson *et al.*, 2013) and ACT (van Engelen *et al.*, 2015), autocorrelation from SPTpol (Keisler *et al.*, 2015), ACTpol (Naess *et al.*, 2014) and Polarbear (The Polarbear Collaboration *et al.*, 2014), and dust generated B-modes in auto and cross-correlation (BICEP2 and Keck Array Collaborations *et al.*, 2015, BICEP2/Keck and Planck Collaborations *et al.*, 2015).

Another foreground contribution to the B-mode signal in the CMB is Faraday Rotation (hereby referred to as FR) (Scóccola *et al.*, 2004, Tashiro *et al.*, 2008). Primordial, Galactic and extragalactic contributions to FR will cause E-mode and B-mode mixing (Gluscevic *et al.*, 2009). Future B-mode experiments will need to remove this signal in order to accurately characterize polarized signals from primordial sources or an EB cross-correlation.

FR is the displacement of the polarization angle of linearly polarized photons as they propagate through a plasma. While dust or synchrotron polarization provides

information on the component of magnetic fields oriented perpendicular to the line of sight, FR is a probe of magnetic fields along the line of sight.

The presence of 'isotropic birefringence' can also rotate the polarization angle of linearly polarized photons. This effect, however, manifests in a frequency independent manner and imprints a unique, ℓ-independent, signature on the CMB power spectrum. In contrast, the anisotropic nature of FR imprints a signature with known ℓ-dependent structure on CMB power spectra. (Lue *et al.*, 1999, Gruppuso *et al.*, 2016)

Available maps of Galactic and extragalactic FR measure, shown in Figure 12, rely on current radio data (Oppermann *et al.*, 2015) but upcoming radio surveys will provide better overall sensitivity and more precise measurements of FR (Bernardi *et al.*, 2013, Sotomayor-Beltran *et al.*, 2013, Condon, 2015, Sotomayor-Beltran *et al.*, 2015, Wayth *et al.*, 2015, Lenc *et al.*, 2016).

FR becomes significant for photons travelling through regions with large magnetic fields oriented parallel to the direction of photon propagation and regions with weak magnetic fields extending over non-trivial distances (De *et al.*, 2013).

In near-large galaxies, the high electron density, n_e, can cause large FR and may also contain tangled magnetic fields that can lead to depolarization (Carretti, 2010). Depolarization is the net loss of the total polarized intensity. FR can also cause depolarization through differential FR. Differential FR occurs when polarized photons are emitted from a spatially extended source or, in the case of the CMB, from a large primordial magnetic field at the surface of last scattering. Photons undergo different amounts of FR depending upon the extent of the source through which they travel.

For the CMB specific case, a large magnetic field at the surface of last scattering will create a damping effect on E- and B-mode production. In the presence of a large magnetic field, Thomson scattering at the surface of last scattering will cause
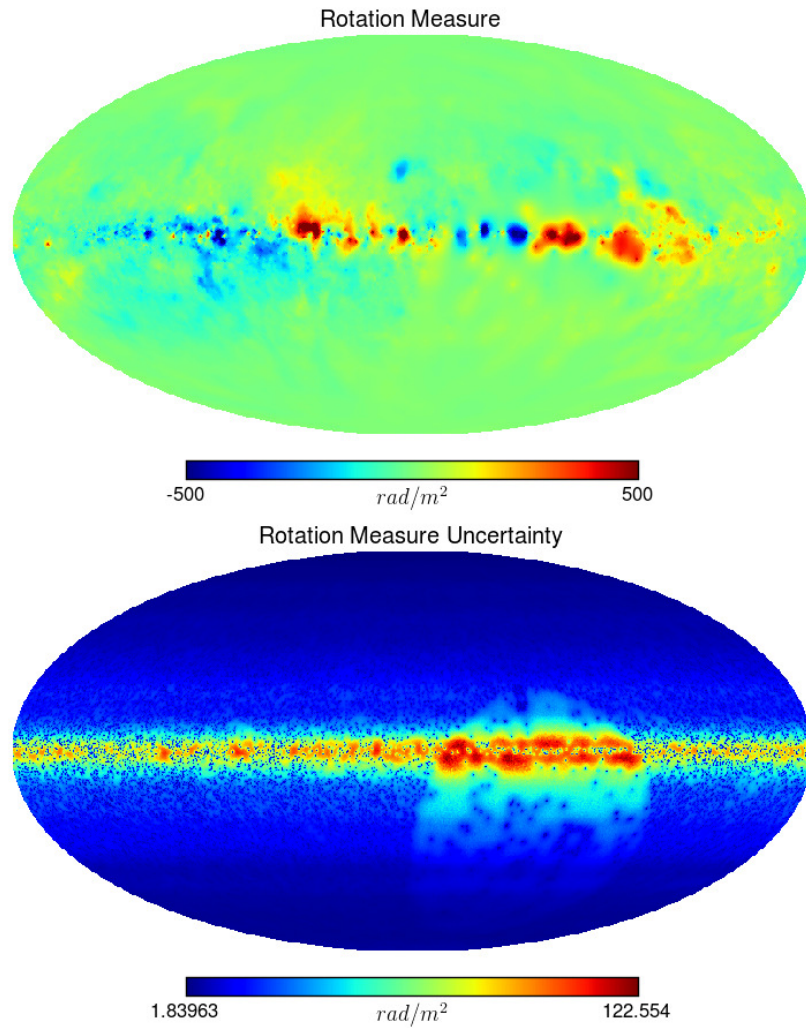
Figure 12: RM of the Galaxy as provided by Oppermann *et al.* (2015). The top figure is the RM reconstruction and the bottom is uncertainty in RM. Note the difference in scales.

depolarization (Scóccola *et al.*, 2004). Specific discussion of these effects can be found in Harari *et al.* (1997) and Scóccola *et al.* (2004) respectively.

The detection of FR at millimeter wavelengths would enable the detection of the rotation of polarized CMB emission due to interactions at high redshifts (e.g. reionization or recombination epochs). This would potentially constrain the amplitude of large-scale magnetic fields.

Characterizing FR through different cosmological eras will also provide insight to the evolution of magnetic fields in the Universe. Observable FR first occurred during photon decoupling at the surface of last scattering (Kosowsky and Loeb, 1996). When the universe is still at a high ionized fraction, photons that have decoupled from the baryionic fluid will experience FR while recombination occurs. Reionization will also leave a signature of FR as ionization fractions increase and photons pass through ionized regions (Scóccola *et al.*, 2004).

Predictions for FR in the CMB at recombination from primordial magnetic fields estimated a 1° rotation in polarization angle at an observed frequency of 30 GHz (Kosowsky and Loeb, 1996). The resulting power spectrum of these polarized photons is estimated to have a peak polarization amplitude of $\ell^2 C_\ell^C \approx 10^{-12}(\mu K)^2$ (Kosowsky *et al.*, 2005). Recent estimates of the strength of primordial magnetic fields from the PLANCK collaboration correspond to a level of FR in the CMB comparable to the amount expected from Galactic sources (Planck Collaboration *et al.*, 2016d). A precise understanding of Galactic FR is required to disentangle the two signals. Detecting Galactic FR in CMB data sets is the first step in this process.

The paper is organized as follows: Section 2.2 reviews FR, Section 2.3 defines the correlator used in this paper and its uncertainty, Section 2.4 analyses the simulations of this correlator, Section 2.5 explores the correlation of FR with other CMB foregrounds,

Section 2.6 applies this analysis to real data, and we provide a discussion of this work in Section 2.7.

2.2 Faraday Rotation

FR occurs as polarized photons propagate through regions of space containing ionized particles and magnetic fields. These photons undergo a rotation in the direction of polarization by an angle

$$\theta(\hat{\mathbf{n}}) = \lambda^2 \alpha_{RM}(\hat{\mathbf{n}}) = \frac{3}{16\pi^2 e} \lambda^2 \int \dot{\tau} \mathbf{B} \cdot d\mathbf{l} \tag{2.1}$$

In this equation $\hat{\mathbf{n}}$ is the direction along the line of sight, $\dot{\tau} \equiv n_e \sigma_T a$ is the differential optical depth, λ is the observed wavelength of the photon, $\mathbf{B}$ is the comoving magnetic field and $d\mathbf{l}$ is the comoving element of length along the trajectory of the photon (De *et al.*, 2013). The differential optical depth is a function of the free electron density along the line of sight, n_e, the Thomson scattering cross-section, σ_T , and the scalefactor, a. The rotation measure, $\alpha_{RM}(\hat{\mathbf{n}})$, is the wavelength-independent quantity describing the strength of FR along the line of sight.

Under FR, the Stokes parameters are transformed as

$$Q_\lambda + iU_\lambda = (Q_0 + iU_0)e^{2i\theta(\lambda, \hat{\mathbf{n}})} \tag{2.2}$$

where Q_0 and U_0 are the un-rotated Q and U parameters of the photons in the limit lambda goes to 0, equivalent to the intrinsic polarization of the radiator (e.g. the surface of last scattering).

While the un-rotated polarization bases cannot be directly observed, the effects of FR in multifrequency experiments can be observed through the phase difference

between frequencies

$$Q_i + iU_i = (Q_j + iU_j)e^{2i(\lambda_i^2 - \lambda_j^2)\alpha(\hat{\mathbf{n}})} \qquad (2.3)$$

where subscripts i, j represent different observation frequency bands. In other words, the polarization vector, $Q + iU$, should differ by a phase proportional to the difference of the squares of wavelengths between two frequency bands.

Estimators of the RM power spectrum can be constructed from direct observation of the Gradient (E-mode) and Curl (B-mode) power spectra of the CMB (Gluscevic *et al.*, 2009, Kamionkowski, 2009, Yadav *et al.*, 2009, De *et al.*, 2013, Pogosian, 2014). Such an estimator can also be used to constrain the strength of primoridial magnetic fields (Pogosian, 2014, Ade *et al.*, 2015, Planck Collaboration *et al.*, 2016d). These optimal estimators will help constrain early universe models and the evolution of magnetic fields. Unfortunately, noise levels in current CMB experiments are too high to characterize the FR power spectrum.

In this paper, we calculate the cross-correlation of FR measure maps provided by Oppermann *et al.* (2015) with CMB maps. This correlation can be used to verify the presence of FR in the CMB from a known source (e.g. FR measured from radio observations) and as a tool to verify astrophysical FR in CMB observations. Since FR is cumulative, direct fitting for α_{RM} will only recover the net effect of astrophysical FR, FR intrinsic to sources and any systematic effects that manifest in the uncertainty of polarization angle.

2.3 Faraday Rotation Correlator

2.3.1 Correlator

To construct this correlation, consider maps of observed CMB Stokes parameters Q and U. For each pixel, n, in these maps, the small angle approximation of equation Equation 2.3 becomes

$$Q_i^n + iU_i^n = (Q_j^n + iU_j^n)e^{2i(\lambda_i^2 - \lambda_j^2)\alpha(\hat{\mathbf{n}})}$$

$$\approx (Q_j^n + iU_j^n)(1 + 2i(\lambda_i^2 - \lambda_j^2)\alpha_{RM}^n) \tag{2.4}$$

Since Stokes Q and U are both real quantities, we can separate the real and imaginary parts of this equation and calculate the difference in each as

$$\Delta Q_{ij}^n = Q_i^n - Q_j^n = 2(\lambda_i^2 - \lambda_j^2)\alpha_{RM}^n U_i^n$$

$$\Delta U_{ij}^n = U_i^n - U_j^n = -2(\lambda_i^2 - \lambda_j^2)\alpha_{RM}^n Q_i^n \tag{2.5}$$

where the subscripts i, j represent frequency bands. The minus sign convention here is chosen such that the resulting power spectra are positive. Applying this correlator requires maps of Q and U from at least two frequencies and a sufficient map of α_{RM}. To combine more than two pairs of maps we employ an inverse variance weighting of the correlation for multiple frequency pairs.

Using the standard spherical harmonic decomposition, we define

$$\frac{\Delta Q_{ij}}{2(\lambda_i^2 - \lambda_j^2)} \equiv \sum_{\ell m} q_{\ell m}^{ij} Y_{\ell m} \tag{2.6}$$

$$\frac{\Delta U_{ij}}{2(\lambda_i^2 - \lambda_j^2)} \equiv \sum_{\ell m} u_{\ell m}^{ij} Y_{\ell m} \tag{2.7}$$

$$-\alpha_{RM}(\hat{\mathbf{n}})Q_i \equiv \sum_{\ell m} r_{\ell m}^i Y_{\ell m} \tag{2.8}$$

$$\alpha_{RM}(\hat{\mathbf{n}})U_i \equiv \sum_{\ell m} s^i_{\ell m} Y_{\ell m} \tag{2.9}$$

The factor $2\left(\lambda_i^2 - \lambda_j^2\right)$ in Equations 2.6 and 2.7 is introduced to construct a wavelength-independent correlator. These four maps will form the basis of our cross-correlations. Equation 2.5 shows that under small rotations the quantities in equations 2.6 and 2.9 should be equivalent since the $2\left(\lambda_i^2 - \lambda_j^2\right)$ will cancel in the definition of ΔQ_{ij} in equation 2.5. This will also hold for equations 2.7 and 2.8.

From the spherical harmonic coefficients, cross-correlations can be defined as

$$C_\ell^{AB} = \frac{1}{2\ell + 1} \sum_{m=-\ell}^{\ell} Re\left\{A^*_{\ell m} B_{\ell m}\right\} \tag{2.10}$$

Where A and B denote the two maps used in a cross-correlation, for this work equaitons 2.6 and 2.9, and equations 2.7 and 2.8. These two angular power spectra can then be added together to create the detection correlator

$$\begin{aligned} C_\ell^{FR} &= \frac{1}{2\ell + 1} \sum_{m=-\ell}^{\ell} Re\left\{ q^*_{\ell m} s_{\ell m} + u^*_{\ell m} r_{\ell m} \right\} \\ &= C_\ell^{\Delta Q \times \alpha U} + C_\ell^{\Delta U \times \alpha Q} \end{aligned} \tag{2.11}$$

2.3.2 Uncertainty

The theoretical uncertainty in equation 2.11 can be calculated following the work of Polenta *et al.* (2005). The method calculates the uncertainty in a cross-correlation as

$$\delta \tilde{C}_\ell^{ij\,2} = \frac{2}{\nu_\ell} \left\{ C_{\ell,th}^{ij\,2} + \frac{C_{\ell,th}^{ij}}{2}\left(N_\ell^i + N_\ell^j\right) + \frac{N_\ell^i N_\ell^j}{2} \right\} \tag{2.12}$$

where $\nu_\ell = (2\ell + 1)\Delta\ell f_{sky}\frac{w_2^2}{w_4}F_\ell$, f_{sky} is the fraction of the sky observed, $\Delta\ell$ is the size of a bin in ℓ space, w_2 and w_4 are powers of integrals of a pixel space masking function and F_ℓ is a power-transfer function. These quantities and an in-depth analysis can

be found in Hivon *et al.* (2002). The subscript *th* denotes a theoretical model. For this work, we represent $C^{i,j}_{\ell,th}$ as multiple realizations over noiseless CMB simulations inserted into the correlator pipeline. The two maps are given superscripts i and j, and their respective noise power spectra denoted as $N^{i,j}_\ell$.

An estimate of the noise power in equation 2.6, $N^{\Delta Q}_\ell$, and equation 2.9, $N^{\alpha U}_\ell$, is required to use equation 2.12. To accomplish these estimates, considering equations 2.6 and 2.9, write

$$q^{ij}_{\ell m} = \int d\Omega \left[\frac{Q^i(\theta, \phi) - Q^j(\theta, \phi)}{2 \left(\lambda^2_i - \lambda^2_j \right)} \right] Y^*_{\ell m}(\theta, \phi) \tag{2.13}$$

$$s^{ij}_{\ell m} = \int d\Omega \left[\alpha(\theta, \phi) \times U^j(\theta, \phi) \right] Y^*_{\ell m}(\theta, \phi) \tag{2.14}$$

Assuming each map to be a sum of signal and noise components: $Q^i = Q^i_0 + \delta Q^i$, $U^i = U^i_0 + \delta U^i$ and $\alpha = \alpha_0 + \delta$, and equations 2.13 and 2.14 become

$$q^{ij}_{\ell m} = \int d\Omega \left[\frac{Q^i_0 + \delta Q^i - Q^j_0 - \delta Q^j}{2 \left(\lambda^2_i - \lambda^2_j \right)} \right] Y^*_{\ell m}(\theta, \phi) \tag{2.15}$$

$$s^{ij}_{\ell m} = \int d\Omega \left[(\alpha_0 + \delta\alpha) \times (U^j_0 + \delta U^j) \right] Y^*_{\ell m}(\theta, \phi) \tag{2.16}$$

Then we separate terms that rely on any noise component from the purely signal components and square in Fourier space. Converting the integrals to summations over pixels of size Ω_{pix}, and writing the uncertainty per pixel in a map X as σ_{X_n}, the noise power spectra can be written as

$$N^{\Delta Q}_\ell = \sum_n^{N_{pix}} \frac{\sigma^2_{Q^i_n} - 2\sigma_{Q^i_n}\sigma_{Q^j_n} + \sigma^2_{Q^j_n}}{\left(2(\lambda^2_i - \lambda^2_j) \right)^2} \frac{\Omega^2_{pix}}{4\pi} \tag{2.17}$$

$$N^{\alpha U}_\ell = \sum_n^{N_{pix}} \left[\sigma_\alpha U^j_0 + \alpha_0 \sigma_{U^j} + \sigma_\alpha \sigma_{U^j} \right]^2 \frac{\Omega^2_{pix}}{4\pi} \tag{2.18}$$

Instrument	ν (GHz)	FWHM (acrmin)	Noise Depth (μK-arcmin)
QUIET	43.1	27.3	36
	94.5	11.7	36
BICEP/ KECK	95	30	3.4
	150	30	3.4
ACT	30	5	14
	40	5	14
	90	2.2	11
	150	1.3	10
	230	0.9	35
PLANCK	30	33	210
	44	24	240
	70	13	300
SPIDER	90	49	15
	150	30	11
	250	17	36
CMB-S4	40	4	1
	90	2	1
	150	1	1
	220	0.7	1

Table 2: Parameters used in CMB simulations. All parameters derived from Bischoff *et al.* (2013), Chang (2013), Fraisse *et al.* (2013), Calabrese *et al.* (2014), BICEP2 and Keck Array Collaborations *et al.* (2015), Planck Collaboration *et al.* (2016a).

Inserting these into equation 2.12, a theoretical estimation of the variance in the cross-correlation power spectrum can be computed. This process can also be repeated to estimate the noise for the correlations of equations 2.7 and 2.8. The two separate variance estimators are then added in quadrature to provide an estimate of the uncertainty for Equation 2.11. We also produce noise estimators by performing Monte Carlo simulations over independent noise simulations. The agreement between these estimators is shown in Figure 13. We find a good agreement between these two estimators in general. Variations between them can result from a spatial structure that exists in the noise maps not captured by an RMS thermal noise power.

2.4 Simulation

We simulate CMB observations for the following surveys: QUIET, PLANCK, BICEP/KECK, AdvancedACT, PLANCK, SPIDER and sensitivities expected for CMB-S4. The parameters used to construct these simulations are described in Table 2. The CAMB software is used in simulating CMB data (Lewis *et al.*, 2000, Howlett *et al.*, 2012) and the HEALPIX[11] (Górski *et al.*, 2005) and ANAFAST packages are used in data processing.

We generate pure CMB simulated data and apply FR to the polarized Q and U maps based on the frequencies of a given array. The RM used to facilitate FR in these simulations is the map provided by Oppermann *et al.* (2015) and shown in Figure 12.

The polarized Q and U maps are then smoothed to the observing resolution for each instrument. White noise is added to the smoothed polarized maps before an additional smoothing with a Gaussian beam to the desired resolution for analysis. Noise is added before the final smoothing since data product maps are created at different spatial resolutions but must be smoothed to the same resolution for before this analysis. In order to properly difference maps of Q and U from different observational wavelengths, we smooth all maps to resolution of 40arcmin. Since the FR maps used in the analysis are only available at Healpix $NSIDE = 128$, we downgrade all maps to this Healpix $NSIDE$ and smooth to avoid pixelization effects.

These images are then analysed using the method from section 2.3. The results from these simulations are characterized using the following definitions.

To find the likelihood of a correlation, we calculate the posterior distribution for a scalefactor β such that

---

[11]Information on HEALPix available at http://healpix.sf.net/
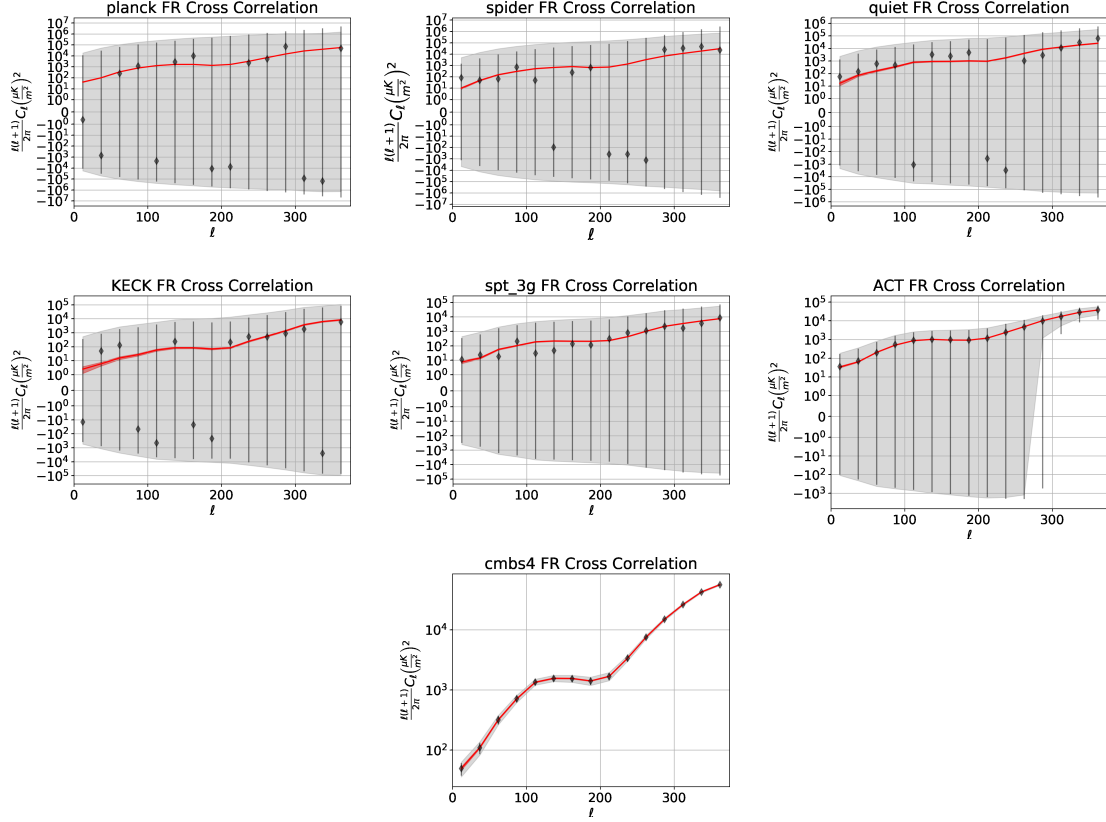
Figure 13: Simulated output power spectra from QUITE, PLANCK, SPIDER, SPT-3G, AdvancedACT, and CMB-S4. The grey region represents the noise estimator given in Equation 2.12, error bars are generated by Monte Carlo trials over $N = 500$ noise simulations. The theoretical and MC error bars show agreement within the simulated regions. The red line and surrounding red shaded region represent the theoretical signal for each experiment and uncertainty due to cosmic variance. Large thermal noise in current generation CMB arrays and limited spatial resolution of the FR map limit the signal to noise of this correlation. Experiments like the future CMB-S4 will have sufficient sensitivity to make high signal-to-noise detections of this signal. Signal-to-noise for each experiment is computed for $25 < \ell < 250$ due to the limited resolution of the radio RM maps. Higher resolution maps would allow for experiments like AdvancedAct to make detections at higher multipole moments.

47
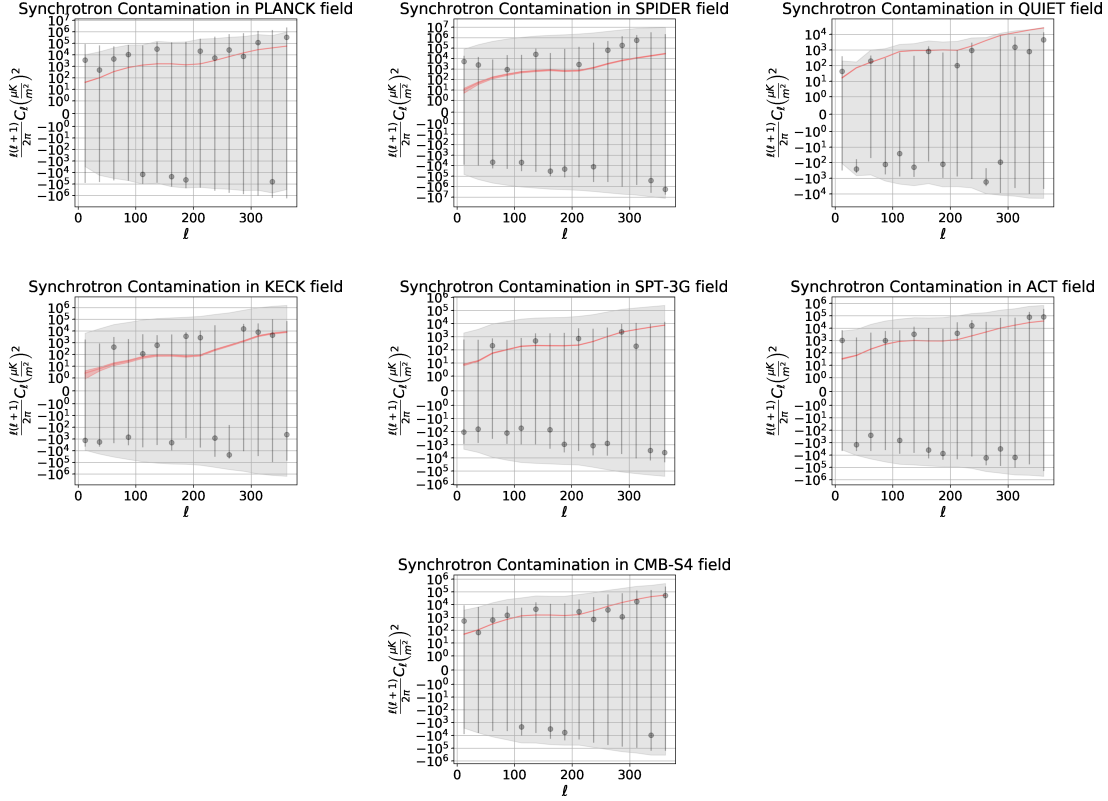
Figure 14: Same as Figure 13, but for inputs maps containing only polarized synchrotron. The grey shaded region is the theoretical error bar with the jack-knife error. Error bars represent the standard deviation in a bin. The red line is the theoretical estimate of the FR cross-correlation signal in the region. Synchrotron emission can contribute power on the same scale or higher as the expected FR signal. This power is dominated by the uncertainty in the correlation however. Good synchrotron removal is necessary to perform this correlation properly. The construction of synchrotron templates allows for high-precision subtraction to be performed on CMB data.
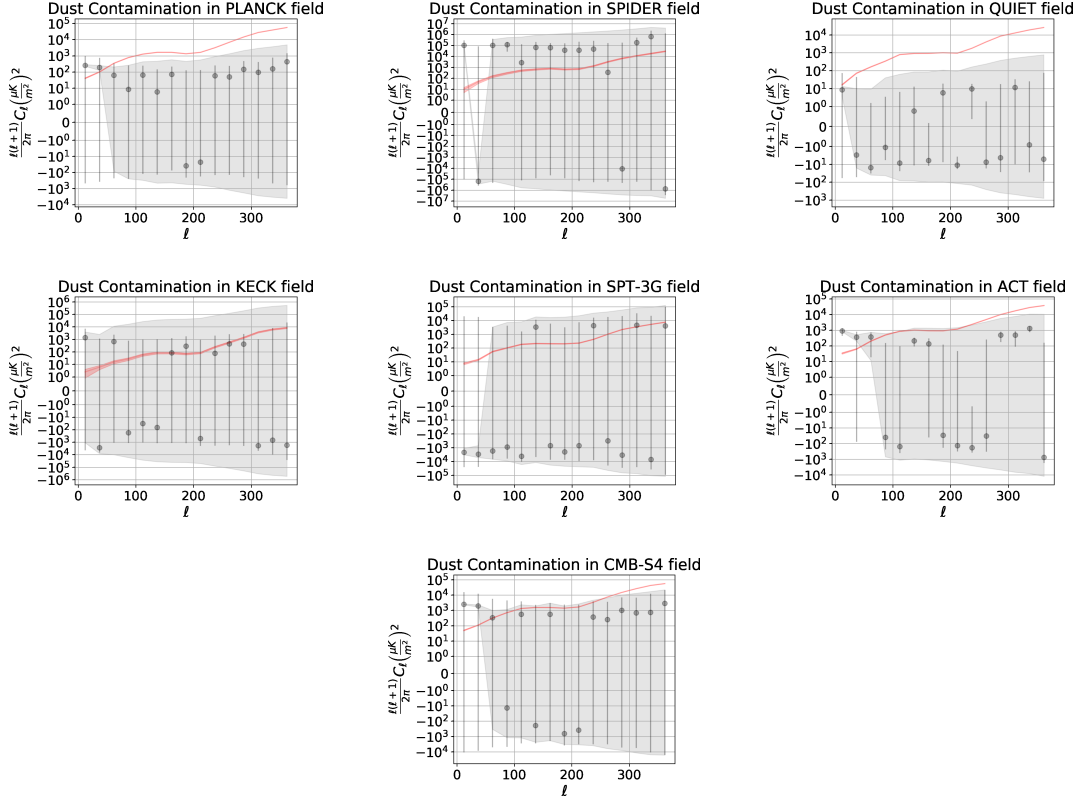
Figure 15: Same as Figure 13, but for inputs maps containing only polarized dust from Planck. The grey shaded region is the theoretical error bar with the jack-knife error. Error bars represent the standard deviation in a bin. The red line is the theoretical estimate of the FR cross-correlation signal in the region. Some experiments observe in regions with low dust and are not subject to this foreground. Experiments with high dust power also exhibit large uncertainty, and this would contribute to the uncertainty in the correlator. Overall, large uncertainty in the correlation requires good removal of polarized dust emission.

$$C_\ell^{FR} = \beta C_{\ell,th}^{FR} \tag{2.19}$$

with the $C_{\ell,th}^{FR}$ given from noiseless simulations in the observed region. Due to the low angular resolution of current FR measure maps, this posterior is only fit for $25 < \ell \leq 250$. Assuming a uniform prior distribution for β in the range [–1000,1000] and Gaussian variances, when computing the posterior distribution of the simulations, the standard error of the mean is used as the uncertainty of the data points. Defining the estimator of β as $\bar{\beta}$, it should fall in the interval

$$\bar{\beta} = 1 \pm \frac{\sigma_{\bar{\beta}}}{\sqrt{N_{sim}}} \tag{2.20}$$

where $\sigma_{\bar{\beta}}^2$ is the variance of the posterior distribution and N_{sim} is the number of simulations. We calculate the total SNR of the correlator as

$$SNR = \frac{1}{\sigma_{\bar{\beta}}} \tag{2.21}$$

Since the simulations are designed such that $\beta = 1$, a strong correlation is represented by a narrow peak centred around $\bar{\beta} = 1$. The posterior is computed in this way to determine whether there exists bias in the simulations or correlator.

The results from our simulations are illustrated in Figure 13. The signal to noise expected from this correlation can be found in Table 3. Based on our estimates, current CMB experiments are unable to detect the FR cross-correlation due to the high thermal noise in CMB observations and the limited spatial resolution of current RM maps. Next generation experiments with thermal noise levels similar to the CMB-S4 estimates and increased spatial resolution of RM maps will be able to make high signal-to-noise detections.

2.5   CMB Foregrounds

The presence of polarized CMB foregrounds like synchrotron and thermal dust emission may cause false correlations with this method if present in polarization observations.

An in-depth analysis and discussion of the characteristics of polarized CMB foregrounds can be found in Planck Collaboration *et al.* (2016c). As noted by Dineen and Coles (2004), the intensity of synchrotron emission is a function of the energy density of electrons, $N(E)dE$, and the strength of magnetic field. When the electron energy density exhibits a power-law distribution

$$N(E)dE \propto E^{-(2\alpha+1)}dE \tag{2.22}$$

the intensity of synchrotron radiation takes the form

$$I(\nu) \propto B_{\perp}^{1+\alpha}\nu^{-\alpha} \tag{2.23}$$

where $B_{\perp}$ is the component of the magnetic field perpendicular to the line of sight and α is the spectral index.

This provides information on the total synchrotron intensity, the polarized components of synchrotron emission are described in Orlando and Strong (2013) as

$$Q \propto \int (B_{\perp x}^2 - B_{\perp y}^2)I(s)d\mathbf{s} \tag{2.24}$$

$$U \propto \int (2B_{\perp x}B_{\perp y})I(s)d\mathbf{s} \tag{2.25}$$

where the $B_{\perp x}$ and $B_{\perp y}$ are the components of the magnetic field perpendicular to the line of sight and the integral is performed along the line of sight.

While synchrotron emission and FR are dominated by components of the same magnetic field, B, some field configurations may produce the existence of one effect and not the other (e.g. FR without synchrotron and vice-versa).

Polarized thermal dust emission is dominated primarily by the temperature of the dust, T_d, as well as the component of the magnetic field perpendicular to the line of sight $\mathbf{B}_\perp$ and its alignment with the orientation of dust particles (Planck Collaboration et $al.$, 2015a). While its correlation with FR cannot necessarily be intuitively predicted, much work has been done attempting to simulate this emission (Planck Collaboration et $al.$, 2015a, Ghosh et $al.$, 2017, Vansyngel et $al.$, 2017) and accurate simulations of emission can be used to estimate the amount of correlation.

Dineen and Coles (2004) use a Spearman rank-order correlation coefficient to investigate the amount of correlation between FR from radio point sources and CMB foreground maps. They find a stronger correlation between dust and FR than between synchrotron and FR, even outside the galactic centre.

For our analysis we are investigating how polarized foreground may cause a false correlation with our method. The residual correlations found in the Spearman rank-order analysis suggest that polarized CMB foregrounds may produce false positive correlation.

To determine the extent to which the FR cross-correlation may be contaminated by other low-frequency polarized CMB foregrounds, we compute the correlator from section 2.3 with polarized dust and synchrotron maps provided by PLANCK (Planck Collaboration et $al.$, 2016b) for each set of observed frequencies in the simulated experiments.

We can estimate the error in the foreground correlation by sending a jack-knifed map, created from differencing the Half mission 1 and Half mission 2 images from

each potential foreground respectively, through the correlation pipeline. This error is represented by the shaded regions in Figs 14 and 15.

Fig. 14 shows the results of cross-correlation pipeline when the polarized synchrotron maps are substituted for rotated CMB images. Within error, this correlation is found to be consistent with zero and is not expected to contaminate a net signal to the correlation. The large magnitude of recovered correlations is comparable to the expected FR signal and indicates that proper foreground removal from observation is necessary to ensure synchrotron contamination does not dominate the final error budget.

Similarly, Fig. 15 shows the results of the cross-correlation pipeline when the polarized dust maps are substituted for rotated CMB images. Polarized dust shows a residual correlation for the simulated frequencies. This signal is especially prominent in the high frequencies where dust emission is strong. Hence, in the analysis of actual observations, care must be taken to accurately remove this foreground before performing the cross-correlation.

For both types of foregrounds analysed, the jack-knife errors dominate any potential residual signal. Without proper removal, these foregrounds may contribute to a false correlation or an anticorrelation. The existence of detailed foreground maps for direct subtraction and the usage of techniques like a principle component analysis allow for the removal of these foregrounds from CMB maps in practice.

2.6 Application to Real Data

Based on the simulation, the low-frequency data collected by PLANCK should not be able to detect the effects of the Galactic FR. The contributions from thermal noise
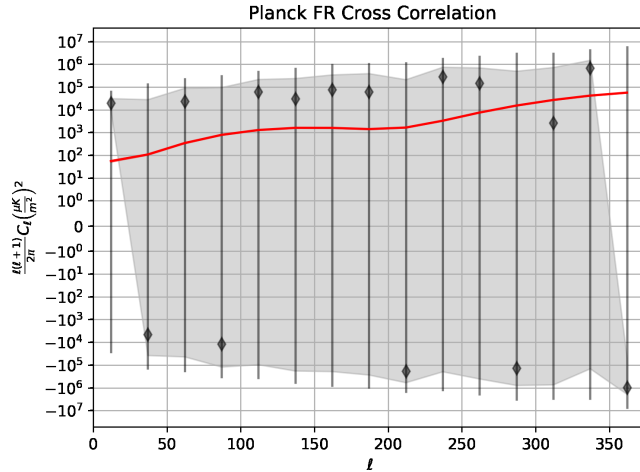
Figure 16: Real Planck LFI data correlation, the inverse variance weighted sum of 30x44, 44x70 and 30x70 correlators. The error bars are derived from the standard deviation within a bin of $\Delta\ell = 25$. The correlator is consistent with zero for all tested multipoles, indicating no observable signal in the data. The grey shaded region represents the theoretical error obtained obtained from the covariance provided in the planck data. Discrepancy between the error bars and shaded regions may be a representative of the limited statistics in the data.

dominate the correlation. In this section, we apply the correlator to actual PLANCK data to test the predictions above.

When applied to Planck LFI data, the cross-correlation produces the results shown in Fig. 16. Black error bars in Fig. 16 are given by the standard deviation of the power spectrum in a bin of $\Delta\ell = 25$ over $N = 500$ realization of the noise covariance map provided in the PLANCK data release injected into a simulated CMB signal. The grey shaded region is the theoretical error given in Section 2.3.2 with the thermal noise level from Planck Collaboration *et al.* (2016a). The posterior distribution of β is generated using the theoretical error bars for the PLANCK data. The posterior distribution for β produces $\bar{\beta} = 27.91$ and $\sigma_{\bar{\beta}} = 74.00$.

The mean of the posterior is consistent with zero within error and the standard deviation of the posterior, $\sigma_{\bar{\beta}}$, and the SNR from the analysis of the PLANCK

Experiment	Frequencies (GHz)	Noise levels (μK-arcmin)	f_{sky}	$\bar{\beta}$	$\sigma_{\bar{\beta}}$	S/N Galactic FR
PLANCK	30,44,70	210,240,300	0.73[1.]	.21	63.80	0.02
BICEP2	100,150	3.4	0.01	0.71	25.09	0.04
SPIDER	90,150	10	0.1	0.59	23.11	0.04
QUIET	45,90	36	0.005	1.41	13.07	0.08
SPT3G	150,220	3.5,6	0.06	0.90	8.42	0.11
AdvancedACT	30,40,90,150,230	14,14,11,10, 35	0.5	1.03	0.73	1.36
CMB-S4	40-220	1	0.73[1.]	1.00	0.04	22.73
SPT3G	....			0.88	4.13	0.24
AdvancedACT	....			1.03	0.35	2.89
CMB-S4	....			1.01	0.02	45.46

Table 3: Simulation results and estimates of the SNR expected using this method to detect Galactic FR in the CMB. f_{sky} refers to total sky fraction observed. Model parameters taken from Bischoff *et al.* (2013), Chang (2013), Fraisse *et al.* (2013), Calabrese *et al.* (2014), BICEP2 and Keck Array Collaborations *et al.* (2015), Planck Collaboration *et al.* (2016a). The lower rows of SPT3G, AdvancedACT and CMB-S4 represent the parameters of the fit if all available multipole moments are used in the correlation. This demonstrates that increasing fidelity at higher mulitpole moments of the input maps will allow for stronger detections.

1. .73 sky fraction based on WMAP nine-year polarization analysis mask

data agrees with the expected level from simulation within a factor of $\sim 15\%$. The disagreement may be a result of a spatial structure that exists in the noise covariance map provided by PLANCK opposed to the RMS noise amplitude used in simulations. The agreement between the simulated and actual Planck analyses supports the predications made for other experiments as well.

2.7   Discussion

The simulations and analysis of this cross-correlation method for detecting FR in the above sections have addressed two types of surveys. The all-sky survey, which

provides large sky coverage, and the single field survey, which is limited in sky coverage but can integrate to lower noise levels.

The simulation results and estimates of the expected SNR for various survey configurations are displayed in Table 3. The analysis of these simulations is conducted for $25 < \ell < 250$. We predict a signal near 2σ significance in AdvancedACT data and a detectable signal at very high significance ($> 10\sigma$) in a future CMB-S4 experiment. If we fit for $25 < \ell < 384$ (the full multipole resolution of the RM map), we find an increase in statistical significance for SPT3G, AdvancedACT and the CMB-S4 experiments. This demonstrates that increasing spatial resolution of maps used in this analysis will allow for stronger detections of this correlation. According to our analysis, some experiments well suited to observing high CMB-multipoles like the KECK array, SPT, and SPIDER are not good candidates for observing FR. These instruments, while integrating to low noise depths, are observing in regions specifically selected for their low foregrounds and as seen in Figure 12, FR is largest on the Galactic plane and falls off quickly as Galactic latitude increases.

Compared to single-frequency FR power spectrum estimators, like De *et al.* (2013), our expected signal-to-noise ratio using Planck-LFI data is greater by a factor of ~ 30. The single-frequency estimators must also consider weak lensing effects of the CMB in order to accurately constrain their α^{RM} estimator. Since lensing contains only spatially dependent contributions (Lewis and Challinor, 2006) and no dependence on frequency, the multi-frequency estimator considered here offers further advantages for reducing uncertainty from lensing. The use of single frequency or multifrequency estimators (De *et al.*, 2013, Pogosian, 2014) is also able to estimate $\alpha_{\ell m}^{RM}$ from their techniques. Although our cross-correlation results in the convolution of the polarized CMB and $\alpha_{\ell m}^{RM}$ power spectra, this work can be extended to provide an estimate of

the FR power spectrum, $\alpha_{\ell m}^{RM}$, and to remove the effects of weak lensing on the FR estimator.

A map space analysis of non-Gaussain fields like FR will provide knowledge not accessible through the power spectrum. We can estimate the minimum polarized sensitivity required by a CMB experiment to observe detectable Galactic FR in a single pixel at 90 and 150 GHz using the maximum RM recovered by Oppermann *et al.* (2015) of 2500 rad m^{-2}.

We find that ~ 1 degree precision for polarization angle measurements is necessary to construct accurate maps of Galactic FR measure from CMB experiments. Even more sensitive observations are required to estimate extragalactic and primordial FR using CMB as a back-light. These sensitivities are currently beyond CMB experiments. Planck Collaboration *et al.* (2015b) discuss the uncertainty in polarization angle which results from what they describe as conventional fitting and Bayesian inferencing. While some recovered angles show uncertainties below this threshold, the distribution of uncertainties extends up to 45 degrees for Bayesian-derived angles and 100 degrees for conventional estimation methods. These results are shown in Fig. B.1 in Planck Collaboration *et al.* (2015b).

To achieve this level of sensitivity in a CMB experiment, we can estimate the uncertainty level an experiment would require on polarized emission by propagating the uncertainty in $\theta = \frac{1}{2}\tan^{-1}(\frac{U}{Q})$ and assuming equality in uncertainties of Q and U

$(\Delta Q = \Delta U)$:

$$\delta\theta^2 = (\frac{d\theta}{dQ}\Delta Q)^2 + (\frac{d\theta}{dU}\Delta U)^2 + 2\frac{\delta\theta}{\delta Q}\frac{\delta\theta}{\delta U}\sigma_{QU}$$
$$= \frac{1}{4}\left(\frac{QU}{Q^2+U^2}\right)^2\left(\left(\frac{\Delta Q}{Q}\right)^2 + \left(\frac{\Delta U}{U}\right)^2\right) - \frac{1}{2}\frac{QU}{(Q^2+U^2)^2}\sigma_{QU}$$
$$= \frac{1}{4}\frac{\Delta Q^2}{Q^2+U^2} - \frac{1}{2}\frac{QU}{(Q^2+U^2)^2}\sigma_{QU}$$
$$\delta\theta^2 = \frac{1}{4}\left(\frac{\Delta Q^2}{P^2} - \frac{2QU\sigma_{QU}}{P^4}\right)$$

(2.26)

where $P = \sqrt{U^2 + Q^2}$ is the polarization amplitude, and σ_{QU} is the covariance between Q and U. This requires sensitivity at the $1 - 2\%$ level in polarization signal on a per pixel level when $\sigma_{QU} \to 0$. In general, the presence of covariance between the observed Q and U Stokes parameters will complicate the ability to achieve sub-degree precision in polarization angle.

Through modelling and simulation, Planck Collaboration *et al.* (2016d) predict that primordial magnetic fields of order 10nG will produce FR at comparable levels to galactic FR. For fields of these strengths, sub-degree polarization angle sensitivity and precise knowledge of galactic FR would be necessary to identify and characterize effects from these primordial fields.

Until these sensitivity levels are reached, a cross-correlation can be used to identify the Galactic FR contributions to polarized power in the CMB. This kind of cross-correlation can also be used to verify the presence of FR from sources common to polarized surveys. Only the contributions to FR from common sources observed by both surveys [e.g. The CMB and Oppermann *et al.* (2015) maps here] will produce a signal with this kind of correlation.

In conclusion, we expect current CMB experiments to be unable to detect FR even through cross-correlation. Strong residual signal from CMB foregrounds like dust and synchrotron radiation will need to be carefully removed from CMB in any analysis.

AdvancedAct observations may be able to produce a statistically significant signal (~ 2 sigma) through a cross-correlation and the significance of the signal will increase with the inclusion of higher multipole moments in the fitting of $\bar{\beta}$. Intermediary experiments that will have thermal noise similar to or lower than AdvancedAct may exhibit increasingly significant signals through this correlation. Strong detections will be possible with the construction of a future CMB-S4-type experiment.

2.8   Acknowldegements

The following work is the result of research and analysis culminating in best estimation of the 21cm power spectrum by the Donald C. Backer Precision Array for Probing the Epoch of Reionization (PAPER) 64 element deployment. The results themselves are written in a brief document which outlines the observation pipeline, analysis methods and power spectrum estimation techniques. These upper limits result from the re-analysis of the observations from the PAPER-64 element configuration and are the most reliable results from the PAPER array to date.

The first iteration of power spectrum estimates from PAPER-64 are published in Ali *et al.* (2015) (also referred to as A15). This analysis uses an Optimal Quadratic Estimator (OQE) and empirically estimated covariance matrix to attempt to mitigate residual foreground contamination. An OQE with a properly modeled covariance matrix, is traditionally a lossless power spectrum estimator (Tegmark, 1997), however Switzer and Liu (2014), Dillon *et al.* (2015), and even A15 note that the use of an empirically estimated covariance matrix can cause over fitting of noise terms and results in the loss of coherent signal.

Using a simulated signal injected into the data, A15 attempts to quantify the amount of signal loss expected from the analysis by comparing the input known power to the output power which uses the empirical covariance from both the data and the injected signal to down-weight foregrounds. At a levels comparable to the power spectrum estimate of just the data, this comparison yields a $\sim 2\%$ loss from the known signal.

This paper began as an extension of the analysis from A15 by applying the OQE methods to the full redshift band of the same observations. However the power spectra

in other redshift bands failed to pass internal consistency checks like the comparison with a theoretical noise estimator. Further simulations told a complex story of signal loss hidden behind underestimated bootstrap and theoretical uncertainties. These effects and the current power spectrum methodology to counteract signal loss is documented in the collaboration paper Cheng et al (currently in prep.) and again summarized in an erratum on Ali et al (currently in prep.) which also formally retracts the previous upper limits. The following chapter will be the third paper in this series and is presented here in the form of its initial submission. It presents what the PAPER collaboration considers to be the definitive power spectrum estimates from PAPER-64. These results supersede all previous PAPER limits.

Chapter 3

PAPER 64: MULTI-REDSHIFT LIMITS ON THE 21CM POWER SPECTRUM

FROM THE EPOCH OF REIONIZATION

Matthew Kolopanis[1*], Daniel C. Jacobs[1], Carina Cheng[2], Aaron R. Parsons[2,3], Saul A. Kohn[4], Adrian Liu[2,5], James E. Aguirre[4], Zaki S. Ali[2], Gianni Bernardi[6,7,8], Richard F. Bradley[9,10,11], Chris L. Carilli[12,13], David R. DeBoer[3], Matthew R. Dexter[3], Joshua S. Dillon[2], Pat Klima[10], David H. E. MacMahon[3], David F. Moore[4], Chuneeta D. Nunhokee[7], Jonathan C. Pober[14], William P. Walbrugh[6], Andre Walker[6]
[1]*School of Earth and Space Exploration, Arizona State U., Tempe AZ*
[2]*Astronomy Dept., U. California, Berkeley, CA*
[3]*Radio Astronomy Lab., U. California, Berkeley CA*
[4]*Dept. of Physics and Astronomy, U. Penn., Philadelphia PA*
[5]*Berkeley Center for Cosmological Physics, Berkeley, CA*
[6]*INAF-Istituto di Radioastronomia, via Gobetti 101, 40129, Bologna, Italy*
[7]*Department of Physics and Electronics, Rhodes University, PO Box 94, Grahamstown, 6140, South Africa*
[8]*SKA SA, 3rd Floor, The Park, Park Road, Pinelands, 7405, South Africa*
[9]*Dept. of Electrical and Computer Engineering, U. Virginia, Charlottesville VA*
[10]*National Radio Astronomy Obs., Charlottesville VA*
[11]*Dept. of Astronomy, U. Virginia, Charlottesville VA*
[12]*National Radio Astronomy Obs., Socorro NM*
[13]*Cavendish Lab., Cambridge UK*
[14]*Dept. of Physics, Brown University, Providence RI*

Abstract

We present limits on the 21cm power spectrum from the Epoch of Reionization (EoR) from the Donald C. Backer Precision Array for Probing the Epoch of Reionization (PAPER) 64 element configuration. In this work, we present an analysis of the full PAPER 64 data set over the entire redshift range probed by the instrument ($z \sim 7.5$ to 11) and combine data from three unique baselines for increased sensitivity. We report power spectrum limits in redshift bins centered

at $z = 10.87$, 9.93, 8.91, 8.13, and 7.48 along with a re-analysis of the $z = 8.37$ bin from Cheng et al. (2018, *in prep.*). We find upper limits on the 21cm power spectrum in the range $0.3 < k < 0.6$ h Mpc^{-1} on $\Delta^2(k)$ from PAPER 64 to be (650 mK)^2, (450 mK)^2, (390 mK)^2, (250 mK)^2, (280 mK)^2, (250 mK)^2 for the $z = 10.87$, 9.93, 8.91, 8.37, 8.13, and 7.48 redshift bands respectively. Compared to the analysis of Ali *et al.* (2015), which used the same data set in the $z = 8.37$ band, these results reflect lest stringent upper limits by a factor of ~ 10 (in mK). We also demonstrate the importance of the foreground removal technique to obtaining results over the full PAPER frequency (redshift) range. These new limits incorporate important corrections to the PAPER data analysis and power spectrum pipelines described in our companion paper (Cheng et al. 2018, *in prep.*) and the results supersede all previous PAPER results (Ali *et al.* (2015) erratum).

3.1 Introduction

The Epoch of Reionization (EoR) represents the a major phase transition for intergalactic hydrogen from a neutral to ionized state. In most models, this phase transition is fueled by the first luminous bodies, which condensed from hydrogen clouds and began heating and ionizing the surrounding Intergalactic Medium (IGM) (Barkana and Loeb, 2001, Oh, 2001). Observational constraints constrain the timing of this event to somewhere to the redshift range ($12 < z < 6$).

---

*matthew.kolopanis@asu.edu

† Hubble Fellow

$^\diamond$ NSF AAPF Fellow

The 21cm photons emitted from the spin-flip transition of hydrogen are predicted to be a strong probe of cosmic evolution during this time (Furlanetto *et al.*, 2006). For an in-depth review of the physics of 21cm cosmology, refer to Barkana and Loeb (2007), Morales and Wyithe (2010), Loeb and Furlanetto (2013) and Pritchard and Loeb (2010).

As observed from Earth, the 21cm line from the EoR is redshifted to wavelengths comparable to FM Radio, and global telecommunications, among many other terrestrial and astrophysical radio band emissions. Some foregrounds can be mitigated by carefully selecting radio quiet zones to observe. Unfortunately, Galactic foregrounds still dominate radio observations by 4 or 5 orders of magnitude compared to the expected EoR signal. The foreground challenges faced by modern radio arrays are discussed in detail in previous literature (e.g. Santos *et al.* (2005), de Oliveira-Costa *et al.* (2008), Ali *et al.* (2008), Bernardi *et al.* (2009, 2010, 2013), Ghosh *et al.* (2011), Pober *et al.* (2013) and Yatawatta *et al.* (2013)).

Detection of 21cm emission by the neutral hydrogen medium is the target of multiple experiments including those aimed at a globally averaged total power measurement (EDGES; Bowman and Rogers (2010), LEDA;Bernardi *et al.* (2016), SARAS; Patra *et al.* (2015), BIGHORNS; Sokolowski *et al.* (2015), and SCI-HI; Voytek *et al.* (2014b)) and the fluctuations caused by heating, cooling, collapse, and ionization (GMRT; Paciga *et al.* (2013), LOFAR[1]; Yatawatta *et al.* (2013), MWA[2]; Tingay *et al.* (2013), and HERA[3]; DeBoer *et al.* (2016)).

---

[1]www.lofar.org

[2]mwatelescope.org

[3]reionization.org

The Donald C. Backer Precision Array for Probing the Epoch of Reionization (PAPER[4]; Parsons *et al.* (2010)) is an experimental interferometer with the goal of placing some of the first limits on fluctuations.

Previous PAPER publications include the PAPER 8 station results (Parsons *et al.*, 2010), the PAPER-32 element power spectrum estimates (Parsons *et al.* (2014), Jacobs *et al.* (2015), Moore *et al.* (2017)), the PAPER-64 element power spectrum estimates (Ali *et al.* (2015); hereafter A15), and our companion paper (Cheng et al. (2018, *in prep.*); hereafter C18).

The PAPER experiment observed in stages, with the number of antennas increasing by factors of two each year. The 64 antenna experiment was analyzed initially in A15 and again in C18.

Through the rigorous re-analysis in C18, we have identified a major cause of signal loss in power spectrum estimation with an Optimal Quadratic Estimator (OQE). Signal loss is the unintentional removal of coherent signal during analysis. This results from the use of empirically estimated covariance matrices as a weighting matrix in a QE. An empirically estimated covariance matrix contains terms related to the data, this dependence induces higher order (i.e. non-quadratic) terms in a QE. Applying the OQE normalization despite these terms then gives the wrong power level (i.e. signal loss). This effect is described more thoroughly in Section 3.1.1 of C18. This analysis also found the previous bootstrapping method to underestimate the variance in our power spectrum estimator. These effects compounded in our analysis in A15 to form a severely underestimated upper limit on the 21cm power spectrum. C18 used an updated thermal uncertainty model to help inform the analysis and identify these shortcomings.

---

[4]eor.berkeley.edu
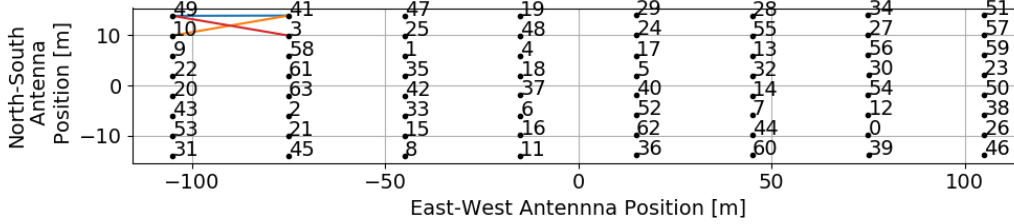
Figure 17: The antenna positions of the PAPER 64 element array. Highlighted are the three baseline types used in this analysis. These baselines consist of East-West baselines from adjacent antenna columns with no row separation (blue line [O type]; e.g. 49-41, 1-4, 0-26), baselines with one column separation and one positive Northward row separation (orange line [E+ type]; e.g. 10-41, 1-48, 0-38), and baselines with one column separation and one negative Northward row separation (red line [E- type]; e.g. 49-3, 1-18, 0-46). Note the aspect ratio of this plot has been exaggerated in order to easily highlight the different baseline types.

In this paper, the updated analysis techniques described in C18 have been applied to the full redshift range probed by the PAPER instrument ($z \sim 7.5$ to 11). We use this extended redshift range to examine the performance of the OQE and revised signal loss correction under various foreground conditions. We find similar subtraction residuals can be achieved using multiple foreground filtering techniques. Using a combination of foreground filtering techniques, we provide revised upper limits on the 21cm power spectrum from PAPER. The upper limits reported in this paper represent the most confident results achieved by the PAPER instrument to date and supersede all previous results (A15 erratum).

This work is organized as follows: we briefly review the data used in this analysis in section 3.2 (it is the same as both A15 and C18). In section 3.3 we review the revised power spectrum estimation techniques and uncertainties. The multi-redshift power spectrum results are presented in section 3.4 and discussed in section 3.5. Finally, we provide some concluding remarks in section 3.6.
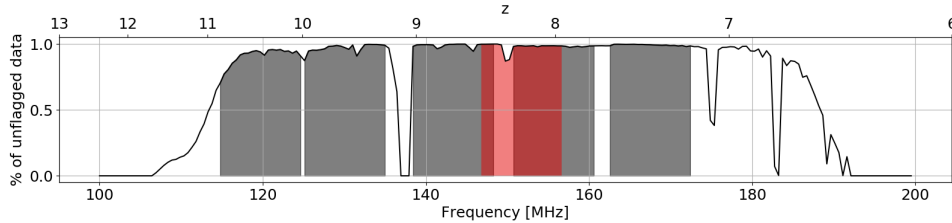
Figure 18: The frequency bands used in this analysis plotted over the total fraction of data not flagged in each frequency bin. All frequency bands used in this analysis have been shown. The red area near 150 MHz the $z = 8.37$ band used in C18 and A17. This redshift bin is included in order to properly compare with previous works, but it is worth noting the information obtained from this bin is not entirely independent from the two redshift bins with which it overlaps.

3.2 Data

For a complete review of the observation, reduction, and analysis steps of PAPER data prior to power spectrum estimation we refer to A15. We will provide a brief review below.

The PAPER 64 element array antennas were arranged in an 8×8 grid as illustrated in Figure 17. Due to the highly redundant configuration of this array, most of the observed sky power is captured by the three shortest baselines types. These are the same three baseline types used in A15, and are illustrated in Figure 17. These three baselines consist of a 30 m East/West baselines labeled here as "O" (the baseline analyzed in C18), a 30.3 m baselines with a positive North/South offset of 8° labeled at E+, and a 30.3 m baselines with a negative North/South offset of 8° labeled as E-. Three antennas (19, 37, and 50) have been flagged due to higher levels of spectral instability and were also flagged in A15. PAPER 64 observed for 135 nights between 2012 November 8 (JD 2456240) and 2013 March 23 (JD 24563745).

Data is first calibrated redundantly using log calibration and linear calibration techniques (Liu *et al.*, 2010, Zheng *et al.*, 2014, Dillon *et al.*, 2017). An imaging-based

flux density calibration is applied using Pictor A fluxes derived from Jacobs *et al.* (2013) as described in A15.

Calibration is followed by the application of a wide-band delay filter as described in Parsons *et al.* (2014) which uses a iterative deconvolution algorithm to model spectrally smooth sky components[5]. These smooth spectral components are then subtracted from the original visibilities (Parsons and Backer, 2009, Parsons *et al.*, 2014) followed by another round of RFI filtering to remove interference revealed below the level of the foregrounds. The foreground filtered and RFI flagged data is then binned in Local Sidereal Time (LST).

The final analysis step before power spectrum estimation is the application of a fringe-rate filter (FRF) as described in Parsons *et al.* (2016). This time domain filter passes modes with fringe rates corresponding to sky-like rates of motion. Each fringe rate is constant along a great circle on the sky making a cut through PAPER's wide primary beam. In the filter, each fringe rate bin is given a weight corresponding to the beam power integrated along the line of constant fringe rate. This weighting provides the highest possible coherent integration in time (Parsons *et al.*, 2016). In this way this type of integration can be thought of as performing an operation analogous to binning in uv space, albeit with a non-square grid. The filter also explicitly nulls zero fringe rates which are contaminated by cross-talk between antennas. We apply the optimal FRF as computed from the primary beam of PAPER. This contrasts the filter used in A15 which was slightly altered in shape to increase the number of final LST

---

[5]This process is referred to in other PAPER works as a "CLEAN-like iterative deconvolution." While the algorithm is based on the iterative modeling and subtraction image deconvolution algorithm (Högbom, 1974) here it is used in a one dimension sense to remove the convolution function induced by the finite Fourier transform and RFI flagging. Further clarification can be found in Kerrigan *et al.* (2018) where the use of the TH filter with CLEAN was recently revisited.
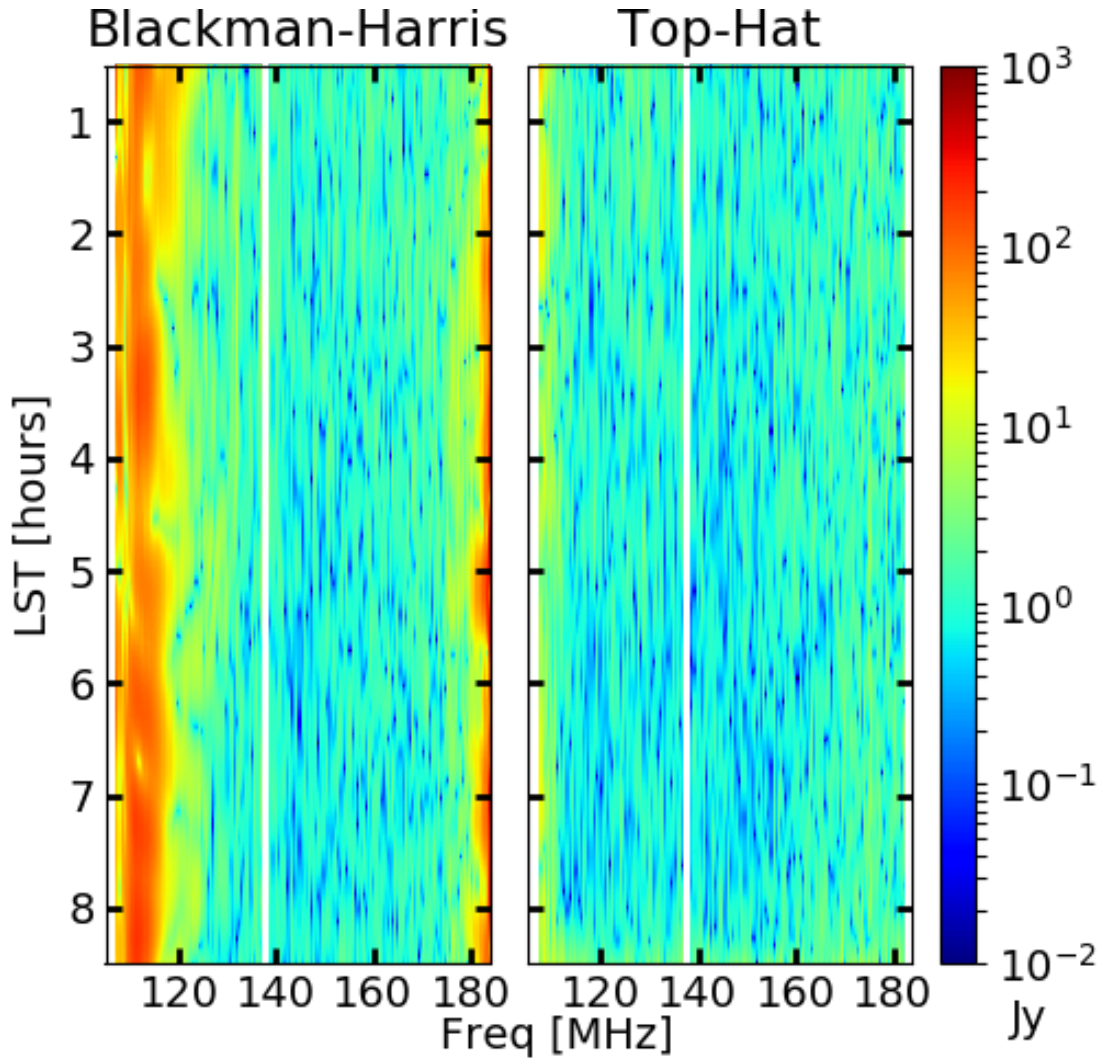
Figure 19: Waterfalls of visibility amplitude after application of two foreground filtering methods plotted versus LST and Frequency for a representative O type baseline (antenna pair 0 and 26). The difference is in the method of building a delay-space foreground model which has low leakage beyond the horizon. On the left a Blackman-Harris (BH) function was multiplied onto the spectra before delay filtering while data on the right have uniform weighting (Top-Hat or 'TH') but the iterative CLEAN algorithm has been used to build the delay model. The BH windowed data shows a sharp increase in amplitude near the band edges, a factor of 100 higher at the lower frequencies. This significant residual is a useful testing ground for foreground minimizing quadratic estimators but ultimately the TH window proves to be a simpler way to minimize foregrounds.

bins. The resulting total integration time of an LST bin after the application of the optimal FRF in this work is 3857 s.

For the power spectrum estimation in this paper, we select data from the LST range $00^h30^m00^s - 08^h48^m00^s$ for our analysis[6].

The previous PAPER multi-redshift analyses Jacobs *et al.* (2015) and Kerrigan *et al.* (in review) note that weighting spectra by a Blackman-Harris (BH) window before delay filtering provides low foreground residuals in the center of the PAPER bandpass (z~8). The BH weighting is favored because it minimizes sharp edges at the band edges giving a very high dynamic range delay space point spread function and therefor low leakage of delay modes beyond the horizon. Therefore the consequence of down-weighting the edge of the band is that the subtracted model performs poorly in those areas, particularly at low frequencies where foregrounds are the brightest. Kerrigan *et al.* (in review) notes success using uniform weighting across the full band (ie Top-hat or 'TH'). Figure 19 shows data from both wideband delay windows after the application of the FRF for the LST range used in this analysis. Both data sets show similar amplitude in the middle of the band (near $\nu = 150$ MHz) but the Blackman-Harris data shows a sharp increase in amplitude near the band edges while the Top-Hat data is roughly constant across the band. The ~ 2 orders of magnitude between the amplitude of both data sets below $\nu = 120$ MHz implies the TH windowed data is better suited for power spectrum estimation at high redshifts.

---

[6]Note that LST range here is slightly different from A15. Besides the LST range and the shapes of the FRFs applied in this work and A15, the data and processing prior to power spectrum estimation are identical.

Table 4: PAPER 64 Theoretical Noise Estimate Values

Term	Description	Value	Units
X^2Y	Conversion from interferometric (u,v,η) to cosmological $(k_{\perp,x}, k_{\perp,y}, k_{\parallel})^{\text{a}}$	$6.04 \times 10^{11} \left(\frac{1+z}{10}\right)^{2.5}$	$\frac{\text{Mpc}^3}{h^3\text{str GHz}}$
Ω_{eff}	Effective beam area[b]	$.74^2/.24$	str
T_{sys}	System Temperature	$180 \left(\frac{\nu\ [GHz]}{.18}\right)^{-2.55} + T_{rcvr}$	K
T_{rcvr}	Receiver Temperature	144	K
N_{lst}	Number of effective LST bins	8	
N_{sep}	Number of independent baseline types	3	
t_{int}	Integration time of LST bin[c]	3857	s
N_{days}	Number of effective days used in LST-binning	34	
N_{pols}	Number of polarizations combined in analysis	2	
N_{bls}	Number of effective baselines	42	

[a] This value is also a function of the assumed background cosmology. See Furlanetto *et al.* (2006) for more information

[b] The effective beam are is influenced by the choice of fringe rate filter applied(Parsons *et al.*, 2016). This value computation is also found in appendix B of Parsons *et al.* (2014).

[c] This value is computed as the Equivalent Noise Bandwidth (ENBW) of the FRF applied to the data. See C18 and Parsons *et al.* (2016) for more information

3.3 Power Spectrum Estimation

Even after foreground removal and FRF application, residual correlations between frequencies and LSTs can manifest as highly significant detections during power spectrum estimation. Since we believe our thermal noise limit exceeds the amplitude of a fiducial 21cm power spectrum by orders of magnitude, we assume these residuals do not result from cosmological signals but instead foregrounds and other systematics not removed during data processing.

One way to reduce these residual contaminations is with the Optimal Quadratic Estimator formalism originally adopted for the Cosmic Microwave Background power spectrum (Tegmark, 1997) and then adapted to 21cm by Liu and Tegmark (2011) and Liu *et al.* (2014a,b).[7] This type of estimator is discussed in the context of imaging type arrays Trott *et al.* (2012), Dillon *et al.* (2013), Dillon *et al.* (2015), and has served as the basis of PAPER results in A15, and C18.

The QE previously used in A15 defines an un-normalized power for between data sets $\mathbf{x}_1$ and $\mathbf{x}_2$ in the β-th k-bin, $\hat{q}_\beta$, as

$$
\begin{aligned}
\hat{q}_\beta &= \frac{1}{2} \left(\mathbf{R}_1 \mathbf{x}_1\right)^\dagger \mathbf{Q}_\beta \left(\mathbf{R}_2 \mathbf{x}_2\right) \\
&= \frac{1}{2} \mathbf{x}_1^\dagger \mathbf{R}_1^\dagger \mathbf{Q}_\beta \mathbf{R}_2 \mathbf{x}_2
\end{aligned}
\tag{3.1}
$$

where the $\mathbf{x}_1$ and $\mathbf{x}_2$ corresponds to odd and even Julian Dates respectively or vice versa, dagger indicates the complex conjugate and transpose operation, $\mathbf{R}_i$ is an arbitrarily[8] chosen weighing matrix for data vector i, and $\mathbf{Q}_\beta$ is a matrix operator which performs the Fourier transform along the frequency dimension of our data and bins the data into the β-th k-bin.

Since the QE formalism allows for a choice of weighting matrix, $\mathbf{R}$, to apply to time ordered data before power spectrum estimation, we use a regularized empirical covariance matrix to down-weight any residual foregrounds in our data. We choose

---

[7]The Quadratic Estimator can provide an estimate with a SNR that is theoretically the best one can do and is often referred to as an *Optimal* Quadratic Estimator. However this optimality requires exact knowledge of all cosmological and foregrounds signals, noise contributions and instrumentally induced correlations. Furthermore this optimality is only true in a narrow theoretical sense and should not be mistaken for a claim of broad optimality across all methods.

[8]This matrix can be chosen arbitrarily; however the power spectrum estimation must also be normalized later which depends on the choice of matrix. For an *Optimal* Quadratic Estimator, this matrix must be the true underlying covariance matrix.

the regularization

$$\mathbf{R} = (\mathbf{C}_{emp} + \gamma \mathrm{Tr}[\mathbf{C}_{emp}]\mathbf{I})^{-1} \qquad (3.2)$$

where $\mathbf{C}_{emp}$ is the empirically estimated covariance, $\mathbf{I}$ is the identity matrix, Tr is the trace operator, and γ is a scalar factor. The empirically estimated covariance is computed as

$$\mathbf{C}_{emp} = \langle \mathbf{x}\mathbf{x}^{\dagger} \rangle_{LST} \qquad (3.3)$$

averaged over the 8 hours of LST analyzed. This choice of weighting will down-weight any signals which correlate highly between frequency channels but will scale as the identity when there is little correlation. The use of empirical covariance weighting

We choose a scale factor γ to minimize the final power spectrum estimation after accounting for signal loss, as discussed in Section 3.1.4 of C18. The exact regularization used is set as $\gamma = 0.035$.

The OQE uses the true underlying covariance maxtrix $\mathbf{C}$ which requires *a priori* knowledge of all foregrounds, thermal uncertainties, and systematics. Estimating the covariance empirically fundamentally violates this assumption and as a result the covariance matrix can correlate otherwise statistically independent sky modes. This correlation will cause these modes to be down-weighted during power spectrum estimation resulting in signal loss (Switzer and Liu, 2014, Dillon *et al.*, 2015). When performing power spectrum estimation with an empirically estimated covariance matrix, additional analysis is required to identify and counteract signal loss. This is achieved in Dillon *et al.* (2015) through eigenmode filtering and by applying empirical covariance matrices not dependent on the data to which it is applied. In this work, we counter act signal loss through our choice of covariance regularization and signal injection simulations.

The foreground filtered data span the redshift range 12 to 6. The amount of evolution happening through this time is not known though constraints from EDGES high suggest that evolution is probably slower than a dz (total change in redshift) of 1-2 (Monsalve *et al.*, 2017). In the data set here, a practical limitation comes from a desire to avoid including channels with significant flagging. Bands with mostly continuous spectral sampling can be found if at the redshifts $z = 10.87$, 9.93, 8.91, 8.13, and 7.48 (119.7, 130.0, 143.3, 155.6, and 167.5 MHz respectively) in windows 10 MHz wide. These bands are illustrated visually in Figure 18.

As a validation check we also include a reprocessing of the $z = 8.37$ bin centered at 151.7 MHz which was analyzed A15 and C18. The only difference is that now three baseline types (as opposed to the single baseline type in C18) have been included.

3.3.1   Power Spectrum Uncertainties

Power spectrum errors can come from thermal, instrumental, and terrestrial (RFI) sources. Those with a known covariance (like thermal noise) can be propagated through the data processing and power spectrum estimation steps into an estimated error bar. The other sources are much harder to estimate from first principles. The net variance in the data can be estimated by bootstrapping, estimating many power spectra from subsets of data and then calculating the variance of these estimates. In the redundant PAPER array, the axis most amenable to bootstrapping is the selection of baselines which are cross multiplied to get a power spectrum.

Specifically,we randomly distribute and average individual baselines into 5 groups, then perform the power spectrum estimation by cross multiplying each combination of baseline groups. The final estimate is the average over all products and the time axis to

get a single spectrum vs k.[9] Repeat this process selecting different baseline groups to find new realizations of the power spectrum. The variance of these bootstrap samples is interpreted as the uncertainty in the power spectrum estimation. We perform this bootstrap estimation to probe the underlying distribution of allowed values given our observed values (Efron and Tibshirani, 1994, Andrae, 2010).

As discussed in Liu *et al.* (2014a,b), when estimating the power spectrum estimated in the regime $k_\parallel >> k_\perp$, the delay axis (the Fourier dual to frequency) can (to a good approximation) be re-interpreted as the cosmological $k_\parallel$ axis. As a result, following the derivation in (Parsons *et al.*, 2012) and usage in Pober *et al.* (2013, 2014), the theoretical uncertainty in the power spectrum estimate in the delay space can be written as

$$P_n(k) = \frac{X^2 Y \Omega_{eff} T_{sys}^2}{t_{int} N_{days} N_{bls} N_{pols} \sqrt{2 N_{lst} N_{sep}}} \tag{3.4}$$

where $X^2 Y$ converts from interferometric units to cosmological units, T_{sys} is the system temperature, Ω_{eff} is the effective size of the primary beam in steradians (Parsons *et al.*, 2014), N_{lst} is the number of independent LST samples, N_{pols} is the number of polarizations used in the analysis, t_{int} is the integration time of an LST sample, N_{days} is the effective number of days used in LST binning, N_{bls} is the effective number of baselines combined, and N_{sep} is the number of independent baseline types .

This equation does assume the uncertainty has no temporal dependence and the beam has no variation across the band where power spectrum is estimated. As an aid to future repeatability, the values used here are listed in Table 4. The calculation is documented as a python module called 21CMSENSE_CALC available at github.com/dannyjacobs/21cmsense_calc. See C18 for further discussion of this calculation and how it has been updated from A15.

---

[9]This technique is described in more detail in Section 3.2.2 of C18.

3.3.2 Signal Loss Estimation

One undesirable impact of many foreground mitigation strategies is the unintended removal of some fraction of desired background signal. In most cases the strategy is to measure the amount of loss using simulated data products. However in most cases the amplitude of the observed excess was significant at only a few sigma after integration over the entire season making it difficult to build a sensible model of foreground excess. One strategy that doesn't require a model of the data is to inject a simulated EoR-like signal into the data and ask the question of when that injected signal could be detected as a proxy for the actual underlying signal.

Under the QE framework when the foreground covariance is estimated using the same data providing the power spectrum answer, the signal loss has the potential for being very large. In C18 several factors were identified as contributing to a larger than originally estimated loss in the A15 power spectrum method. Most significant was that in the interpretation of signal injection cross terms between injected signal and data were assumed small, but are in fact large and negative. C18 provides a detailed analysis of the causes of signal loss and outlines a revised method for recovering power spectrum limits using injected EoR simulations.

The injection process is performed in parallel with the error bootstrap by adding a different realization of simulated 21cm signal into each bootstrap. Doing this for a range of injected power levels, one can construct the likelihood that the data are consistent with the injected power. Using Bayes' theorem, this likelihood can then be interpreted in the reverse to find the posterior probability of a range of 21cm power levels given the data.

Three power spectra are produced by this process:

I. A uniform weighted power spectrum (the result of a frequency FFT or using the identity as $\mathbf{R}$ in Equation F.2)

II. the uncorrected lossy power spectrum

III. an upper limit on injected power which is the 97.5% confidence limit on the posterior

The uniform weighted and lossy power spectra also provide useful consistency checks. Comparing the uniform weighted power spectrum to derived upper limit evaluates the effectiveness of the chosen weighting scheme at suppressing residual frequency-frequency correlations in the data. The lossy power spectrum can be used to check whether the variation in the output power spectra between different k-modes are consistent with thermal noise fluctuations around a predicted signal or around zero if no underlying signal is expected. This last check is useful in identifying bias in power spectrum estimation and determining the extent of signal loss between these points and the limits derived from the posterior. Other standard data products produced by the pipeline include all of these same outputs for a noise simulation which models the time and frequency dependent sampling of the lst-binned data set.

3.4 Multi-Redshift Power Spectrum Results

Power spectra at the selected redshifts are shown for two foreground filtering methods in Figure 20 and Figure 21, data points are given in Table 5.

Comparing the BH windowing Figure 20 with the TH windowing Figure 21 filtering, the advantage of the latter at low frequencies is immediately apparent. What is also notable is the regime in which QE weighting is effective.

Figure 20: The multi-redshift power spectrum estimators from the data which used a BH wideband window in delay filtering. All three baselines are combined in an unweighted averaged after power spectrum estimation. All error bars are 2σ. Data points are the output of the QE with $\mathbf{R}$ weighting and the limits are the 97.5% confidence limit of the posterior. Green lines indicate the theoretical thermal noise estimate for each redshift bin as computed with Equation 3.4. The weighted power spectra are computed using weighting in Equation 3.2 with the $\gamma = 0.035$. The dotted line indicates the horizon for a 30 m baseline or the light travel time between the antenna in each baseline. The uniform weighted power spectrum estimators exhibit a sharp rise in amplitude at the lower redshift bands. This corresponds to the band edges in Figure 19 where the amplitude of the data rises sharply. The $\mathbf{R}$ weighted QE successfully suppress these residual signals by multiple orders of magnitude in the $z = 10.87$ band and with less suppression in the $z = 9.93$ band. For the remaining redshift bands where the data amplitudes are lowest in the waterfalls, the upper limits from the $\mathbf{R}$ weighted QE shows no major improvements over the uniformed weighted QE outside of the horizon.
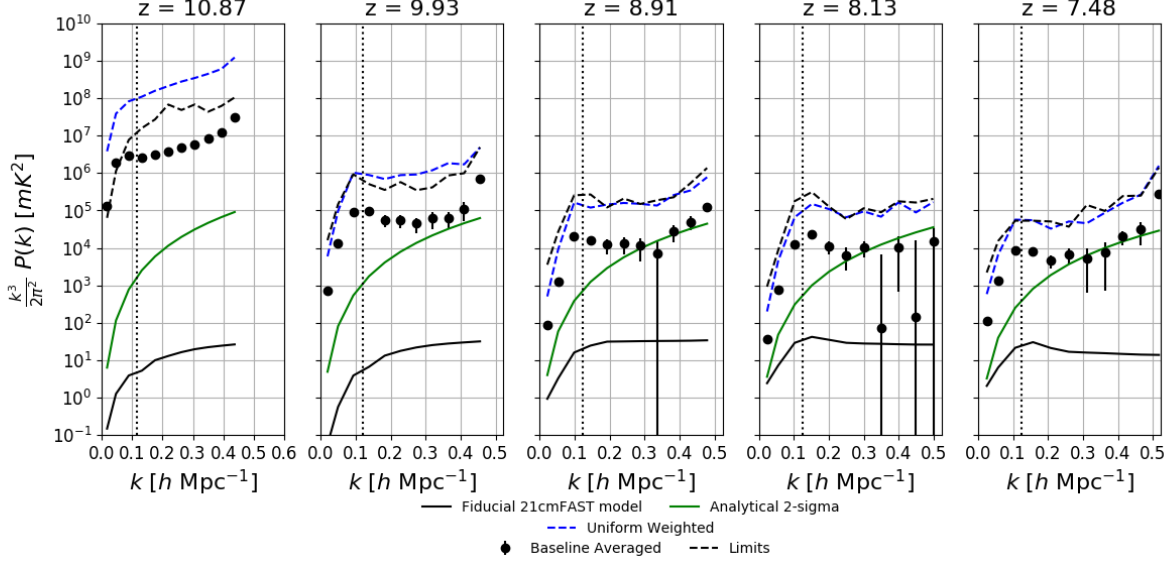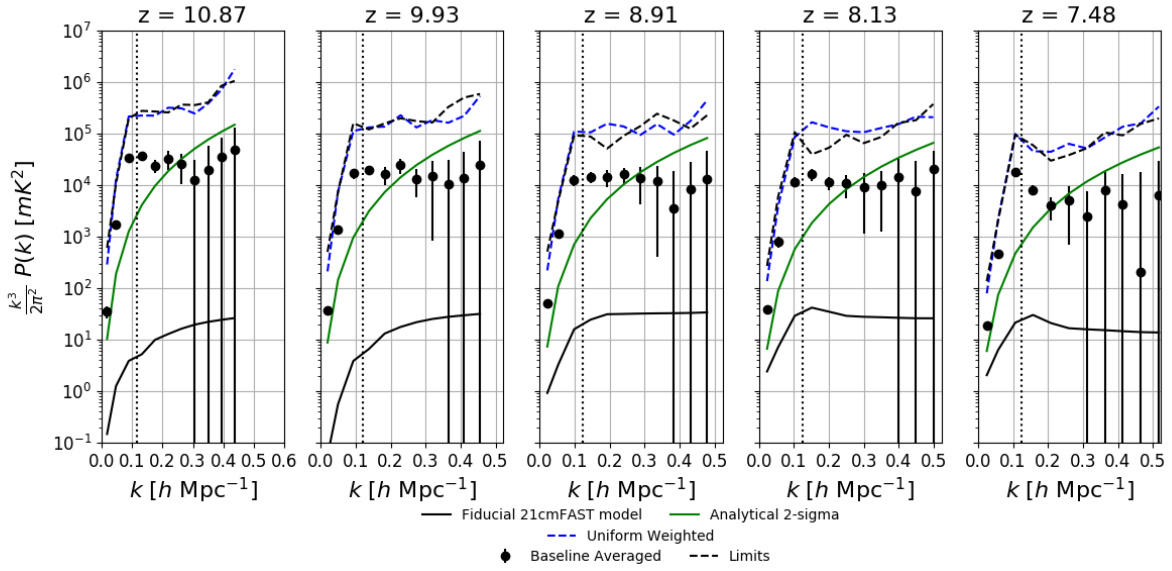
Figure 21: The multi-redshift power spectrum estimators from data which used a TH wideband window in delay filtering. All lines are the same as Figure 20 The uniform weighted power spectrum estimators show no large dependence on frequency. This is consistent with the relatively flat amplitudes of the data shown in Figure 19. Similar to the BH windowed data, the **R** weighted QE provides no major decrease in the upper limits compared to the uniform weighted power spectra above the horizon. The TH windowed data does show more k-bins consistent with zero at 2σ compared to the BH windowed data.

3.4.1 QE foreground mitigation

The foreground filtering used in C18 is windowed with a Blackman-Harris window function before being Fourier Transformed from frequency to delay space and the iterative deconvolution algorithm used to model smooth delay modes. In the three lowest redshift bands (all of which are near the center of the instrument bandwidth) the QE estimate improves on the unweighted estimate by only a small factor at best.

However, as was noted in Jacobs *et al.* (2016) for the BH window, significant residuals remain at the lowest frequencies. The amount of residual is apparent in

the uniform weighted power spectra which exhibit a sharp rise in amplitude at the highest redshift bands. This corresponds to the band edges in Figure 19 where the amplitude of the data rises sharply. Here, the $\mathbf{R}$ weighted QE successfully suppresses these residual foregrounds by multiple orders of magnitude in the $z = 10.87$ band and with less suppression in the $z = 9.93$ band.

Unsurprisingly, the "empirical covariance" QE method works best where foreground covariance dominates. The range of foreground residuals available spans a range of amplitudes from 10,000x to 10x the noise. At the highest power (in the $z = 10.9$ bin), the QE weighting is able to decrease the total power level by a factor of 50, however when foregrounds are closer to the noise, it is less effective.

3.4.2   Upstream foreground mitigation

Though the QE method is somewhat effective at reducing foreground bias its potency is limited in dynamic range as can be seen in Figure 21.

The uniform weighted power spectrum estimators show no large dependence on frequency. This is consistent with the relatively flat amplitudes of the data shown in Figure 19. Similar to the BH windowed data in the middle redshifts, the $\mathbf{R}$ weighted QE provides no major decrease in the upper limits compared to the uniform weighted power spectra. Additionally the TH windowed data shows more k-bins consistent with zero at 2σ compared to the BH windowed data.

3.4.3 Validation against C18

As a check on the repeatability of analysis, we also compute the power spectrum in the $z = 8.37$ redshift band analyzed in C18 and A15. The power spectrum estimators for both sets of data analyzed above are displayed in Figure 22. The upper limits presented here show a factor of ~ 10 increase in mK compared to those in A15. These levels are consistent with the analysis performed in C18 and the slight differences in the power spectra result from the inclusion of all three baseline types in this analysis compared to C18 with only used the O type baseline.

3.5 Discussion

Near the horizon ($k \sim 0.06\ h\ \mathrm{Mpc}^{-1}$), all power spectrum estimators have detections with high significance. As discussed above the relative amplitude of these detections is consistent with the shape of the broadband BH or TH weights applied in the foreground delay filter. However an interesting question remains: what is the origin of the excess occuring *well outside* the edge of the wedge? Consider the TH filtered power spectra which give, on average, the best limits. Beyond the horizon, the posterior limits are consistently higher than noise by an order of magnitude in mK^2. Yet the lossy power spectrum estimators are consistent with zero. Together these imply the variance in the data is larger than that expected purely from thermal fluctuation rather than some kind of bias or detection. The latter would manifest in the lossy power spectrum estimators being highly significant detections possibly with some discernible pattern as a function of k.

One possible source of this excess could be non-redundancy between baselines.
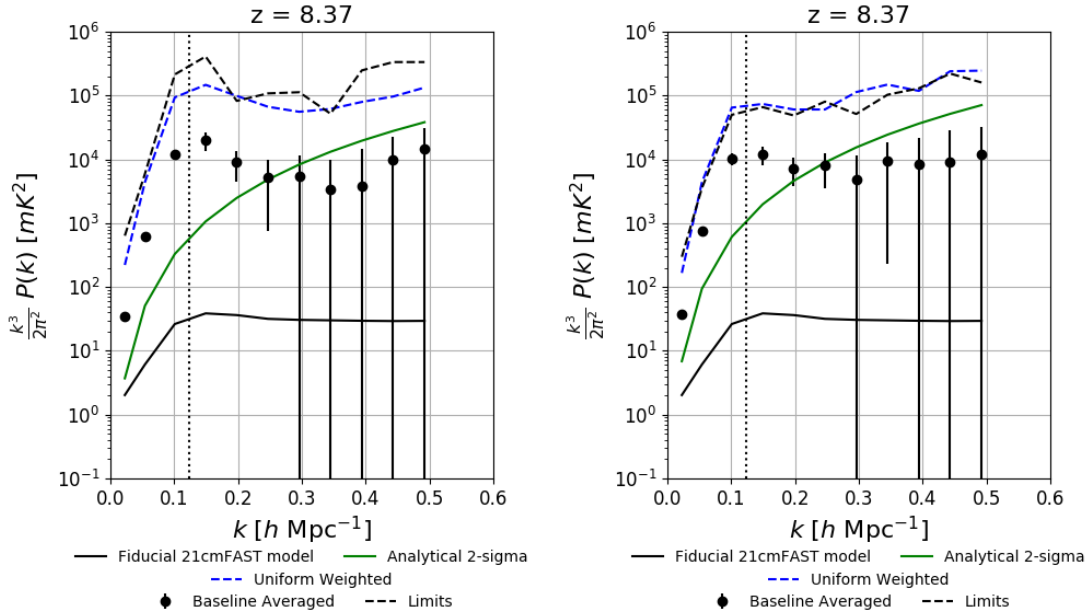
Figure 22: **Left:** The power spectrum estimator from data filtered using a BH window in the delay filtering. **Right:** The power spectrum estimator from data filtered using a TH window in the delay filtering. **In both figure:** The power spectra are combined in an unweighted averaged over all three baseline types. All lines are the same as in Figure 20. The BH wideband window is optimized for analysis in the band and as a result should slightly outperforms the TH window in the uniform weighted power spectra. The TH windowed data does however exhibit slightly lower power inside the horizon and as a result, the TH windowed data is used as the preferred windowing for the power spectrum estimation. Both sets of data have a similar number of k-bins consistent with zero, and similar to other redshift bands with low amplitude the **R** weighted power spectra show no major decrease in the upper limits compared to the uniform weighted power spectra.

Recall that antenna-based calibration by omnical assumes that all baselines are perfectly redundant, ie identical baseline vectors and primary beam responses to the sky.

Clearly there are foreground residuals, as evidenced by the significant detections just outside the wedge. Any deviations from redundancy would manifest as slightly different foregrounds. Each bootstrap selection baselines into groups would result

in different net foregrounds. When cross multiplying different groups together, the non-redundant foregrounds could be positive or negative variation resulting in large error bars in the bootstrap result.

While the QE can provide suppression of highly significant signals, foreground removal upstream of final power spectrum estimation shows improved performance over the QE. As such, it is prudent to optimize foreground removal in a data set to the redshift band of interest. This is evident especially in the $z = 10.87$ redshift band. The BH data displays a large amplitude in the uniform weighted power spectrum and the $\mathbf{R}$ weighted QE estimator produces limits ~ 2 orders of magnitude below the uniform weighted power spectrum limits. However, the uniform weighted TH power spectrum produces a limit a factor of 10 better than that.

The lowest upper limits in each redshift band, in the spatial scale range $0.3 < k < 0.6\,h\,\mathrm{Mpc}^{-1}$ are $(650\,\mathrm{mK})^2$, $(450\,\mathrm{mK})^2$, $(390\,\mathrm{mK})^2$, $(250\,\mathrm{mK})^2$, $(280\,\mathrm{mK})^2$, $(250\,\mathrm{mK})^2$ for the for the $z = 10.87$, 9.93, 8.91, 8.37, 8.13, and 7.48 redshift bands respectively. These upper limits represent a significant increase over prior limits published by the PAPER instrument (a factor of ~ 10 in mK) and supersede all previous PAPER limits. They also exceed the expected amplitude of a fiducial 21CMFAST[10] model by a factor or ~ 100 in mK (Mesinger *et al.*, 2011).

3.6   Conclusion

Using revised analysis methods we estimate the 21cm power spectrum in 5 redshift bins.

These results represent our highest confidence results and supersede all previous

---

[10]github.com/andreimesinger/21cmFAST

PAPER power spectrum results. This includes results from PAPER-32 (Parsons *et al.*, 2014, Jacobs *et al.*, 2015, Moore *et al.*, 2017) which used a different covariance estimation technique in their QE but have not been subjected to the rigorous re-analysis from C18. The constraints on spin temperature of Hydrogen made by Pober *et al.* (2015) and Greig *et al.* (2016) based on the previously published upper limits should also be disregarded. Though we do not place significant constraints on the IGM temperature, we would like to note their analysis will still be relevant should any future limits on the 21cm power spectrum be placed similar to the original limits from A15.

Though the limits have increased, because the error bars scaled proportionally the significance remains roughly the same. As before, the best limits have low significance foreground detections both inside and outside the EoR window. The origin of these weak sources of leakage remains an open question.

The current best limits from many 21cm experiments in the $k-$ranges reported by each instrument are displayed in Figure 23. With the inclusion of this work, the best limits from many experiments are all closely approaching 10^4 mK^2 across many redshifts.

To date, all power spectrum estimates have been reported as upper limits. However, to discern and characterize the physics of reionization, high significance detections of the 21cm power spectrum are necessary. Next generation radio telescopes, like the fully realized 350 element configuration of HERA (Pober *et al.*, 2014, DeBoer *et al.*, 2016, Liu and Parsons, 2016) and the future Square Kilometre Array (SKA; Mellema *et al.* (2013)), are predicted be able to make these detections and put stringent constraints on reionization.
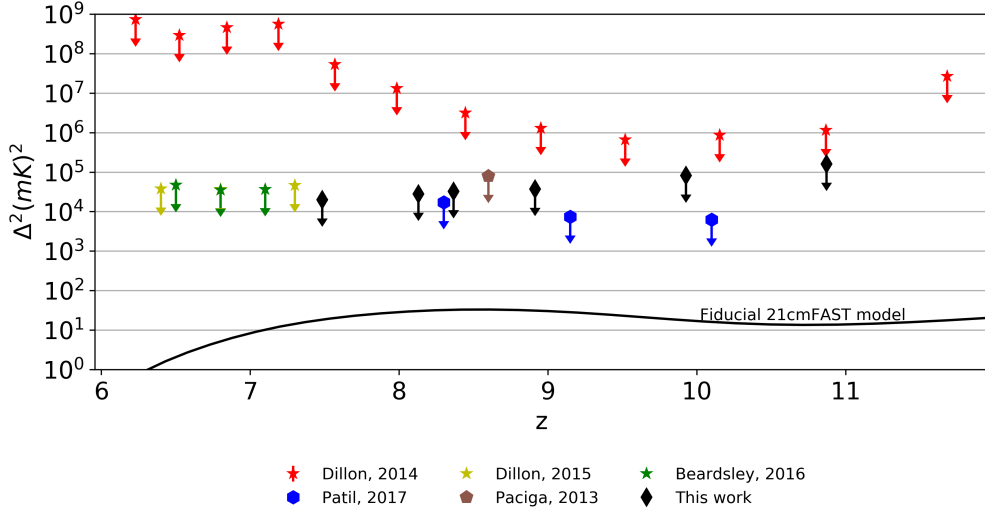
Figure 23: A comparison of the lowest limits achieved by various instruments in the k-ranges reported by each instrument. The results from this work are taken in the range $0.3 \leq k \leq 0.6 \ h \ \mathrm{Mpc}^{-1}$. Data is taken from the MWA (stars; Dillon *et al.* (2014, 2015), Beardsley *et al.* (2016)), the GMRT (pentagon; Paciga *et al.* (2013)) LOFAR (hexagons; Patil *et al.* (2017)) and PAPER (diamonds; This work). The addition of the data values from this work includes the $z = 8.37$ redshift bin analyzed in C18. It is worth nothing this redshift bin is not entirely independent from the $z = 8.13$ and 8.91 bins. This can be inferred from the overlapping window functions from Figure 18.

3.7 Acknowledgements

Table 5: PAPER Multi-redshift Power Spectrum Value

k	redshift	Δ^2	TE[a]	TS	TD[c]	B[b]	BS	BD[c]
$h\,\mathrm{Mpc}^{-1}$		mK^2	mK^2	σ		mK^2	σ	
0.1	10.86	36200	1300	57.89	Det	197600	0.37	Ulim
0.2	10.86	28000	10000	5.60	Det	268600	0.21	Ulim
0.3	10.86	56800	33800	3.37	Det	366000	0.31	Ulim
0.4	10.86	86000	80000	2.15	Det	403500	0.43	Ulim
0.5	10.86	232800	156300	2.98	Det	1057200	0.44	Ulim
0.1	9.92	25300	900	58.63	Det	158700	0.32	Ulim
0.2	9.92	22500	6900	6.52	Det	158000	0.29	Ulim
0.3	9.92	29600	23300	2.54	Det	175200	0.34	Ulim

Continued on next page

k	redshift	Δ^2	TE[a]	TS	TD[c]	BE[b]	BS	BD[c]
$h\,\mathrm{Mpc}^{-1}$		mK^2	mK^2	σ		mK^2	σ	
0.4	9.92	52600	55200	1.91	ULim	327800	0.32	Ulim
0.5	9.92	148200	107900	2.75	Det	589200	0.50	Ulim
0.1	8.91	13300	600	47.49	Det	92600	0.29	Ulim
0.2	8.91	11900	4500	5.32	Det	51200	0.47	Ulim
0.3	8.91	27300	15100	3.61	Det	139700	0.39	Ulim
0.4	8.91	32900	35900	1.83	ULim	180800	0.36	Ulim
0.5	8.91	60500	70100	1.73	ULim	226900	0.53	Ulim
0.1	8.36	10400	500	45.99	Det	49800	0.42	Ulim
0.2	8.36	8600	3600	4.71	Det	48700	0.35	Ulim
0.3	8.36	12200	12300	1.99	ULim	51400	0.47	Ulim
0.4	8.36	21500	29100	1.48	ULim	129500	0.33	Ulim
0.5	8.36	44300	56700	1.56	ULim	159900	0.55	Ulim
0.1	8.12	10600	400	51.71	Det	106600	0.20	Ulim
0.2	8.12	10600	3300	6.44	Det	53300	0.40	Ulim
0.3	8.12	15100	11100	2.72	Det	65300	0.46	Ulim
0.4	8.12	36300	26400	2.75	Det	161500	0.45	Ulim
0.5	8.12	64200	51500	2.49	Det	374500	0.34	Ulim
0.1	7.48	16700	300	106.76	Det	94800	0.35	Ulim

k	redshift	Δ^2	TE[a]	TS	TD[c]	BE[b]	BS	BD[c]
$h\,\mathrm{Mpc}^{-1}$		mK^2	mK^2	σ		mK^2	σ	
0.2	7.48	5300	2500	4.24	Det	29800	0.36	Ulim
0.3	7.48	12900	8500	3.05	Det	52000	0.49	Ulim
0.4	7.48	27300	20000	2.73	Det	92600	0.59	Ulim
0.5	7.48	51100	39100	2.61	Det	197700	0.52	Ulim

The table column names are defined as follows: TE - Theoretical Error, TS - Theoretical Sigma, TD - Theoretical Detection, BE - Bootstrap Error, BS - Bootstrap Sigma, BD - Bootstrap Detection

All data in this table comes from the Top-Hat windowed data.

The lowest limits achieved by PAPER-64 combined from both filtering techniques. The "theoretical error" is the Analytic 2 sigma (green line) from Figure 21, bootstrap error comes from the errorbars from the same figure as the filter in the table. Theoretical detection column values are Det(detection) if the significance of the values of Δ^2 is greater than 2σ when compared to the theoretical error at a 1σ level. The bootstrap detection column is the same but significance computed with the bootstrap error bar.

[a] Theoretical Error calculated with Equation 3.4.

[b] All error bars are 2σ.

[c] Det indicates a measurement and error-bar inconsistent with zero, ULim indicates consistency with zero at 2σ.

Chapter 4

OPTIMIZING LOW FREQUENCY ARRAY DESIGN

As foregrounds are observed through the instrument additional chromatic effects manifest in the 2-Dimensional power spectrum space in what is colloquially called "the wedge."

The exact shape and extent of these foreground modes are strongly dependent on instrument configuration and can be mitigated through optimizing antenna placement and spectral stability. Here I investigate the degree to which foregrounds contamination can be minimized through array design. Essentially this sections asks the question: "is it possible to build a radio interferometer that is insensitive to foregrounds?" I begin by reviewing what constitutes foregrounds for these arrays, and constructing metrics to compare the performance of different arrays.

The radio sky is dominated by Synchrotron emission from our Galaxy. This signal is present at levels 4 to 5 orders of magnitude greater in brightness temperature than the underlying cosmological signal 21cm experiments aim to observe (Morales and Wyithe, 2010, Pritchard and Loeb, 2012). This foreground emission is spectrally smooth compared to the expected structure of the underlying 21cm signal and given no further assumptions, it should be possible to separate these two signals in the Fourier Space dual to frequency.

This effect is illustrated by the cartoon in Figure 24. The spectrally smooth foregrounds dominate emission from the EoR by orders of magnitude at low frequencies. When moving to Fourier Space, after applying a Blackman-Harris window, the EoR signal becomes discernible at high Fourier modes.
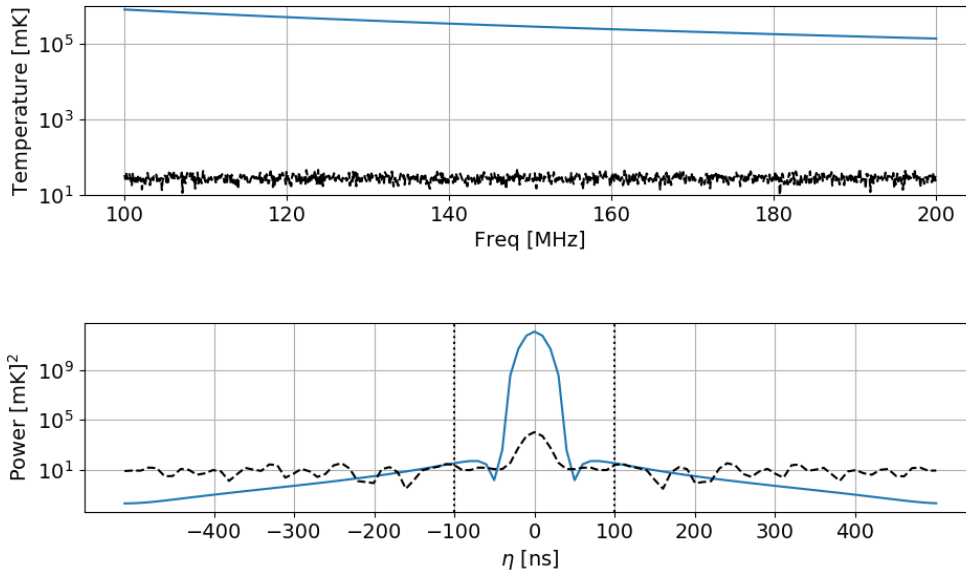
Figure 24: A cartoon depicting how EoR signal can be discerned from the dominating foreground emission. In both images, blue represents the spectrally smooth diffuse foregrounds and black is the underlying EoR signal.
Top: The spectrally smooth foregrounds dominate emission from the EoR by orders of magnitude at low frequencies.
Bottom: Power from both the EoR signal and the foreground plotted on a logarithmic axis. Power is calculated after applying a Blackman-Harris window, and a Fourier Transform over a 10 MHz band centered at 150 MHz of the toy model in the upper panel. Despite the orders of magnitude difference in the emission of the foreground, the EoR signal becomes discernible at high Fourier modes.

Many analysis pipelines attempt to exploit this fact in what is known as a "foreground avoidance" power spectrum estimation technique (Dillon *et al.*, 2013, Parsons *et al.*, 2014, Trott, 2014, Ali *et al.*, 2015, Dillon *et al.*, 2015, Jacobs *et al.*, 2016, Trott *et al.*, 2016). However by intentionally omitting modes significant sensitivity is lost. Perhaps even more significant, the highly chromatic filter used in some of these pipelines also removes power from the desired signal in both a frequency and scale dependent way. This is particularly detrimental to imaging and cross-correlation applications (Beardsley, 2015).

The ideal theoretical case quickly becomes complicated by actual observations. Through numerous kinds of "instrumental mode mixing" (Bowman *et al.*, 2009, Parsons *et al.*, 2012) the low Fourier modes to which foregrounds are theoretically confined leak to higher k-modes. This effect has been observed in both simulation and observations (Datta *et al.*, 2010, Morales *et al.*, 2012, Vedantham *et al.*, 2012, Trott *et al.*, 2012, Hazelton *et al.*, 2013, Pober *et al.*, 2013, Thyagarajan *et al.*, 2013, 2015b,a, Pober *et al.*, 2016, Barry *et al.*, 2016). The sampling density in the (u, v) plane also directly influences the the variation of information caused by "Multi-Baseline Mode Mixing" (Hazelton *et al.*, 2013), an effect where a small number of samples can bias power spectrum estimation in gridded pixels.

4.1   Assesing Chromatic Foregrounds in Fourier Space

Observations of otherwise spectrally smooth foregrounds can gain spectral structure from a number of effects (e.g. a variable bandpass with ripples) but the largest contributing factor is simply due to the arrangement and density of antennas. This dependence can be more intuitively understood by considering a simple exercise of two baselines.

Each baseline inherently samples a Fourier mode of the sky image. When these modes are combined together on a grid the sky can be reconstructed through a Fourier Transform. The contribution to the phase of the visibility from each source measured depends on the source's position in the sky and also on the apparent length of each baseline in wavelengths. The apparent length of a baseline, $|u|$, is the physical separation of the antennas, $|b|$, measured in wavelengths ($|u| = |b|\frac{\nu}{c}$). This effect is illustrated by the cartoon in Figure 25
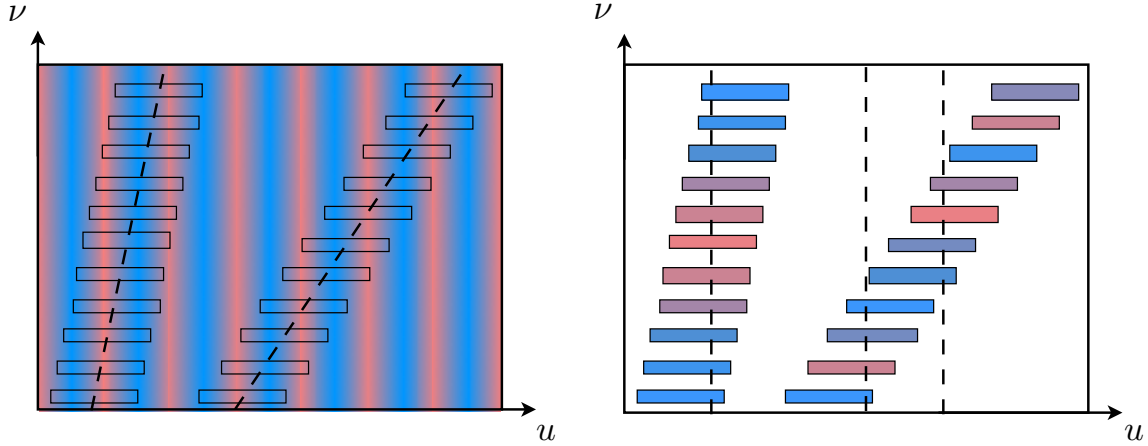
Figure 25: A cartoon illustration of how baselines measure different Fourier Modes with frequency. For both images the baseline lengths in wavelengths (dashed black line) is plotted as a function of frequency. Overplotted on each baseline are representative boxes of the frequency sampling of an instrument.
LEFT: Baselines measure different mode and variation of the underlying signal with frequency.
RIGHT: Plotted here are the representative values measured by each baseline gridded into the uv plane. Fourier Transforms are taken directly along the frequency axis. Variations in the sampling of the underlying source structure casued by poor uv-sampling causes power to leak towards high k-modes. Figure adapted from Morales *et al.* (2012) and Beardsley (2015)

For the remainder of this discussion, it is sufficient to consider how the wedge develops from the basic sampling of baselines in the (u, v, f) cube and how it affects the Fourier Transform from frequency to $k_\parallel$ space. While this analysis is performed explicitly in power spectrum estimation in this work, the goal is to minimize foregrounds to enable high fidelity imaging with minimal mode loss.

Any deviations from a perfect spatial sampling function creates spectral variation in the (u, v, f) cube which has strong dependence on baseline length. Grid points in the (u, v, f) cube can be occupied (or not) as a function of frequency depending on the configuration of baselines in the array. The coherent addition of different baseline types can lead to high sampling density in some areas of the (u, v, f) cube and low

sampling density in areas where only a few baselines are present. For very short baselines, the grid can be fully occupied along the frequency axis with a single baseline. For longer baselines, where coverage is sparse, moving along the frequency axis at a constant (u, v) coordinate will transition between areas which have sampling to those that do not, causing signal variation along the Fourier Transform axis. Several power spectrum analyses have shown that a (u, v) coverage with large gaps lead to significant correlation across all $k_\parallel$ modes (Beardsley *et al.*, 2016, Jacobs *et al.*, 2016). However, even in situations where the (u, v) coverage is "filled," small variations in sampling density along the frequency axis can cause significant foreground contamination in the wedge.

The amount of leakage observed by Imaging type power spectra estimation can be combated by increasing the baseline sampling density throughout the (u, v, f) cube. Developing future radio arrays to uniformly sample the (u, v) plane across all observed frequencies would provide passive, powerful foreground mitigation.

4.2 Array Optimiation Limitations using Existing Pipelines

Foreground simulations propagated through a given instrument are the standard method for predicting an array's expected foreground contamination. This consists of producing time ordered visibilities for all relevant sources (e.g. diffuse galactic emission, point sources catalogs) and reducing these visibilities through an analysis pipeline. These pipelines will grid the visibilities in the (u, v) plane and calculate a power spectrum.

Properly computing and accounting for important effects which can cause foreground leakage requires the full observational pipeline to be accurately modeled to

one part in 10^5 or better (the scale difference of foreground emission to expected EoR signal). As a result, even minuscule effects, like the precession of sources due to the nutation of the Earth's rotational axis(Morales URSI 2018), effectively mapping the beam and modeling sources outside the main lobe (Pober *et al.*, 2016), and even catalog completeness and calibration technique (Barry *et al.*, 2016) can cause significant differences in the power spectrum.

Even some computational choices can cause unforeseen effects in the power spectrum. For example, it has recently been observed that the Fast Holographic Deconvolution (FHD[11]; Sullivan *et al.* (2012)) package used in MWA analysis has increased leakage due to clipping the beam model in (u, v) space without letting the beam go smoothly to zero. However, letting the beam extend infinitely in the (u, v) is also infeasible computationally and practically. Approximations intended to ease computation complexity at the expense of (minimal) precision are becoming themselves sources of foreground leakage.

Other complications arise when considering the computational cost of large scale simulations. The computation time required to perform such simulations and analyses can quickly become impractical. On a 24 core machine, a 127 element array arranged like HERA (a hex dithered into three rhombus shards) observing the GLEAM all sky catalog for a 10 minute observation over 30 MHz bandwidth simulated with PRISIM[12] requires over 350 cpu-hours and 300 GB of RAM. Even simulating only the unique baseline types, the time required scales like the number of unique baselines up to a total of N_{ants}^2 for an array with minimal redundancy. Power spectrum estimation by FHD and the Error Propagated Power spectrum with InterLeaved Observed Noise

[11]github.com/EoRImaging/FHD

[12]github.com/nithyanandan/PRISim

94

(εPPSILON[13]; Jacobs *et al.* (2016), Hazelton *et al.* (in prep)) computes the power spectrum estimation from HEALPIX[14] (Górski *et al.*, 2005) images output by FHD. This process requires multiple Discrete Fourier Transforms (DFTs) from the flat (u, v, f) space into curved sky image[15] by tracking different channels of data[16]. For the simulations analyzed here, we produce no sky model or residual and therefore track 6 data channels (an observation, weights, variance each for even and odd JDs). For large images (like those made from radio instruments able to observe the whole sky) these DFTs can take 30+ hours each, adding additional complexity to the simulation pipeline. This DFT time is measured directly from both FHD and εPPSILON and scales based on the size of the sky image made and the number of HEALPIX pixels used to store the image.

In an attempt to model the expected time for a complete simulation

$$t_{sim} = t_{prisim} + t_{FHD} + t_{eppsilon} \tag{4.1}$$

we'll make an assumption that computations can be completed continuously without delay[17], so the speed of operations, v_{ops}, is equivalent to the cpu clock speed. The

---

[13]github.com/EoRImaging/Eppsilon

[14]http://healpix.sourceforge.net

[15]This process is not exactly a DFT, but is closely approximated by one. The actual computation is a calculation of the correlation of the Green's Function of Electromagnetic wave propagation between two observation points (the antenna positions) from a wave originating at infinity. The exact form and computation are derived in Clark (1999).

[16] A power spectrum is generally formed from a splitting of even and odd Julian days mutliplied together. Both even and odd now have one an observation, a sky model, a residual image, the (u, v) weights and variance.

[17]This assumption will lead to an underestimated simulation time. The computations would actually rely on the Duty Cycle time for a cpu as well as computation speed; however it makes our model much simpler.

PRISIM simulation must simulate a visibility for each combination of source (or sky pixel on a HEALPIX map), frequency, and time for each baseline in an array. This requires

$$t_{prisim} = \frac{N_{src} * N_{freqs} * N_{times} * N_{ants}^2}{v_{ops}} \tag{4.2}$$

time to complete a simulation. Where N_{src} is the number of sources, N_{freqs} is the number of frequency channels, N_{times} is the number of time samples, N_{ants} is the number of antennas, and v_{ops} is the cpu clock speed.

Next assume that FHD will grid a visibility for each frequency, time and baseline with a kernel of size $N_{FHD\ pix} = 100$ pixels per side. This gridding is accompanied by an DFT from the (u, v) plane onto a HEALPIX sky for each data channel mentioned above. This computation requires

$$t_{FHD} = \left(\frac{N_{ants}^2 * N_{freqs} * N_{times} * N_{FHD\ pix}^2}{v_{ops}} + t_{DFT} \right) * N_{channel} \tag{4.3}$$

where $N_{channel}$ is the number of data channels, N_{pix} is the number of pixels in an FHD (u, v) plane and t_{DFT} is the time required for an FHD DFT.

Finally that εPPSILON only performs DFTs from the sky image into power spectrum space

$$t_{eppsilon} = t_{DFT} * N_{channel} \tag{4.4}$$

where t_{DFT} is the time for one DFT measured before and $N_{channel}$ is the number of DFTs required for εPPSILON (again one for each data channel). The time for these DFTs is dependent on the choices made in FHD concerning how large of an image to make. Assuming the same size image is produced for every simulation, this is a constant.

Combining these approximations, a model of the expected computation time for the simulation described above for varying number of antennas, a HEALPIX map with
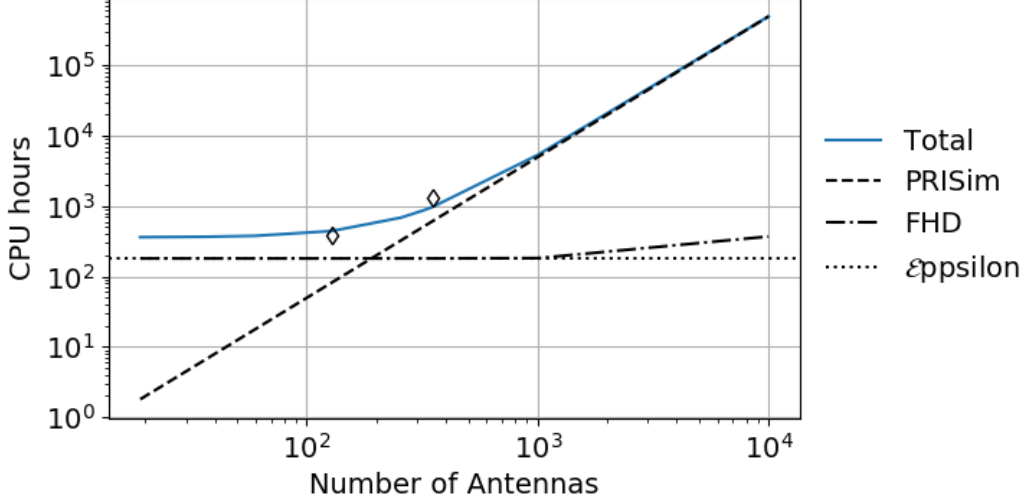
Figure 26: The expected simulation time for varying array sizes for and all sky image of the GLEAM point source catalog observed for 10 minutes of a 30 Mhz bandwidth centered at 150 Mhz on a machine with a cpu speed of 3250 Mhz. Both array simulation (dashed black) and the gridding and image making (dash-dot black) require computations scaling as N_{ant}^2. Large N_{ant} arrays will require computations completed by computing clusters. Over plotted are two measured simulation times for a HERA-128 array (384 cpu-hours) and a HERA-350 (1320 cpu-hours).

NSIDE=512 sources, 308 frequency channels, and 60 time integrations is displayed in Figure 26 on a machine with a cpu speed of 3250 MHz. The scaling for a simulation similar to this would depend on the input source catalog and the size of the sky image produce. For a smaller catalog, the required time will decrease significantly. Similarly, making a smaller sky image would provide a reduction in the time required for each DFT. The total time required quickly becomes dominated by the computations depending on the number of baselines (N_{ants}^2) for very large arrays. These time also assume no initialization, or I/O time which only increases the final result.

Future array design would be impeded by requiring large amounts of time and memory or supercomputer access to evaluate the potential benefits of different configuration

for a large number of antennas. These pipeline components are all under continual development to add new features like parallelization and optimization. However, since the principal source of foreground leakage is the array configuration and response in the (u, v) plane, it is worthwhile and can increase efficiency to explore metrics based only on how an array's aperture samples the (u, v) plane. Such metrics do not require all simulation pipeline elements, and as a result greatly reduce the computation time required to evaluate multiple array configurations.

4.3   Qauntifying Wedge Leakage and Instrument Chromaticity

Given the various complications to conducting full instrument simulations and the emphasis on an array's aperture sampling in the (u, v) plane, it is necessary to construct a representative proxy metric. The ideal metric allows array configurations to be ranked on their foreground performance using only basic design parameters: antenna positions and antenna beam. The metric must also be approximately calibratable against real simulations. Finally, the metric will likely be used in optimization loops by future array designers so it should be not be computationally intensive.

One possible leakage metric is described in the following Section 4.3.1. This discussion is accompanied by the results of some simulations of different array configurations. Section 4.3.2 discusses how this same metric can be applied to the sampling density of an instrument in power spectrum space.

4.3.1 Wedge Leakage

In a theoretical array which completely and uniformly samples the electromagnetic field, foregrounds are confined to the $k_\parallel = 0$ bin (DC bin, bandwidth limited region) of a power spectrum estimation. Comparing the power at $k_\parallel = 0$ to the power above $k_\parallel = 0$ can provide and estimate of the relative amount of power leaking into the wedge. Bins where the ratio is large would indicate high power leakage, while those with low ratios indicate bins with minimal leakage. The power above the $k_\parallel = 0$ bin represents power from the foregrounds which has been leaked into these modes from the addition of spectral structure. An ideal power spectrum from a spectrally smooth foreground will have all power in the $k_\parallel = 0$ and the ratio described above would be uniformly zero.

This section investigates the hypothesis that wedge leakage, even in densely packed arrays, depends on the uniformity of the aperture sampling function. One such dense array is HERA which has 14 m dishes arranged in a hexagonal face-packed lattice shown in Figure 27. This array is highly redundant with a (u, v) response strongly peaked at the shortest antenna spacing. A variation in this design has HERA broken into three rhombus-shaped shard each offset along cardinal directions thus increasing the (u, v) sampling of array, also shown in Figure 27.

The first step to testing this hypothesis is to quantify the amount of leakage occurring in full simulations. The PRISIM package is used to simulate a 10 minute observation of the GLEAM point source catalog over a 30 MHz bandwidth centered
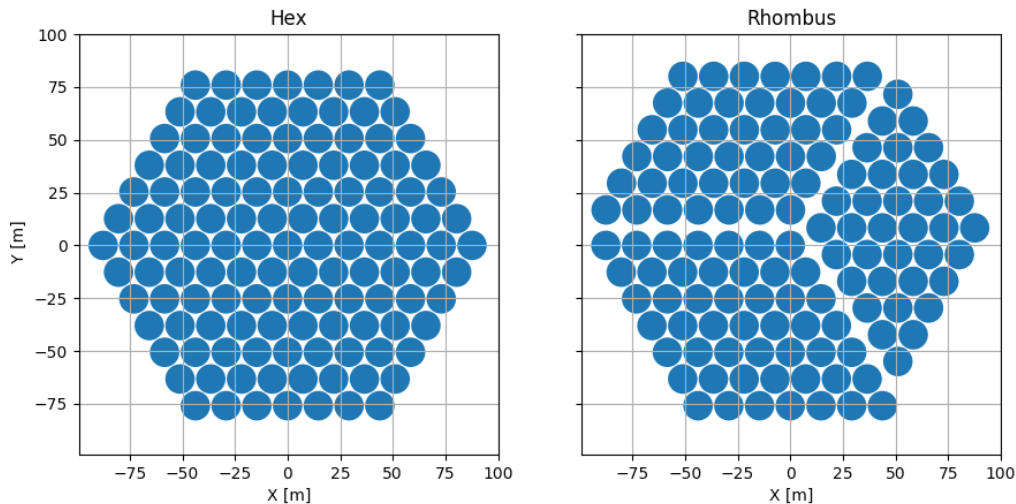
Figure 27: Two HERA-like antenna configurations used in these simulations. Both arrays consist of 14m dishes with .6m spacing between adjacent dishes.
LEFT: The compact hexagon, referred to as Hex in this work.
RIGHT: A hexagon dithered into three distinct sub-groups. Referred to as Rhombus in this work.

at 150 MHz. These simulations are gridded and imaged in FHD, and finally the images are used to perform power spectrum estimation in εPPSILON[18].

The 2-Dimensional, P($k_{\parallel}$,$k_{\perp}$), power spectra from these simulations are shown in Figure 28. Initial comparisons by eye cannot easily discern the difference between the two spectra due to the extreme dynamic range. However, the difference is clearly visible in the ratio of power inside and outside the bandwidth limited region. These ratios are shown in Figure 29. Both arrays appear comparable at low $k_{\perp}$, but the Rhombus array shows noticeably less fractional power outside the bandwidth limited region in the range $0.01 < k_{\perp} < 0.04\ h\ \mathrm{Mpc}^{-1}$. This range coincides with the area

---

[18] The package PYUVDATA (Hazelton *et al.*, 2017) is used to standardize output format from PRISIM and the input of FHD
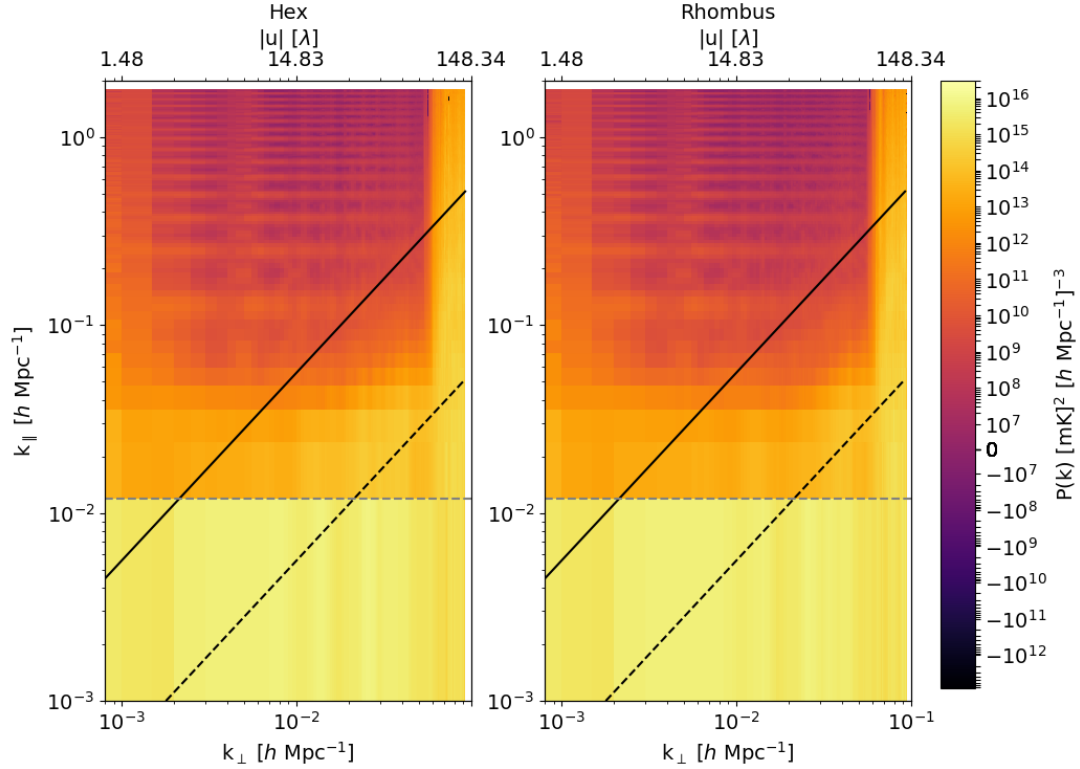
Figure 28: The 2-Dimensional power spectra from the two HERA arrays show in Figure 27. The solid black line indicates the horizon, the dashed black line is the 9 degree FoV of the simulated antennas. The Dashed grey line indicates the barrier of the bandwidth limited region ($k_{\parallel} = 0$ bin, computed by converting $1/B$ into $k_{\parallel}$ where B is the bandwidth of the simulation). Initial comparisons by eye cannot easily discern the difference between the two spectra due to the extreme dynamic range.

where the wedge is expected to leak the most for these arrays. The sharp rise in fractional power near $k_{\perp} = 0.06h$ Mpc^{-1} occurs where both arrays are no longer sensitive to sky modes (the region bounded by the maximum baseline length).

Based on these two arrays, the use of fractional power outside the $k_{\parallel} = 0$ bin compared to the power inside the $k_{\parallel} = 0$ bin may be a successful metric to predict the foreground contamination of an array. More simulations of varying array configurations are necessary to fully evaluate this metric's ability to quantify foreground leakage but
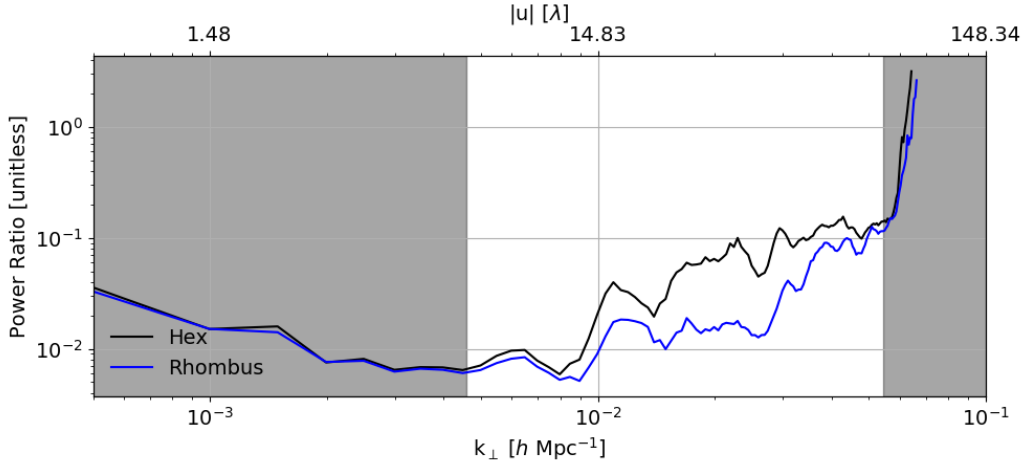
Figure 29: The ratio of total power above $k_{\parallel} = 0$ to power at $k_{\parallel} = 0$ for the two simulated power spectra in Figure 28. Both arrays appear comparable at low $k_{\perp}$, but the Rhombus array shows noticeably less total power outside the bandwidth limited region in the range $0.01 < k_{\perp} < 0.04 \ h \ \text{Mpc}^{-1}$. This range coincides with the area where the wedge is expected to leak the most for these arrays. The sharp rise in fractional power near $k_{\perp} = 0.06 \ h \ \text{Mpc}^{-1}$ occurs where both arrays are no longer sensitive to sky modes (the region bounded by the maximum baseline length). The gray regions indicate areas where there are no baselines sensitive to these cosmological modes.

the remainder of this work will assume this is a representative metric of foreground leakage.

4.3.2 Instrument Chromaticity

Given a metric which allows us to rank full-sky/instrument simulations, the next step is to find a similar metric based only on the instrument configuration. This metric must, as discussed early, capture the (u, v, f) variation but also be easily computable. A natural choice is to calculate the gridded (u, v, f) weights in this space with as few approximations as possible. The weights are the cumulative response function of an

array to each Fourier Mode measured on the sky. The concept of this calculation is simple, grid the electromagnetic response of each baseline on to the (u, v) plane at each observed frequency. Fourier Transform the sampling density along the frequency dimension, multiply by the complex conjugate and average radially in bins of constant $u^2 + v^2$. This produces the Point Spread Function (PSF) of the instrument in power spectrum space, or the response of the instrument in the power spectrum domain. To accomplish this, an accurate model of the beam for each baseline (or for individual antennas) is required. Transforming this sky plane beam into the (u, v) plane is not without challenges as well. The beam model is pixelized, and information of the response pattern at scales comparable to and smaller than the pixel size will be lost. The size and shape of the pixels themselves can alter the Discrete Fourier Transform (DFT) from the sky plane to the (u, v) plane. The advantage to pixelated maps, such as a HEALPIX map, is the easy manipulation of beam models (rotations, masking, etc) and well defined geometric relations for computing the DFT over the desired pointing (e.g. only transforming the response to the sky above the horizon).

Producing a fully gridded $(u.v)$ weight or baseline sampling density, with as few approximations as possible, appears computationally difficult, but this difficulty arises from the choices of computational approximations versus theoretical exactness. Ideally this computation should be performed with as few approximations as possible, and the treatment of the beam can prove to be the most difficult part of this limit.

Since the beam pixelization offers a choice in pixel size, it is worthwhile to investigate the effects of the size and shape of a HEALPIX pixel by calculating the (u, v) response of the primary beam for multiple HEALPIX pixelization. A delta function is gridded on to the (u, v) plane at $(u, v) = (5\lambda, 0)$. A DFT is performed to transform this delta function into a sine wave on a HEALPIX map and another DFT is performed
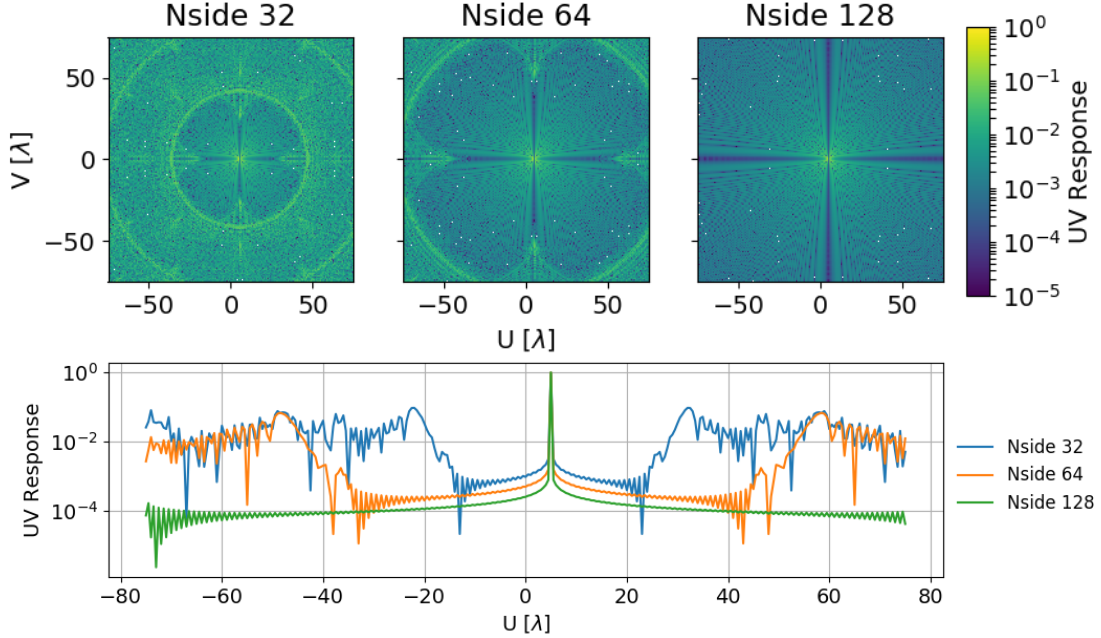
Figure 30: The results of gridding a delta function in the (u, v) plane, performing a DFT to a map and back again. The resulting power in the (u, v) plane represents the kernel of the pixel in this space.
TOP: The 2-Dimensional images of the (u, v) plane after calculating the (u, v) response of the HEALPIX pixels for different N_{side} values. The sidelobes of the pixel kernels move to larger $|u|$ values for smaller pixels.
BOTTOM: A 1-Dimensional cut along the axis $v = 0$ of the HEALPIX kernel for each N_{side} value. The sidelobes of the kernel roughly correspond with the average size scale of a pixel $\sim 30\lambda$, $\sim 60\lambda$, $\sim 120\lambda$ for $N_{side} = 32$, 64, and 128 respectively. The dynamic range is also improved for higher resolution maps.

on the HEALPIX map to convert the map back to the (u, v) plane. The resulting deviation from the ideal delta function in the (u, v) plane provides information on the kernel of a HEALPIX pixel.

The delta function and pixel kernel, along with a one dimensional slice of this kernel, are shown in Figure 30. The approximate average size of a HEALPIX pixel corresponds to a maximum size scale of ~ 30, ~ 60, and ~ 120 wavelengths in (u, v) space for the $N_{side} = 32$, 64, 128 respectively. This roughly corresponds to the first
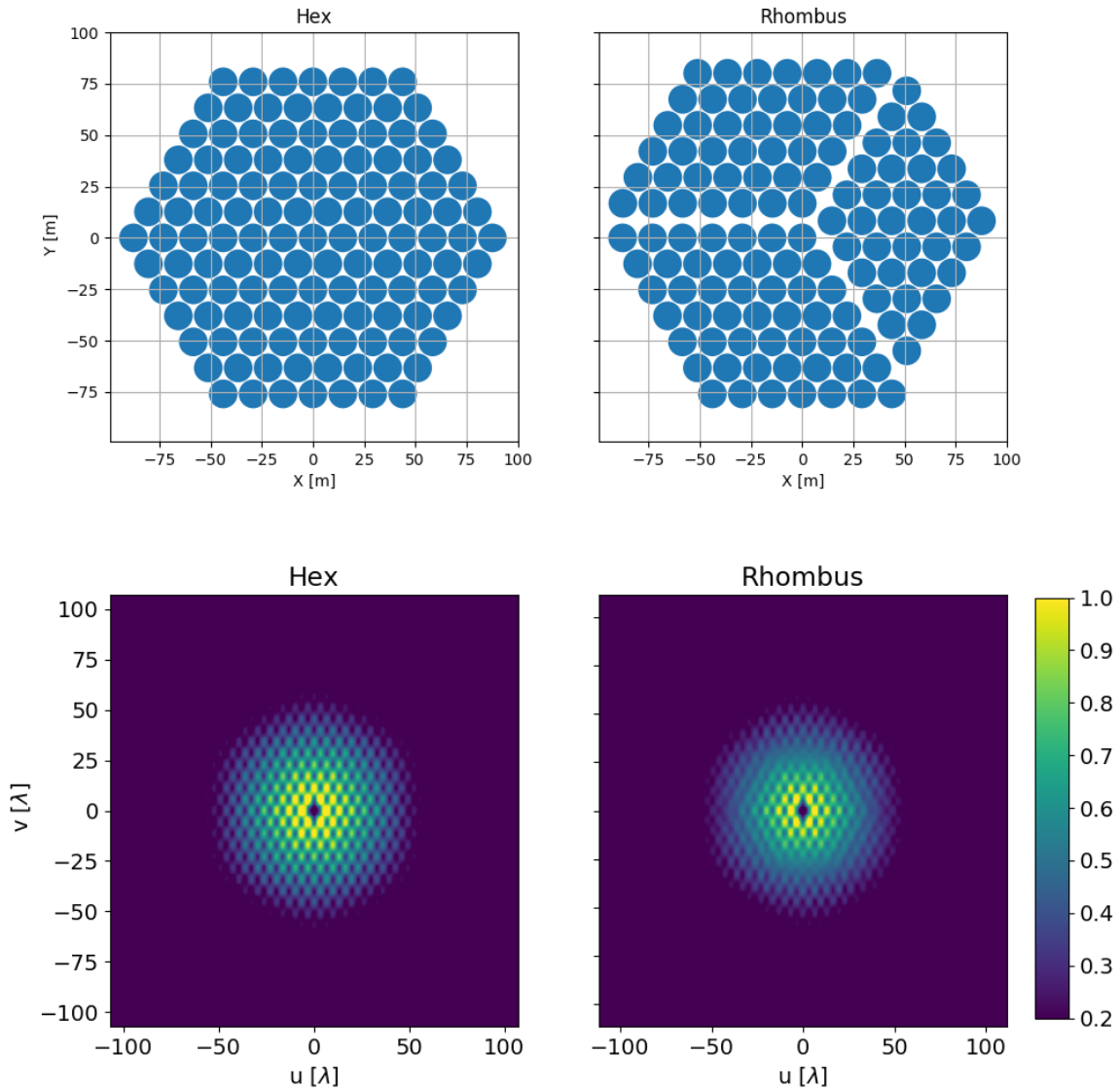
Figure 31: The gridded (u, v) weights for the Hex and Rhombus arrays at 150 MHz. Both arrays have a response in the (u, v) plane which sharply peaked at the shortest spacing between antennas ($|u|$ 7λ). The Rhombus array appears slightly more smooth near $|u| = 25$ λ by eye, but this does not provided a full evaluation of foreground leakage.
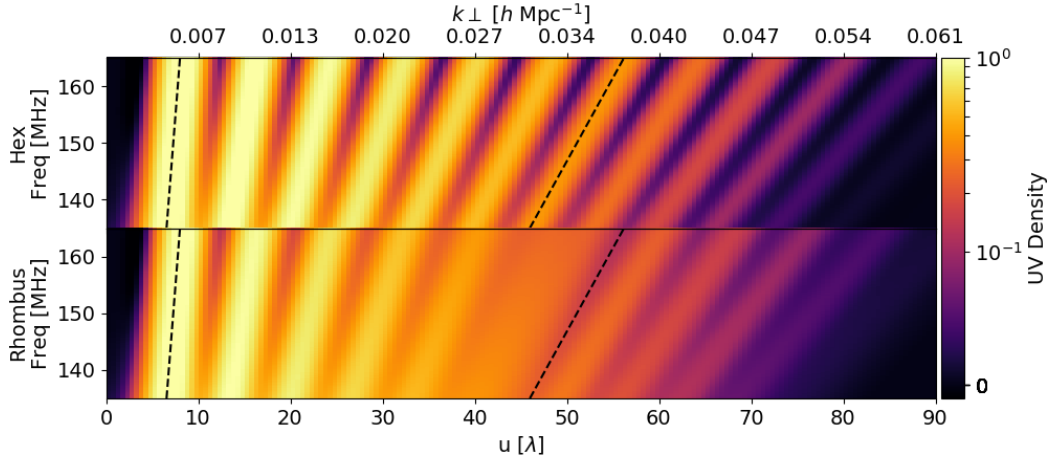
Figure 32: The gridded (u, v) weights from Figure 31 for the Hex and Rhombus arrays along a cut at $v = 0$ plotted as a function of frequency and u. Over plotted in dashed black lines are two baselines (7.3λ and 51.1λ at 150 MHz respectively). The shorter baseline appears almost identical between to the two arrays, however the longer baselines (where the wedge would be more prominent) appears significantly smoother for the Rhombus array.

sidelobe of the gridded kernel. Beyond the size scale of the pixel, no information about the beam could be accurately reconstructed.

The ability to grid and add baselines coherently is the core foundation of this evaluation[19]. The gridded weights for both arrays at 150 MHz are shown in Figure 31. Both arrays display sharp peaks at the smallest baseline length and a gradual decreas in response towards longer baselines. After gridding the (u, v) weights over the 30 MHz bandwidth for both simulated arrays, the spectral evolution can be evaluated. The evolution of the weights for both arrays along the $v = 0$ axis in the (u, v) plane is plotted in Figure 32. The noticeably smoother density of the Rhombus array near $u \sim 50\lambda$ gives a visual clue that this array has a flatter, and therefor less chromatic

[19] This is accomplished using the PY21CMWEDGE python package found at github.com/mkolopanis/py21cmwedge

106
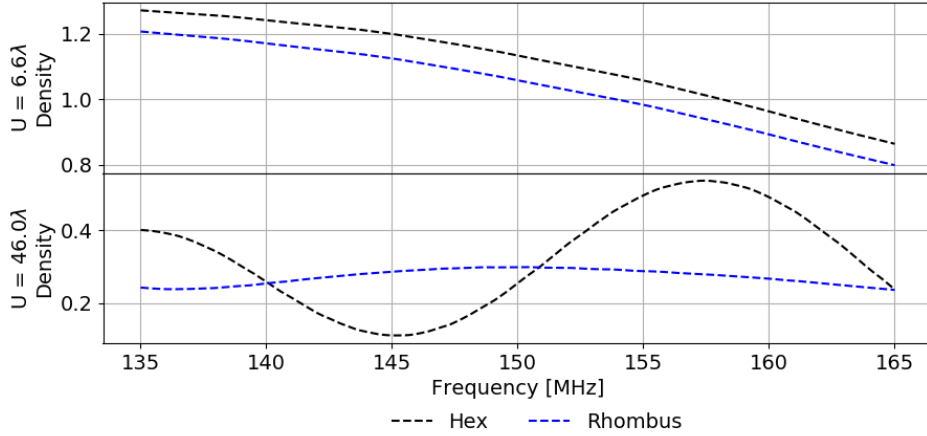
Figure 33: The one dimensional cut of the $(u.v)$ density from Figure 32 plotted against frequency. The shorter baseline length is nearly identical between the two arrays. For the longer baseline length, the Rhombus array displays a similar amplitude with lower variance over the bandwidth in the simulation.

response. A 1-Dimensional slice of the weights along $u = 6.6\lambda$ and $u = 46.0\lambda$ for each arrays is displayed in Figure 33. This further illustrates the reduced variation in density exhibited by the Rhombus array compared to the Hex. The two wavelengths $u = 6.6\lambda$ and $u = 46.0\lambda$, correspond to cosmological scales $k_\perp = 0.0044\ h\ \mathrm{Mpc}^{-1}$ and $k_\perp = 0.0310\ h\ \mathrm{Mpc}^{-1}$ respectively. Comparing the fractional power from Figure 29, both arrays have similar leakage at the shorter baseline where the (u, v) density is similar, but the Rhombus has reduced foreground leakage at the longer baseline where the density is smoother.

This qualitative assessment comparing the general shapes helps to create an intuitive understanding of how the baseline sampling affects wedge contamination. To perform a quantitative comparison, the (u, v, f) weights are Fourier transformed along the frequency axis to compute the point spread function (PSF) in power spectrum space. This is equivalent to the power spectrum of a single 1 Jy point source observed
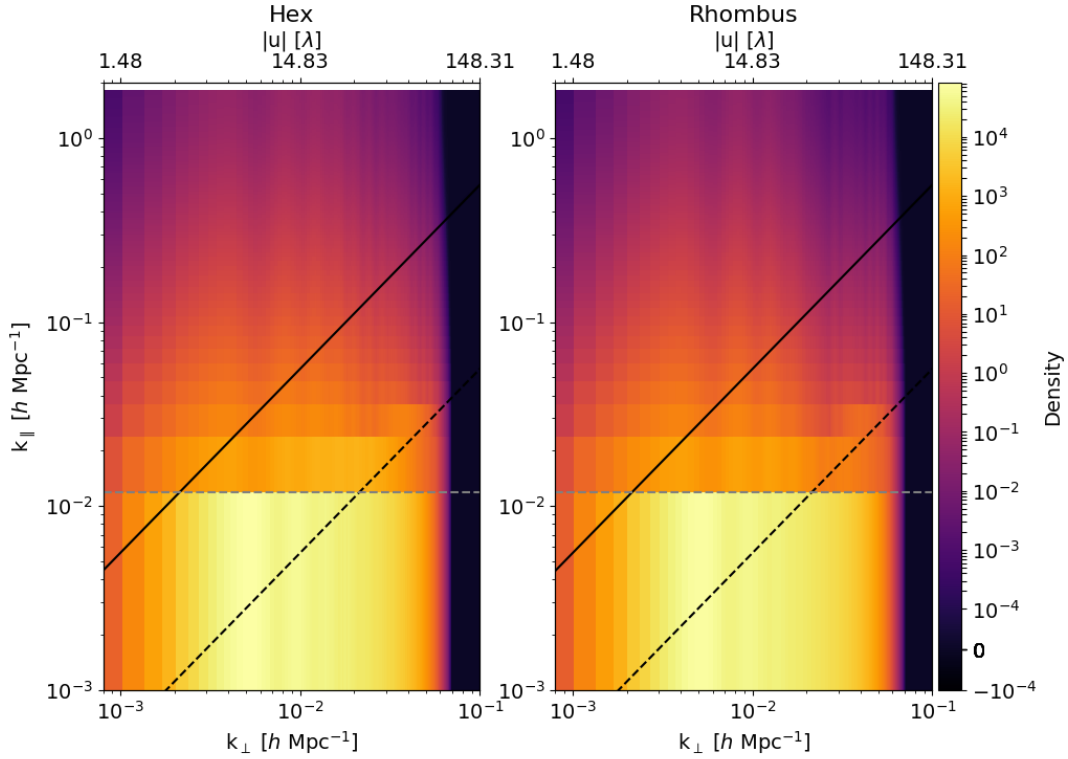
Figure 34: The 2-Dimensional point spread function (PSF) in power spectrum space for each simulated array. This is the Frequency Fast Fourier Transform (FFT) of the (u, v) weights from Figure 31. This is equivalent to the power spectrum of a single point source located at the zenith but quicker to calculate than using a full simulation pipeline. All additional lines are the same as Figure 28. Vertical striations correspond to areas where fluctuations in the (u, v) weights occur. By eye, it is difficult to tell the difference is response between the two instruments.

at zenith but was a much simpler calculation than using a simulation pipeline. The PSFs for both arrays is shown in Figure 34. Like the complete simulations above, the difference between the two is difficult to perceive by eye.

Similar to the evaluation of wedge leakage in Section 4.3.1, the ratio of the total weights inside the $k_\parallel = 0$ bin and the weights outside the $k_\parallel = 0$ bin of the simulated
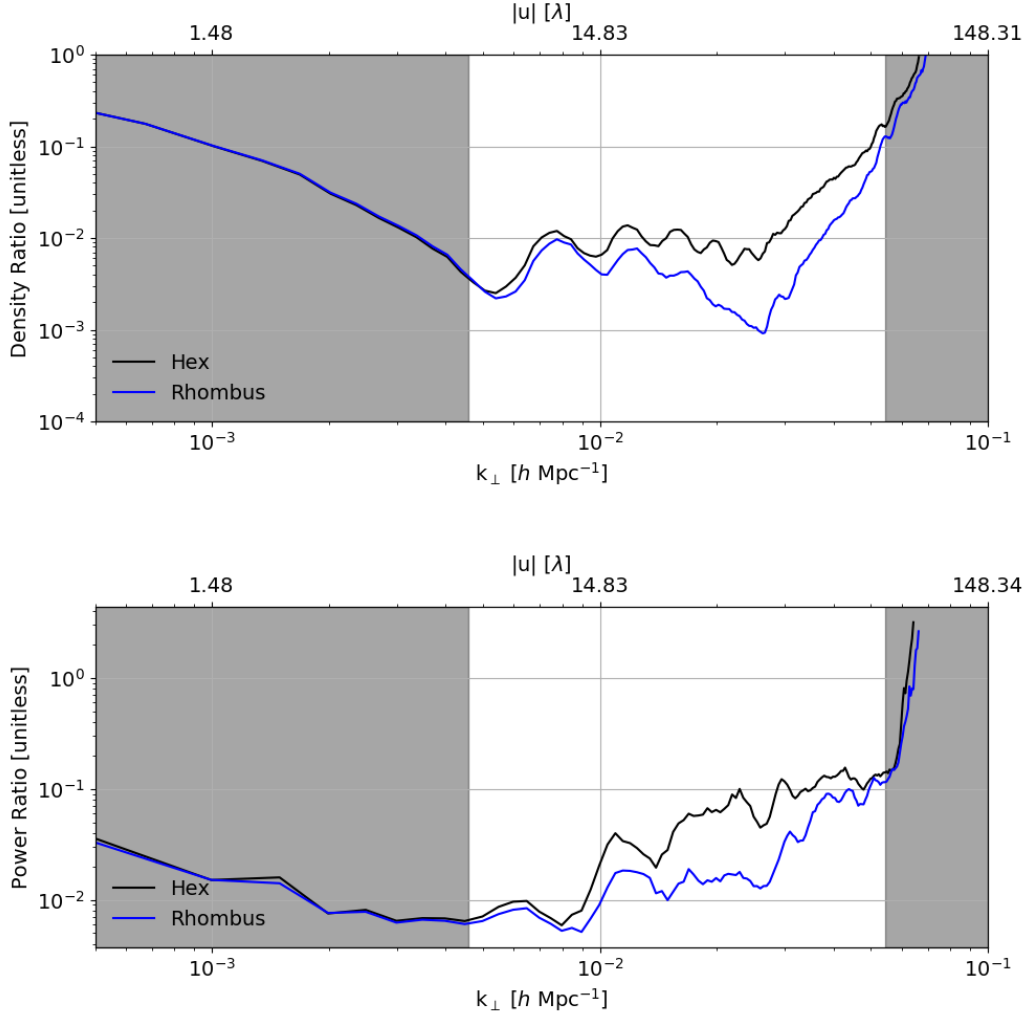
Figure 35: **TOP:** The ratio of total density above and below the bandwidth limited region of the two simulated power spectra in Figure 34.
Bottom: The power ratio plot from Figure 29.
In Both: The region with high agreement between the two arrays ($k_\perp < 0.005h$ Mpc^{-1}) also coincides with the Fourier modes which are not probed by either instruments. The shortest baseline for each array (7.3λ) and as such the arrays are only sensitive to cosmological scales above $k_\perp = 0.005h$ Mpc^{-1}. The Rhombus array shows noticeably less total density outside the bandwidth limited region in the range $0.005 < k_\perp < 0.04 \ h$ Mpc^{-1}. These scales are also expected to have larger wedge contamination. The sharp rise in fractional density near $k_\perp = 0.06 \ h$ Mpc^{-1} occurs where both arrays are no longer sensitive to sky modes (the region bounded by the maximum baseline length). The similarity of the weight and power ratios provides evidence to validate this evaluation as a proxy to determine an array's susceptibility to wedge leakage. As before in Figure 29, the grayed out regions indicate cosmological scales which cannot be probed by the arrays.

109

observation for each $k_\perp$-bin can be used to evaluate the fractional response of the power spectrum to information inside the wedge which should be confined to the bandwidth limited bin. This ratio, along with a repeat of the wedge leakage ratio from Figure 29, is shown in Figure 35. Below $k < 0.005h$ Mpc^{-1}, neither array is sensitive to cosmological signal, this is below the scales probed by the shortest baseline length ($u = 7.3\lambda$ at 150 MHz). Both ratios exhibit similar behavior when comparing their response as a function of $k_\perp$. The Rhombus array has less fractional density than the Hex above $k = 0.01h$ Mpc^{-1} until the region bounded by the longest baseline length (near $k = 0.06h$ Mpc^{-1}). The similarity between the responses of both the weight and density ratios indicate the smoother (u, v) coverage of the Rhombus arrays is less prone to foreground contamination. This supports the use of this proxy to evaluate future array configurations for their relative power spectrum sensitivity.

The other advantage to this computation is the reduction in complexity and calculation time. By only considering the (u, v, f) weights, this computation only requires 1 data channel (opposed to the 6 or 10 data channels in simulations without or with calibration against sky model respectively).

Similar to the method from Section 4.3.1, the total time required to evaluate this proxy can be modeled by considering the total number of computations performed. This method requires gridding a weight for each baseline, time, and frequency in kernel computed from the size of the dish. Then a single FFT convolution with the beam response in the (u, v) plane for each frequency. This can be modeled as

$$t_{weights} = \frac{N_{ants}^2 * N_{times} * N_{freqs} * N_{kernel}^2 + N_{freqs} * N_{pix}^2 * log(N_{pix})}{v_{ops}} \qquad (4.5)$$

where $N_{pix} = 400$ is length of one side of the (u, v) grid, $N_{kernel} = 7$ is the dish size in wavelengths and all other values are the same as before. Like the times for both PRISIM and FHD, this requires a calculation scaling with the number of baselines time

is saved in the number of calculations done by convolving the all weights with the beam at once. This saves time compared to PRISIM since there are no sources to scale computation time, and FHD since the beam is applied once to every weight with the FFT instead of gridding the weights with the beam directly.

4.4   Discussion

The two metrics defined above to estimate foreground leakage in radio interferometers have provided reasonable result for the array configurations analyzed. The similarity of the two metrics is promising, but the continued use of the proxy weight evaluation requires additional simulations for a full and accurate calibration and validation.

An initial correlation comparison between both statistics investigated in this work is plotted in Figure 36. The two statistics appear by eye to have a strong correlation, and to investigate this further I compute the Pearson correlation coefficient between the two and estimate the uncertainty by performing a bootstrap resampling to evaluate the underyling distribution of the correlation coefficient (Efron and Tibshirani, 1994) for both the Hex and Rhombus configurations.

The correlation coefficients are given in Table 6. The correlations coefficients indicate the two statistics are strongly correlated with p-values which support the rejection of the null-hypothesis. This provides strong evidence to continue investigating these metrics as a proxy to foreground contamination in interferometric arrays.

Simulations with different configurations of the compact Hex with varying amounts of redundancy and unique baseline types are planned to produce more comparisons
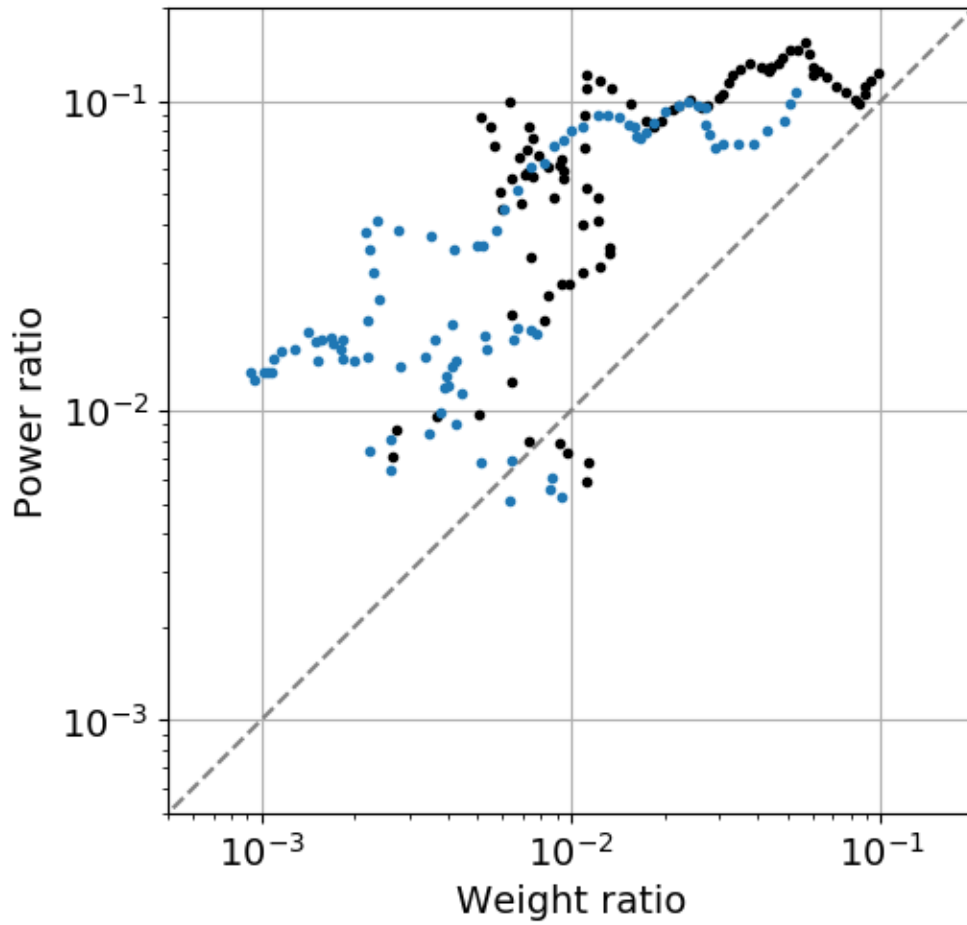
Figure 36: The correlation of the Power and Weight ratio statistics investigated in this work. By eye, the two statistics appear correlated. This correlations is investigated further by computing the Pearson correlation coefficient between for both array configurations.

Table 6: Power and Weight ratio correlation

Array	Pearson Correlation Coefficient	Uncertainty	P-value
Hex	0.79	0.07	3.7×10^{-4}
Rhombus	0.70	0.08	2.2×10^{-3}

Correlation coefficients of the power and weight statistics for the Hex and Rhombus array configurations analyzed in this work. The uncertainty is calculated as the standard deviation of the bootstrap resampling for both statistics. The corresponding p-values provide evidence to reject the null-hypothesis.

between the two metrics presented in this work. These arrays will include further breaking the hex sub-structures into triangles or adding pseudo-random variations in antenna placement to increase the number of unique baselines.

This analysis also produces questions concerning the trade off between increased redundancy and unique baseline types present in an array. These two parameters can effect the thermal sensitivity, foreground contamination, and efficiency of baseline usage towards producing a foreground free equivalent of a given array design.

This analysis will be continued for multiple array configurations like those described above and include a trade-off analysis between the foreground contamination, baseline usage efficiency, and sensitivity in future works. The combination of these analysis will help create the array evaluation tool to help design the future foreground free array.

Chapter 5

CONCLUSION

This work has presented analysis methods and techniques for probing cosmig structure originating over a large volume of space-time. The use of the CMB as a back-light for Faraday Rotation will provide information on the evolution of cosmic magnetic fields and the new correlation method from this will work will help identify FR in CMB survey for further analysis.

Next generation CMB surveys, like the CMB-S4, will enable high precision polarization observations with low thermal noise. These kinds of observations will be able to place precise constraints on the total amount of FR of CMB photons. Using cross-correlation techniques like the one outlined here will help identify different contributions to FR. Until these thermal levels are reached, cross correlations will enable earlier detections than available through auto-correlations or power spectrum estimators of single maps.

The study of the cosmic dawn and Epoch of Reionization in this work produced revised limits on the 21cm power spectrum of the EoR from the 64 element deployment of PAPER. By tracing data with different foreground filtering techniques, it was possible to provide comparable limits in multiple redshift ranges. This is accomplished by selecting the foreground filtering technique better equipped to mitigate foregrounds in each redshift.

The lessons learned in observation strategy, data analysis and power spectrum estimation from PAPER are influencing the future of HERA, the natural successor to paper. With its compact hexagonal design, HERA will build upon the success

of redundant array design for high sensitivity in future 21cm observations. The construction of outrigger dishes in later deployments will enable imaging analyses to complement and validate the delay-based analysis based on the PAPER pipeline.

The last chapter of this work outlines a method to evaluate potential foreground leakage in upcoming radio interferometers. By constructing the power spectrum of the (u, v) weights, an estimate of the expected foreground leakage can be compared for different array designs. This calculation is quicker than full-sky end to end instrument simulations but can provide comparable information on foreground leakage. Using this evaluation, array designs can be iterated on to optimize a future imaging array.

Constructing an array free of foreground contamination in the wedge would enable science observations and cosmological constraints in both statistical and imaging modes. Such an advance is necessary as 21 cm cosmology moves from early experimental arrays into the regime of precision cosmology. To best reduce foreground leakage, an optimized array would require uniform (u, v, f) weights along the spectral dimension for all observed cosmological scales.

A next generation array, with suitably optimized (u, v) response should aim to mitigate foreground leakage below the desired level for HI mapping. Complete 3-Dimensional cubes of neutral Hydrogen would not only allow for detection of the power spectrum of reionization but map the entire history in our Universe. Identifying early ionized bubbles can help constrain the type of luminous bodies responsible for the EoR and direct follow up surveys for detailed studies of these bodies. Cross correlations of the evolution of ionized bubbles with other cosmic probes like the CMB would help constrain the cosmological parameters which describe the Universe and how we perceive it.

REFERENCES

Ade, P. A. R., K. Arnold, M. Atlas, C. Baccigalupi, D. Barron, D. Boettger, J. Borrill, S. Chapman, Y. Chinone, A. Cukierman, M. Dobbs, A. Ducout, R. Dunner, T. Elleflot, J. Errard, G. Fabbian, S. Feeney, C. Feng, A. Gilbert, N. Goeckner-Wald, J. Groh, G. Hall, N. W. Halverson, M. Hasegawa, K. Hattori, M. Hazumi, C. Hill, W. L. Holzapfel, Y. Hori, L. Howe, Y. Inoue, G. C. Jaehnig, A. H. Jaffe, O. Jeong, N. Katayama, J. P. Kaufman, B. Keating, Z. Kermish, R. Keskitalo, T. Kisner, A. Kusaka, M. Le Jeune, A. T. Lee, E. M. Leitch, D. Leon, Y. Li, E. Linder, L. Lowry, F. Matsuda, T. Matsumura, N. Miller, J. Montgomery, M. J. Myers, M. Navaroli, H. Nishino, T. Okamura, H. Paar, J. Peloton, L. Pogosian, D. Poletti, G. Puglisi, C. Raum, G. Rebeiz, C. L. Reichardt, P. L. Richards, C. Ross, K. M. Rotermund, D. E. Schenck, B. D. Sherwin, M. Shimon, I. Shirley, P. Siritanasak, G. Smecher, N. Stebor, B. Steinbach, A. Suzuki, J.-i. Suzuki, O. Tajima, S. Takakura, A. Tikhomirov, T. Tomaru, N. Whitehorn, B. Wilson, A. Yadav, A. Zahn, O. Zahn and Polarbear Collaboration, "POLARBEAR constraints on cosmic birefringence and primordial magnetic fields", PRD **92**, 12, 123509 (2015).

Ahmed, Z., M. Amiri, S. J. Benton, J. J. Bock, R. Bowens-Rubin, I. Buder, E. Bullock, J. Connors, J. P. Filippini, J. A. Grayson, M. Halpern, G. C. Hilton, V. V. Hristov, H. Hui, K. D. Irwin, J. Kang, K. S. Karkare, E. Karpel, J. M. Kovac, C. L. Kuo, C. B. Netterfield, H. T. Nguyen, R. O'Brient, R. W. Ogburn, C. Pryke, C. D. Reintsema, S. Richter, K. L. Thompson, A. D. Turner, A. G. Vieregg, W. L. K. Wu and K. W. Yoon, "BICEP3: a 95GHz refracting telescope for degree-scale CMB polarization", in "Millimeter, Submillimeter, and Far-Infrared Detectors and Instrumentation for Astronomy VII", vol. 9153 of *Proc. SPIE*, p. 91531N (2014).

Ali, S. S., S. Bharadwaj and J. N. Chengalur, "Foregrounds for redshifted 21-cm studies of reionization: Giant Meter Wave Radio Telescope 153-MHz observations", MNRAS**385**, 2166–2174 (2008).

Ali, Z. S., A. R. Parsons, H. Zheng, J. C. Pober, A. Liu, J. E. Aguirre, R. F. Bradley, G. Bernardi, C. L. Carilli, C. Cheng, D. R. DeBoer, M. R. Dexter, J. Grobbelaar, J. Horrell, D. C. Jacobs, P. Klima, D. H. E. MacMahon, M. Maree, D. F. Moore, N. Razavi, I. I. Stefan, W. P. Walbrugh and A. Walker, "PAPER-64 Constraints on Reionization: The 21 cm Power Spectrum at z = 8.4", ApJ**809**, 61 (2015).

Andrae, R., "Error estimation in astronomy: A guide", ArXiv e-prints (2010).

Astropy Collaboration, T. P. Robitaille, E. J. Tollerud *et al.*, "Astropy: A community Python package for astronomy", aap **558**, A33 (2013).

Barkana, R., "On correlated random walks and 21-cm fluctuations during cosmic reionization", MNRAS**376**, 1784–1792 (2007).

Barkana, R., "Studying the sources of cosmic reionization with 21-cm fluctuations", MNRAS**397**, 1454–1463 (2009).

Barkana, R. and A. Loeb, "In the beginning: the first sources of light and the reionization of the universe", Phys. Rep.**349**, 125–238 (2001).

Barkana, R. and A. Loeb, "The physics and early history of the intergalactic medium", Reports on Progress in Physics **70**, 627–657 (2007).

Barry, N., B. Hazelton, I. Sullivan, M. F. Morales and J. C. Pober, "Calibration requirements for detecting the 21 cm epoch of reionization power spectrum and implications for the SKA", MNRAS**461**, 3135–3144 (2016).

Beardsley, A., *The Murchison Widefield Array 21cm Epoch of Reionization Experiment: Design, Construction, and First Season Results*, Ph.D. thesis, University of Washington (2015).

Beardsley, A. P., B. J. Hazelton, I. S. Sullivan, P. Carroll, N. Barry, M. Rahimi, B. Pindor, C. M. Trott, J. Line, D. C. Jacobs, M. F. Morales, J. C. Pober, G. Bernardi, J. D. Bowman, M. P. Busch, F. Briggs, R. J. Cappallo, B. E. Corey, A. de Oliveira-Costa, J. S. Dillon, D. Emrich, A. Ewall-Wice, L. Feng, B. M. Gaensler, R. Goeke, L. J. Greenhill, J. N. Hewitt, N. Hurley-Walker, M. Johnston-Hollitt, D. L. Kaplan, J. C. Kasper, H. S. Kim, E. Kratzenberg, E. Lenc, A. Loeb, C. J. Lonsdale, M. J. Lynch, B. McKinley, S. R. McWhirter, D. A. Mitchell, E. Morgan, A. R. Neben, N. Thyagarajan, D. Oberoi, A. R. Offringa, S. M. Ord, S. Paul, T. Prabu, P. Procopio, J. Riding, A. E. E. Rogers, A. Roshi, N. Udaya Shankar, S. K. Sethi, K. S. Srivani, R. Subrahmanyan, M. Tegmark, S. J. Tingay, M. Waterson, R. B. Wayth, R. L. Webster, A. R. Whitney, A. Williams, C. L. Williams, C. Wu and J. S. B. Wyithe, "First Season MWA EoR Power Spectrum Results at Redshift 7", ArXiv e-prints (2016).

Becker, R. H., X. Fan, R. L. White, M. A. Strauss, V. K. Narayanan, R. H. Lupton, J. E. Gunn, J. Annis, N. A. Bahcall, J. Brinkmann, A. J. Connolly, I. Csabai, P. C. Czarapata, M. Doi, T. M. Heckman, G. S. Hennessy, Ž. Ivezić, G. R. Knapp, D. Q. Lamb, T. A. McKay, J. A. Munn, T. Nash, R. Nichol, J. R. Pier, G. T. Richards, D. P. Schneider, C. Stoughton, A. S. Szalay, A. R. Thakar and D. G. York, "Evidence for Reionization at z~6: Detection of a Gunn-Peterson Trough in a z=6.28 Quasar", AJ**122**, 2850–2857 (2001).

Bennett, C. L., D. Larson, J. L. Weiland, N. Jarosik, G. Hinshaw, N. Odegard, K. M. Smith, R. S. Hill, B. Gold, M. Halpern, E. Komatsu, M. R. Nolta, L. Page, D. N. Spergel, E. Wollack, J. Dunkley, A. Kogut, M. Limon, S. S. Meyer, G. S. Tucker and E. L. Wright, "Nine-year Wilkinson Microwave Anisotropy Probe (WMAP) Observations: Final Maps and Results", ApJS**208**, 20 (2013).

Benoit, A. *et al.*, "The Cosmic microwave background anisotropy power spectrum measured by Archeops", Astron. Astrophys. **399**, L19–L23 (2003).

Benson, B. A., P. A. R. Ade, Z. Ahmed, S. W. Allen, K. Arnold, J. E. Austermann, A. N. Bender, L. E. Bleem, J. E. Carlstrom, C. L. Chang, H. M. Cho, J. F. Cliche, T. M. Crawford, A. Cukierman, T. de Haan, M. A. Dobbs, D. Dutcher, W. Everett, A. Gilbert, N. W. Halverson, D. Hanson, N. L. Harrington, K. Hattori, J. W. Henning, G. C. Hilton, G. P. Holder, W. L. Holzapfel, K. D. Irwin, R. Keisler, L. Knox, D. Kubik, C. L. Kuo, A. T. Lee, E. M. Leitch, D. Li, M. McDonald, S. S. Meyer, J. Montgomery, M. Myers, T. Natoli, H. Nguyen, V. Novosad, S. Padin, Z. Pan, J. Pearson, C. Reichardt, J. E. Ruhl, B. R. Saliwanchik, G. Simard, G. Smecher, J. T. Sayre, E. Shirokoff, A. A. Stark, K. Story, A. Suzuki, K. L. Thompson, C. Tucker, K. Vanderlinde, J. D. Vieira, A. Vikhlinin, G. Wang, V. Yefremenko and K. W. Yoon, "SPT-3G: a next-generation cosmic microwave background polarization experiment on the South Pole telescope", in "Millimeter, Submillimeter, and Far-Infrared Detectors and Instrumentation for Astronomy VII", vol. 9153 of *Proc. SPIE*, p. 91531P (2014).

Bernardi, G., A. G. de Bruyn, M. A. Brentjens, B. Ciardi, G. Harker, V. Jelić, L. V. E. Koopmans, P. Labropoulos, A. Offringa, V. N. Pandey, J. Schaye, R. M. Thomas, S. Yatawatta and S. Zaroubi, "Foregrounds for observations of the cosmological 21 cm line. I. First Westerbork measurements of Galactic emission at 150 MHz in a low latitude field", A&A**500**, 965–979 (2009).

Bernardi, G., A. G. de Bruyn, G. Harker, M. A. Brentjens, B. Ciardi, V. Jelić, L. V. E. Koopmans, P. Labropoulos, A. Offringa, V. N. Pandey, J. Schaye, R. M. Thomas, S. tawatta and S. Zaroubi, "Foregrounds for observations of the cosmological 21 cm line. II. Westerbork observations of the fields around 3C 196 and the North Celestial Pole", A&A**522**, A67+ (2010).

Bernardi, G., L. J. Greenhill, D. A. Mitchell, S. M. Ord, B. J. Hazelton, B. M. Gaensler, A. de Oliveira-Costa, M. F. Morales, N. Udaya Shankar, R. Subrahmanyan, R. B. Wayth, E. Lenc, C. L. Williams, W. Arcus, B. S. Arora, D. G. Barnes, J. D. Bowman, F. H. Briggs, J. D. Bunton, R. J. Cappallo, B. E. Corey, A. Deshpande, L. deSouza, D. Emrich, R. Goeke, D. Herne, J. N. Hewitt, M. Johnston-Hollitt, D. Kaplan, J. C. Kasper, B. B. Kincaid, R. Koenig, E. Kratzenberg, C. J. Lonsdale, M. J. Lynch, S. R. McWhirter, E. Morgan, D. Oberoi, J. Pathikulangara, T. Prabu, R. A. Remillard, A. E. E. Rogers, A. Roshi, J. E. Salah, R. J. Sault, K. S. Srivani, J. Stevens, S. J. Tingay, M. Waterson, R. L. Webster, A. R. Whitney, A. Williams and J. S. B. Wyithe, "A 189 MHz, 2400 deg^2 Polarization Survey with the Murchison Widefield Array 32-element Prototype", ApJ**771**, 105 (2013).

Bernardi, G., J. T. L. Zwart, D. Price, L. J. Greenhill, A. Mesinger, J. Dowell, T. Eftekhari, S. W. Ellingson, J. Kocz and F. Schinzel, "Bayesian constraints on the global 21-cm signal from the Cosmic Dawn", MNRAS**461**, 2847–2855 (2016).

BICEP2 and Keck Array Collaborations, P. A. R. Ade, Z. Ahmed, R. W. Aikin, K. D. Alexander, D. Barkats, S. J. Benton, C. A. Bischoff, J. J. Bock, J. A. Brevik, I. Buder, E. Bullock, V. Buza, J. Connors, B. P. Crill, C. D. Dowell, C. Dvorkin, L. Duband, J. P. Filippini, S. Fliescher, S. R. Golwala, M. Halpern, S. Harrison, M. Hasselfield, S. R. Hildebrandt, G. C. Hilton, V. V. Hristov, H. Hui, K. D. Irwin, K. S. Karkare, J. P. Kaufman, B. G. Keating, S. Kefeli, S. A. Kernasovskiy, J. M. Kovac, C. L. Kuo, E. M. Leitch, M. Lueker, P. Mason, K. G. Megerian, C. B. Netterfield, H. T. Nguyen, R. O'Brient, R. W. Ogburn, IV, A. Orlando, C. Pryke, C. D. Reintsema, S. Richter, R. Schwarz, C. D. Sheehy, Z. K. Staniszewski, R. V. Sudiwala, G. P. Teply, K. L. Thompson, J. E. Tolan, A. D. Turner, A. G. Vieregg, A. C. Weber, J. Willmert, C. L. Wong and K. W. Yoon, "BICEP2/Keck Array V: Measurements of B-mode Polarization at Degree Angular Scales and 150 GHz by the Keck Array", ApJ**811**, 126 (2015).

BICEP2/Keck and Planck Collaborations, P. A. R. Ade, N. Aghanim, Z. Ahmed, R. W. Aikin, K. D. Alexander, M. Arnaud, J. Aumont, C. Baccigalupi, A. J. Banday and et al., "Joint Analysis of BICEP2/Keck Array and Planck Data", Physical Review Letters **114**, 10, 101301 (2015).

Bischoff, C., A. Brizius, I. Buder, Y. Chinone, K. Cleary, R. N. Dumoulin, A. Kusaka, R. Monsalve, S. K. Næss, L. B. Newburgh, G. Nixon, R. Reeves, K. M. Smith, K. Vanderlinde, I. K. Wehus, M. Bogdan, R. Bustos, S. E. Church, R. Davis, C. Dickinson, H. K. Eriksen, T. Gaier, J. O. Gundersen, M. Hasegawa, M. Hazumi, C. Holler, K. M. Huffenberger, W. A. Imbriale, K. Ishidoshiro, M. E. Jones, P. Kangaslahti, D. J. Kapner, C. R. Lawrence, E. M. Leitch, M. Limon, J. J. McMahon, A. D. Miller, M. Nagai, H. Nguyen, T. J. Pearson, L. Piccirillo, S. J. E. Radford, A. C. S. Readhead, J. L. Richards, D. Samtleben, M. Seiffert, M. C. Shepherd, S. T. Staggs, O. Tajima, K. L. Thompson, R. Williamson, B. Winstein, E. J. Wollack and J. T. L. Zwart, "The Q/U Imaging ExperimenT Instrument", ApJ**768**, 9 (2013).

Blanchard, A. and J. Schneider, "Gravitational lensing effect on the fluctuations of the cosmic background radiation", A&A**184**, 1–6 (1987).

Bond, J. R. and S. T. Myers, "The Peak-Patch Picture of Cosmic Catalogs. I. Algorithms", ApJS**103**, 1 (1996a).

Bond, J. R. and S. T. Myers, "The Peak-Patch Picture of Cosmic Catalogs. II. Validation", ApJS**103**, 41 (1996b).

Bond, J. R. and S. T. Myers, "The Peak-Patch Picture of Cosmic Catalogs. III. Application to Clusters", ApJS**103**, 63 (1996c).

Bowman, J. D., I. Cairns, D. L. Kaplan, T. Murphy, D. Oberoi, L. Staveley-Smith, W. Arcus, D. G. Barnes, G. Bernardi, F. H. Briggs, S. Brown, J. D. Bunton, A. J. Burgasser, R. J. Cappallo, S. Chatterjee, B. E. Corey, A. Coster, A. Deshpande, L. deSouza, D. Emrich, P. Erickson, R. F. Goeke, B. M. Gaensler, L. J. Greenhill, L. Harvey-Smith, B. J. Hazelton, D. Herne, J. N. Hewitt, M. Johnston-Hollitt, J. C. Kasper, B. B. Kincaid, R. Koenig, E. Kratzenberg, C. J. Lonsdale, M. J. Lynch, L. D. Matthews, S. R. McWhirter, D. A. Mitchell, M. F. Morales, E. H. Morgan, S. M. Ord, J. Pathikulangara, T. Prabu, R. A. Remillard, T. Robishaw, A. E. E. Rogers, A. A. Roshi, J. E. Salah, R. J. Sault, N. U. Shankar, K. S. Srivani, J. B. Stevens, R. Subrahmanyan, S. J. Tingay, R. B. Wayth, M. Waterson, R. L. Webster, A. R. Whitney, A. J. Williams, C. L. Williams and J. S. B. Wyithe, "Science with the Murchison Widefield Array", PASA **30**, 31 (2013).

Bowman, J. D., M. F. Morales and J. N. Hewitt, "Foreground Contamination in Interferometric Measurements of the Redshifted 21 cm Power Spectrum", ApJ**695**, 183–199 (2009).

Bowman, J. D. and A. E. E. Rogers, "A lower limit of $\Delta z > 0.06$ for the duration of the reionization epoch", Nature**468**, 796–798 (2010).

Bowman, J. D., A. E. E. Rogers, R. A. Monsalve, T. J. Mozdzen and N. Mahesh, "An absorption profile centred at 78 megahertz in the sky-averaged spectrum", Nature **555**, 67, URL http://dx.doi.org/10.1038/nature25792 (2018).

Bunn, E. F., M. Zaldarriaga, M. Tegmark and A. de Oliveira-Costa, "E/B decomposition of finite pixelized CMB maps", Phys. Rev. **D67**, 023501 (2003).

Calabrese, E. *et al.*, "Precision Epoch of Reionization studies with next-generation CMB experiments", JCAP **1408**, 010 (2014).

Carretti, E., "Galactic Foregrounds and CMB Polarization", in "The Dynamic Interstellar Medium: A Celebration of the Canadian Galactic Plane Survey", edited by R. Kothes, T. L. Landecker and A. G. Willis, vol. 438 of *Astronomical Society of the Pacific Conference Series*, p. 276 (2010).

Chang, C., "A stage-iv cmb experiment, cmb-s4", URL https://indico.fnal.gov/getFile.py/access?resId=0&materialId=slides&contribId=71&sessionId=10&subContId=6&confId=6890 (2013).

Chen, X. and M. Kamionkowski, "Particle decays during the cosmic dark ages", Phys. Rev. D **70**, 043502, URL http://link.aps.org/doi/10.1103/PhysRevD.70.043502 (2004).

Ciardi, B. and A. Ferrara, "The First Cosmic Structures and Their Effects", Space Sci. Rev.**116**, 625–705 (2005).

Clark, B. G., "Coherence in Radio Astronomy", in "Synthesis Imaging in Radio Astronomy II", edited by G. B. Taylor, C. L. Carilli, & R. A. Perley, vol. 180 of *Astronomical Society of the Pacific Conference Series*, pp. 1–+ (1999).

Condon, J., "An Analysis of the VLASS Proposal", ArXiv e-prints (2015).

Croft, R. A. C. and G. Altay, "Radiation-induced large-scale structure during the reionization epoch: the autocorrelation function", MNRAS**388**, 1501–1520 (2008).

Datta, A., J. D. Bowman and C. L. Carilli, "Bright Source Subtraction Requirements for Redshifted 21 cm Measurements", ApJ**724**, 526–538 (2010).

De, S., L. Pogosian and T. Vachaspati, "CMB Faraday rotation as seen through the Milky Way", Phys. Rev. D**88**, 6, 063527 (2013).

de Bernardis, P. *et al.*, "A Flat universe from high resolution maps of the cosmic microwave background radiation", Nature **404**, 955–959 (2000).

de Oliveira-Costa, A., M. Tegmark, B. M. Gaensler, J. Jonas, T. L. Landecker and P. Reich, "A model of diffuse Galactic radio emission from 10 MHz to 100 GHz", MNRAS**388**, 247–260 (2008).

DeBoer, D. R., A. R. Parsons, J. E. Aguirre, P. Alexander, Z. S. Ali, A. P. Beardsley, G. Bernardi, J. D. Bowman, R. F. Bradley, C. L. Carilli, C. Cheng, E. de Lera Acedo, J. S. Dillon, A. Ewall-Wice, G. Fadana, N. Fagnoni, R. Fritz, S. R. Furlanetto, B. Glendenning, B. Greig, J. Grobbelaar, B. J. Hazelton, J. N. Hewitt, J. Hickish, D. C. Jacobs, A. Julius, M. Kariseb, S. A. Kohn, T. Lekalake, A. Liu, A. Loots, D. MacMahon, L. Malan, C. Malgas, M. Maree, N. Mathison, E. Matsetela, A. Mesinger, M. F. Morales, A. R. Neben, N. Patra, S. Pieterse, J. C. Pober, N. Razavi-Ghods, J. Ringuette, J. Robnett, K. Rosie, R. Sell, C. Smith, A. Syce, M. Tegmark, N. Thyagarajan, P. K. G. Williams and H. Zheng, "Hydrogen Epoch of Reionization Array (HERA)", ArXiv e-prints (2016).

Dijkstra, M., "Constraining Reionization with Lyα Emitting Galaxies", **423**, 145 (2016).

Dijkstra, M., Z. Haiman, M. J. Rees and D. H. Weinberg, "Photoionization Feedback in Low-Mass Galaxies at High Redshift", ApJ**601**, 666–675 (2004).

Dillon, J. S., S. A. Kohn, A. R. Parsons, J. E. Aguirre, Z. S. Ali, G. Bernardi, N. S. Kern, W. Li, A. Liu, C. D. Nunhokee and J. C. Pober, "Polarized Redundant-Baseline Calibration for 21 cm Cosmology Without Adding Spectral Structure", ArXiv e-prints (2017).

Dillon, J. S., A. Liu and M. Tegmark, "A fast method for power spectrum and foreground analysis for 21 cm cosmology", Phys. Rev. D**87**, 4, 043005 (2013).

Dillon, J. S., A. Liu, C. L. Williams, J. N. Hewitt, M. Tegmark, E. H. Morgan, A. M. Levine, M. F. Morales, S. J. Tingay, G. Bernardi, J. D. Bowman, F. H. Briggs, R. C. Cappallo, D. Emrich, D. A. Mitchell, D. Oberoi, T. Prabu, R. Wayth and R. L. Webster, "Overcoming real-world obstacles in 21 cm power spectrum estimation: A method demonstration and results from early Murchison Widefield Array data", Phys. Rev. D**89**, 2, 023002 (2014).

Dillon, J. S., A. R. Neben, J. N. Hewitt, M. Tegmark, N. Barry, A. P. Beardsley, J. D. Bowman, F. Briggs, P. Carroll, A. de Oliveira-Costa, A. Ewall-Wice, L. Feng, L. J. Greenhill, B. J. Hazelton, L. Hernquist, N. Hurley-Walker, D. C. Jacobs, H. S. Kim, P. Kittiwisit, E. Lenc, J. Line, A. Loeb, B. McKinley, D. A. Mitchell, M. F. Morales, A. R. Offringa, S. Paul, B. Pindor, J. C. Pober, P. Procopio, J. Riding, S. Sethi, N. Udaya Shankar, R. Subrahmanyan, I. Sullivan, N. Thyagarajan, S. J. Tingay, C. Trott, R. B. Wayth, R. L. Webster, S. Wyithe, G. Bernardi, R. J. Cappallo, A. A. Deshpande, M. Johnston-Hollitt, D. L. Kaplan, C. J. Lonsdale, S. R. McWhirter, E. Morgan, D. Oberoi, S. M. Ord, T. Prabu, K. S. Srivani, A. Williams and C. L. Williams, "Empirical Covariance Modeling for 21 cm Power Spectrum Estimation: A Method Demonstration and New Limits from Early Murchison Widefield Array 128-Tile Data", Phys. Rev. D **91**, 12, 123011 (2015).

Dineen, P. and P. Coles, "Faraday rotation as a diagnostic of Galactic foreground contamination of cosmic microwave background maps", MNRAS**347**, 52–58 (2004).

Efron, B. and R. Tibshirani, *An Introduction to the Bootstrap*, Chapman & Hall/CRC Monographs on Statistics & Applied Probability (Taylor & Francis, 1994), URL https://books.google.com/books?id=gLlpIUxRntoC.

Essinger-Hileman, T., A. Ali, M. Amiri *et al.*, "CLASS: the cosmology large angular scale surveyor", in "Society of Photo-Optical Instrumentation Engineers (SPIE) Conference Series", vol. 9153 of *Society of Photo-Optical Instrumentation Engineers (SPIE) Conference Series*, p. 1 (2014).

Field, G. B., "Excitation of the hydrogen 21-cm line", Proceedings of the IRE **46**, 1, 240–250 (1958).

Fraisse, A. A., P. A. R. Ade, M. Amiri *et al.*, "SPIDER: probing the early Universe with a suborbital polarimeter", JCAP **4**, 47 (2013).

Furlanetto, S., M. Zaldarriaga and L. Hernquist, "Statistical probes of reionization with 21 cm tomography", Astrophys. J. **613**, 16–22 (2004a).

Furlanetto, S., M. Zaldarriaga and L. Hernquist, "The Growth of HII regions during reionization", Astrophys. J. **613**, 1–15 (2004b).

Furlanetto, S. R., S. P. Oh and F. H. Briggs, "Cosmology at low frequencies: The 21 cm transition and the high-redshift Universe", Phys. Rep.**433**, 181–301 (2006).

Ghosh, A., S. Bharadwaj, S. S. Ali and J. N. Chengalur, "Improved foreground removal in GMRT 610 MHz observations towards redshifted 21-cm tomography", MNRAS**418**, 2584–2589 (2011).

Ghosh, T., F. Boulanger, P. G. Martin, A. Bracco, F. Vansyngel, J. Aumont, J. J. Bock, O. Doré, U. Haud, P. M. W. Kalberla and P. Serra, "Modelling and simulation of large-scale polarized dust emission over the southern Galactic cap using the GASS Hi data", A&A**601**, A71 (2017).

Gilfanov, M., H.-J. Grimm and R. Sunyaev, "L_X-SFR relation in star-forming galaxies", MNRAS**347**, L57–L60 (2004).

Glover, S. C. O. and P. W. J. L. Brand, "Radiative feedback from an early X-ray background", MNRAS**340**, 210–226 (2003).

Gluscevic, V., M. Kamionkowski and A. Cooray, "Derotation of the cosmic microwave background polarization: Full-sky formalism", PRD **80**, 2, 023510 (2009).

Górski, K. M., E. Hivon, A. J. Banday, B. D. Wandelt, F. K. Hansen, M. Reinecke and M. Bartelmann, "HEALPix: A Framework for High-Resolution Discretization and Fast Analysis of Data Distributed on the Sphere", ApJ**622**, 759–771 (2005).

Greenhill, L. J. and G. Bernardi, "HI Epoch of Reionization Arrays", ArXiv e-prints: 1201.1700 (2012).

Greig, B., A. Mesinger and J. C. Pober, "Constraints on the temperature of the intergalactic medium at z = 8.4 with 21-cm observations", MNRAS**455**, 4295–4300 (2016).

Grimm, H.-J., M. Gilfanov and R. Sunyaev, "High-mass X-ray binaries as a star formation rate indicator in distant galaxies", MNRAS**339**, 793–809 (2003).

Gruppuso, A., G. Maggio, D. Molinari and P. Natoli, "A note on the birefringence angle estimation in CMB data analysis", J. Cosmology Astropart. Phys.**5**, 020 (2016).

Gunn, J. E. and B. A. Peterson, "On the Density of Neutral Hydrogen in Intergalactic Space.", ApJ**142**, 1633–1641 (1965).

Haiman, Z., "The First Nonlinear Structures and the Reionization History of the Universe", Coevolution of Black Holes and Galaxies p. 67 (2004).

Halverson, N. W. *et al.*, "DASI first results: A Measurement of the cosmic microwave background angular power spectrum", Astrophys. J. **568**, 38–45 (2002).

Hanany, S. *et al.*, "MAXIMA-1: A Measurement of the cosmic microwave background anisotropy on angular scales of 10 arcminutes to 5 degrees", Astrophys. J. **545**, L5 (2000).

Hanson, D., S. Hoover, A. Crites, P. A. R. Ade *et al.*, "Detection of B-Mode Polarization in the Cosmic Microwave Background with Data from the South Pole Telescope", Physical Review Letters **111**, 14, 141301 (2013).

Harari, D. D., J. D. Hayward and M. Zaldarriaga, "Depolarization of the cosmic microwave background by a primordial magnetic field and its effect upon temperature anisotropy", Phys. Rev. D**55**, 1841–1850 (1997).

Hazelton, B., A. Beardsley, J. Pober, D. Jacobs, Z. Ali, A. Ewall-Wice, P. L. Plante, aelanman, zacharymartinot, N. Kern and P. Williams, "Hera-team/pyuvdata: Version 1.2", URL https://doi.org/10.5281/zenodo.1044022 (2017).

Hazelton, B. J., M. F. Morales and I. S. Sullivan, "The Fundamental Multi-baseline Mode-mixing Foreground in 21 cm Epoch of Reionization Observations", ApJ**770**, 156 (2013).

Hivon, E., K. Gorski, C. Netterfield, B. Crill, S. Prunet *et al.*, "Master of the cosmic microwave background anisotropy power spectrum: a fast method for statistical analysis of large and complex cosmic microwave background data sets", Astrophys.J. **567**, 2 (2002).

Högbom, J. A., "Aperture Synthesis with a Non-Regular Distribution of Interferometer Baselines", A&AS**15**, 417–+ (1974).

Howlett, C., A. Lewis, A. Hall and A. Challinor, "CMB power spectrum parameter degeneracies in the era of precision cosmology", J. Cosmology Astropart. Phys.**4**, 027 (2012).

Hu, W., "Concepts in CMB anisotropy formation", Lect. Notes Phys. **470**, 207 (1996).

Hu, W., "Reionization Revisited: Secondary Cosmic Microwave Background Anisotropies and Polarization", apj **529**, 12–25 (2000).

Hu, W. and S. Dodelson, "Cosmic microwave background anisotropies", Ann. Rev. Astron. Astrophys. **40**, 171–216 (2002).

Hu, W. and N. Sugiyama, "Thermal history constraints on the isocurvature baryon model", ApJ**436**, 456–466 (1994).

Hu, W. and M. J. White, "A CMB polarization primer", New Astron. **2**, 323 (1997a).

Hu, W. and M. J. White, "The Damping tail of CMB anisotropies", Astrophys. J. **479**, 568 (1997b).

Iliev, I. T., G. Mellema, P. R. Shapiro and U.-L. Pen, "Self-regulated reionization", MNRAS**376**, 534–548 (2007).

J. E. Peebles, P., *Principles of Physical Cosmology*, Princeton Theories in Physics (Princeton University Press, 1993).

Jacobs, D. C., B. J. Hazelton, C. M. Trott, J. S. Dillon, B. Pindor, I. S. Sullivan, J. C. Pober, N. Barry, A. P. Beardsley, G. Bernardi, J. D. Bowman, F. Briggs, R. J. Cappallo, P. Carroll, B. E. Corey, A. de Oliveira-Costa, D. Emrich, A. Ewall-Wice, L. Feng, B. M. Gaensler, R. Goeke, L. J. Greenhill, J. N. Hewitt, N. Hurley-Walker, M. Johnston-Hollitt, D. L. Kaplan, J. C. Kasper, H. Kim, E. Kratzenberg, E. Lenc, J. Line, A. Loeb, C. J. Lonsdale, M. J. Lynch, B. McKinley, S. R. McWhirter, D. A. Mitchell, M. F. Morales, E. Morgan, A. R. Neben, N. Thyagarajan, D. Oberoi, A. R. Offringa, S. M. Ord, S. Paul, T. Prabu, P. Procopio, J. Riding, A. E. E. Rogers, A. Roshi, N. Udaya Shankar, S. K. Sethi, K. S. Srivani, R. Subrahmanyan, M. Tegmark, S. J. Tingay, M. Waterson, R. B. Wayth, R. L. Webster, A. R. Whitney, A. Williams, C. L. Williams, C. Wu and J. S. B. Wyithe, "The Murchison Widefield Array 21 cm Power Spectrum Analysis Methodology", ApJ**825**, 114 (2016).

Jacobs, D. C., A. R. Parsons, J. E. Aguirre, Z. Ali, J. Bowman, R. F. Bradley, C. L. Carilli, D. R. DeBoer, M. R. Dexter, N. E. Gugliucci, P. Klima, D. H. E. MacMahon, J. R. Manley, D. F. Moore, J. C. Pober, I. I. Stefan and W. P. Walbrugh, "A Flux Scale for Southern Hemisphere 21 cm Epoch of Reionization Experiments", ApJ**776**, 108 (2013).

Jacobs, D. C., J. C. Pober, A. R. Parsons, J. E. Aguirre, Z. S. Ali, J. Bowman, R. F. Bradley, C. L. Carilli, D. R. DeBoer, M. R. Dexter, N. E. Gugliucci, P. Klima, A. Liu, D. H. E. MacMahon, J. R. Manley, D. F. Moore, I. I. Stefan and W. P. Walbrugh, "Multiredshift Limits on the 21 cm Power Spectrum from PAPER", ApJ**801**, 51 (2015).

Jacobs, D. C. *et al.*, "Multi-redshift limits on the 21cm power spectrum from PAPER", Astrophys. J. **801**, 1, 51 (2015).

Kamionkowski, M., "How to De-Rotate the Cosmic Microwave Background Polarization", Phys.Rev.Lett. **102**, 111302 (2009).

Keisler, R., S. Hoover, N. Harrington, J. W. Henning, P. A. R. Ade, K. A. Aird, J. E. Austermann, J. A. Beall, A. N. Bender, B. A. Benson, L. E. Bleem, J. E. Carlstrom, C. L. Chang, H. C. Chiang, H.-M. Cho, R. Citron, T. M. Crawford, A. T. Crites, T. de Haan, M. A. Dobbs, W. Everett, J. Gallicchio, J. Gao, E. M. George, A. Gilbert, N. W. Halverson, D. Hanson, G. C. Hilton, G. P. Holder, W. L. Holzapfel, Z. Hou, J. D. Hrubes, N. Huang, J. Hubmayr, K. D. Irwin, L. Knox, A. T. Lee, E. M. Leitch, D. Li, D. Luong-Van, D. P. Marrone, J. J. McMahon,

J. Mehl, S. S. Meyer, L. Mocanu, T. Natoli, J. P. Nibarger, V. Novosad, S. Padin, C. Pryke, C. L. Reichardt, J. E. Ruhl, B. R. Saliwanchik, J. T. Sayre, K. K. Schaffer, E. Shirokoff, G. Smecher, A. A. Stark, K. T. Story, C. Tucker, K. Vanderlinde, J. D. Vieira, G. Wang, N. Whitehorn, V. Yefremenko and O. Zahn, "Measurements of Sub-degree B-mode Polarization in the Cosmic Microwave Background from 100 Square Degrees of SPTpol Data", ApJ**807**, 151 (2015).

Kerrigan, J., J. Pober, Z. Ali, C. Cheng, A. Parsons, J. Aguirre, N. Barry, R. Bradley, G. Bernardi, C. Carilli, D. DeBoer, J. Dillon, D. Jacobs, S. Kohn, M. Kolopanis, A. Lanman, W. Li, A. Liu and I. Sullivan, "Improved 21 cm Epoch Of Reionization Power Spectrum Measurements with a Hybrid Foreground Subtraction and Avoidance Technique", ArXiv e-prints (2018).

Kosowsky, A., "Introduction to microwave background polarization", NAR **43**, 157–168 (1999).

Kosowsky, A., T. Kahniashvili, G. Lavrelashvili and B. Ratra, "Faraday rotation of the cosmic microwave background polarization by a stochastic magnetic field", prd **71**, 4, 043006 (2005).

Kosowsky, A. and A. Loeb, "Faraday rotation of microwave background polarization by a primordial magnetic field", Astrophys.J. **469**, 1–6 (1996).

Lee, A. T. *et al.*, "A High spatial resolution analysis of the MAXIMA-1 cosmic microwave background anisotropy data", Astrophys. J. **561**, L1–L6 (2001).

Lee, K.-G., R. Cen, J. R. Gott, III and H. Trac, "The Topology of Cosmological Reionization", ApJ**675**, 8–15 (2008).

Lenc, E., B. M. Gaensler, X. H. Sun, E. M. Sadler, A. G. Willis, N. Barry, A. P. Beardsley, M. E. Bell, G. Bernardi, J. D. Bowman, F. Briggs, J. R. Callingham, R. J. Cappallo, P. Carroll, B. E. Corey, A. de Oliveira-Costa, A. A. Deshpande, J. S. Dillon, K. S. Dwarkanath, D. Emrich, A. Ewall-Wice, L. Feng, B.-Q. For, R. Goeke, L. J. Greenhill, P. Hancock, B. J. Hazelton, J. N. Hewitt, L. Hindson, N. Hurley-Walker, M. Johnston-Hollitt, D. C. Jacobs, A. D. Kapińska, D. L. Kaplan, J. C. Kasper, H.-S. Kim, E. Kratzenberg, J. Line, A. Loeb, C. J. Lonsdale, M. J. Lynch, B. McKinley, S. R. McWhirter, D. A. Mitchell, M. F. Morales, E. Morgan, J. Morgan, T. Murphy, A. R. Neben, D. Oberoi, A. R. Offringa, S. M. Ord, S. Paul, B. Pindor, J. C. Pober, T. Prabu, P. Procopio, J. Riding, A. E. E. Rogers, A. Roshi, N. Udaya Shankar, S. K. Sethi, K. S. Srivani, L. Staveley-Smith, R. Subrahmanyan, I. S. Sullivan, M. Tegmark, N. Thyagarajan, S. J. Tingay, C. Trott, M. Waterson, R. B. Wayth, R. L. Webster, A. R. Whitney, A. Williams, C. L. Williams, C. Wu, J. S. B. Wyithe and Q. Zheng, "Low-frequency Observations of Linearly Polarized Structures in the Interstellar Medium near the South Galactic Pole", ApJ**830**, 38 (2016).

Lewis, A. and A. Challinor, "Weak gravitational lensing of the CMB", Phys. Rep.**429**, 1–65 (2006).

Lewis, A., A. Challinor and A. Lasenby, "Efficient Computation of Cosmic Microwave Background Anisotropies in Closed Friedmann-Robertson-Walker Models", ApJ**538**, 473–476 (2000).

Lidz, A., O. Zahn, M. McQuinn, M. Zaldarriaga and L. Hernquist, "Detecting the Rise and Fall of 21 cm Fluctuations with the Murchison Widefield Array", ApJ**680**, 962–974 (2008).

Line, J. L. B., R. L. Webster, B. Pindor, D. A. Mitchell and C. M. Trott, "PUMA: The Positional Update and Matching Algorithm", PASA**34**, e003 (2017).

Liu, A. and A. R. Parsons, "Constraining cosmology and ionization history with combined 21 cm power spectrum and global signal measurements", MNRAS**457**, 1864–1877 (2016).

Liu, A., A. R. Parsons and C. M. Trott, "Epoch of reionization window. i. mathematical formalism", Phys. Rev. D **90**, 023018, URL http://link.aps.org/doi/10.1103/PhysRevD.90.023018 (2014a).

Liu, A., A. R. Parsons and C. M. Trott, "Epoch of reionization window. ii. statistical methods for foreground wedge reduction", Phys. Rev. D **90**, 023019, URL http://link.aps.org/doi/10.1103/PhysRevD.90.023019 (2014b).

Liu, A. and M. Tegmark, "A method for 21 cm power spectrum estimation in the presence of foregrounds", Phys. Rev. D**83**, 10, 103006 (2011).

Liu, A., M. Tegmark, S. Morrison, A. Lutomirski and M. Zaldarriaga, "Precision calibration of radio interferometers using redundant baselines", MNRAS**408**, 1029–1050 (2010).

Loeb, A., "First Light", ArXiv Astrophysics e-prints (2006).

Loeb, A. and S. R. Furlanetto, *The First Galaxies in the Universe* (Princeton University Press, 2013).

Lue, A., L. Wang and M. Kamionkowski, "Cosmological Signature of New Parity-Violating Interactions", Physical Review Letters **83**, 1506–1509 (1999).

Mather, J. C., E. S. Cheng, D. A. Cottingham, R. E. Eplee, Jr., D. J. Fixsen, T. Hewagama, R. B. Isaacman, K. A. Jensen, S. S. Meyer, P. D. Noerdlinger, S. M. Read, L. P. Rosen, R. A. Shafer, E. L. Wright, C. L. Bennett, N. W. Boggess, M. G. Hauser, T. Kelsall, S. H. Moseley, Jr., R. F. Silverberg, G. F. Smoot, R. Weiss and D. T. Wilkinson, "Measurement of the cosmic microwave background spectrum by the COBE FIRAS instrument", ApJ**420**, 439–444 (1994).

McQuinn, M., A. Lidz, O. Zahn, S. Dutta, L. Hernquist and M. Zaldarriaga, "The morphology of HII regions during reionization", MNRAS**377**, 1043–1063 (2007).

Mellema, G., L. V. E. Koopmans, F. A. Abdalla, G. Bernardi, B. Ciardi, S. Daiboo, A. G. de Bruyn, K. K. Datta, H. Falcke, A. Ferrara, I. T. Iliev, F. Iocco, V. Jelić, H. Jensen, R. Joseph, P. Labroupoulos, A. Meiksin, A. Mesinger, A. R. Offringa, V. N. Pandey, J. R. Pritchard, M. G. Santos, D. J. Schwarz, B. Semelin, H. Vedantham, S. Yatawatta and S. Zaroubi, "Reionization and the Cosmic Dawn with the Square Kilometre Array", Experimental Astronomy **36**, 235–318 (2013).

Mesinger, A. and M. Dijkstra, "Ultraviolet radiative feedback during the advanced stages of reionization", MNRAS**390**, 1071–1080 (2008).

Mesinger, A., A. Ferrara and D. S. Spiegel, "Signatures of X-rays in the early Universe", MNRAS**431**, 621–637 (2013).

Mesinger, A. and S. Furlanetto, "Efficient Simulations of Early Structure Formation and Reionization", ApJ**669**, 663–675 (2007).

Mesinger, A., S. Furlanetto and R. Cen, "21CMFAST: a fast, seminumerical simulation of the high-redshift 21-cm signal", MNRAS**411**, 955–972 (2011).

Monsalve, R. A., A. E. E. Rogers, J. D. Bowman and T. J. Mozdzen, "Results from EDGES High-band. I. Constraints on Phenomenological Models for the Global 21 cm Signal", ApJ**847**, 64 (2017).

Moore, D. F., J. E. Aguirre, S. A. Kohn, A. R. Parsons, Z. S. Ali, R. F. Bradley, C. L. Carilli, D. R. DeBoer, M. R. Dexter, N. E. Gugliucci, D. C. Jacobs, P. Klima, A. Liu, D. H. E. MacMahon, J. R. Manley, J. C. Pober, I. I. Stefan and W. P. Walbrugh, "Limits on Polarized Leakage for the PAPER Epoch of Reionization Measurements at 126 and 164 MHz", ApJ**836**, 154 (2017).

Morales, M. F., J. D. Bowman and J. N. Hewitt, "Improving Foreground Subtraction in Statistical Observations of 21 cm Emission from the Epoch of Reionization", ApJ**648**, 767–773 (2006).

Morales, M. F., B. Hazelton, I. Sullivan and A. Beardsley, "Four Fundamental Foreground Power Spectrum Shapes for 21 cm Cosmology Observations", ApJ**752**, 137 (2012).

Morales, M. F. and J. S. B. Wyithe, "Reionization and Cosmology with 21-cm Fluctuations", ARA&A**48**, 127–171 (2010).

Naess, S., M. Hasselfield, J. McMahon, M. D. Niemack, G. E. Addison, P. A. R. Ade, R. Allison, M. Amiri, N. Battaglia, J. A. Beall, F. de Bernardis, J. R. Bond, J. Britton, E. Calabrese, H.-m. Cho, K. Coughlin, D. Crichton, S. Das, R. Datta,

M. J. Devlin, S. R. Dicker, J. Dunkley, R. Dünner, J. W. Fowler, A. E. Fox, P. Gallardo, E. Grace, M. Gralla, A. Hajian, M. Halpern, S. Henderson, J. C. Hill, G. C. Hilton, M. Hilton, A. D. Hincks, R. Hlozek, P. Ho, J. Hubmayr, K. M. Huffenberger, J. P. Hughes, L. Infante, K. Irwin, R. Jackson, S. Muya Kasanda, J. Klein, B. Koopman, A. Kosowsky, D. Li, T. Louis, M. Lungu, M. Madhavacheril, T. A. Marriage, L. Maurin, F. Menanteau, K. Moodley, C. Munson, L. Newburgh, J. Nibarger, M. R. Nolta, L. A. Page, C. Pappas, B. Partridge, F. Rojas, B. L. Schmitt, N. Sehgal, B. D. Sherwin, J. Sievers, S. Simon, D. N. Spergel, S. T. Staggs, E. R. Switzer, R. Thornton, H. Trac, C. Tucker, M. Uehara, A. Van Engelen, J. T. Ward and E. J. Wollack, "The Atacama Cosmology Telescope: CMB polarization at $200 < l < 9000$", J. Cosmology Astropart. Phys.**10**, 007 (2014).

Oh, S. P., "Reionization by Hard Photons. I. X-Rays from the First Star Clusters", ApJ**553**, 499–512 (2001).

Oppermann, N., H. Junklewitz, M. Greiner, T. A. Enßlin, T. Akahori, E. Carretti, B. M. Gaensler, A. Goobar, L. Harvey-Smith, M. Johnston-Hollitt, L. Pratley, D. H. F. M. Schnitzeler, J. M. Stil and V. Vacca, "Estimating extragalactic Faraday rotation", A&A**575**, A118 (2015).

Orlando, E. and A. Strong, "Galactic synchrotron emission with cosmic ray propagation models", MNRAS**436**, 2127–2142 (2013).

Paciga, G., J. G. Albert, K. Bandura, T.-C. Chang, Y. Gupta, C. Hirata, J. Odegova, U.-L. Pen, J. B. Peterson, J. Roy, J. R. Shaw, K. Sigurdson and T. Voytek, "A simulation-calibrated limit on the H I power spectrum from the GMRT Epoch of Reionization experiment", MNRAS**433**, 639–647 (2013).

Padin, S. *et al.*, "First intrinsic anisotropy observations with the cosmic background imager", Astrophys. J. **549**, L1 (2001).

Parsons, A., J. Pober, M. McQuinn, D. Jacobs and J. Aguirre, "A Sensitivity and Array-configuration Study for Measuring the Power Spectrum of 21 cm Emission from Reionization", ApJ**753**, 81 (2012).

Parsons, A. R. and D. C. Backer, "Calibration of Low-Frequency, Wide-Field Radio Interferometers Using Delay/Delay-Rate Filtering", AJ**138**, 219–226 (2009).

Parsons, A. R., D. C. Backer, G. S. Foster, M. C. H. Wright, R. F. Bradley, N. E. Gugliucci, C. R. Parashare, E. E. Benoit, J. E. Aguirre, D. C. Jacobs, C. L. Carilli, D. Herne, M. J. Lynch, J. R. Manley and D. J. Werthimer, "The Precision Array for Probing the Epoch of Re-ionization: Eight Station Results", AJ**139**, 1468–1480 (2010).

Parsons, A. R., A. Liu, J. E. Aguirre, Z. S. Ali, R. F. Bradley, C. L. Carilli, D. R. DeBoer, M. R. Dexter, N. E. Gugliucci, D. C. Jacobs, P. Klima, D. H. E. MacMahon, J. R. Manley, D. F. Moore, J. C. Pober, I. I. Stefan and W. P. Walbrugh, "New Limits on 21 cm Epoch of Reionization from PAPER-32 Consistent with an X-Ray Heated Intergalactic Medium at z = 7.7", ApJ**788**, 106 (2014).

Parsons, A. R., A. Liu, Z. S. Ali and C. Cheng, "Optimized Beam Sculpting with Generalized Fringe-rate Filters", ApJ**820**, 51 (2016).

Patil, A. H., S. Yatawatta, L. V. E. Koopmans, A. G. de Bruyn, M. A. Brentjens, S. Zaroubi, K. M. B. Asad, M. Hatef, V. Jelić, M. Mevius, A. R. Offringa, V. N. Pandey, H. Vedantham, F. B. Abdalla, W. N. Brouw, E. Chapman, B. Ciardi, B. K. Gehlot, A. Ghosh, G. Harker, I. T. Iliev, K. Kakiichi, S. Majumdar, G. Mellema, M. B. Silva, J. Schaye, D. Vrbanec and S. J. Wijnholds, "Upper Limits on the 21 cm Epoch of Reionization Power Spectrum from One Night with LOFAR", ApJ**838**, 65 (2017).

Patra, N., R. Subrahmanyan, S. Sethi, N. Udaya Shankar and A. Raghunathan, "Saras Measurement of the Radio Background At Long Wavelengths", ApJ**801**, 138 (2015).

Peebles, P. J. E. and J. T. Yu, "Primeval Adiabatic Perturbation in an Expanding Universe", ApJ**162**, 815 (1970).

Peterson, J. B., U.-L. Pen and X.-P. Wu, "The Primeval Structure Telescope", Modern Physics Letters A **19**, 1001–1008 (2004).

Planck Collaboration, R. Adam, P. A. R. Ade, N. Aghanim, Y. Akrami, M. I. R. Alves, F. Argüeso, M. Arnaud, F. Arroja, M. Ashdown and et al., "Planck 2015 results. I. Overview of products and scientific results", A&A**594**, A1 (2016a).

Planck Collaboration, R. Adam, P. A. R. Ade, N. Aghanim, M. I. R. Alves, M. Arnaud, M. Ashdown, J. Aumont, C. Baccigalupi, A. J. Banday and et al., "Planck 2015 results. X. Diffuse component separation: Foreground maps", A&A**594**, A10 (2016b).

Planck Collaboration, P. A. R. Ade, N. Aghanim, D. Alina, M. I. R. Alves, G. Aniano, C. Armitage-Caplan, M. Arnaud, D. Arzoumanian, M. Ashdown, F. Atrio-Barandela, J. Aumont, C. Baccigalupi, A. J. Banday, R. B. Barreiro, E. Battaner, K. Benabed, A. Benoit-Lévy, J.-P. Bernard, M. Bersanelli, P. Bielewicz, J. R. Bond, J. Borrill, F. R. Bouchet, F. Boulanger, A. Bracco, C. Burigana, J.-F. Cardoso, A. Catalano, A. Chamballu, H. C. Chiang, P. R. Christensen, S. Colombi, L. P. L. Colombo, C. Combet, F. Couchot, A. Coulais, B. P. Crill, A. Curto, F. Cuttaia, L. Danese, R. D. Davies, R. J. Davis, P. de Bernardis, A. de Rosa, G. de Zotti, J. Delabrouille, C. Dickinson, J. M. Diego, S. Donzelli, O. Doré, M. Douspis, X. Dupac, G. Efstathiou, T. A. Enßlin, H. K. Eriksen, E. Falgarone, L. Fanciullo,

K. Ferrière, F. Finelli, O. Forni, M. Frailis, A. A. Fraisse, E. Franceschi, S. Galeotta, K. Ganga, T. Ghosh, M. Giard, Y. Giraud-Héraud, J. González-Nuevo, K. M. Górski, A. Gregorio, A. Gruppuso, V. Guillet, F. K. Hansen, D. L. Harrison, G. Helou, C. Hernández-Monteagudo, S. R. Hildebrandt, E. Hivon, M. Hobson, W. A. Holmes, A. Hornstrup, K. M. Huffenberger, A. H. Jaffe, T. R. Jaffe, W. C. Jones, M. Juvela, E. Keihänen, R. Keskitalo, T. S. Kisner, R. Kneissl, J. Knoche, M. Kunz, H. Kurki-Suonio, G. Lagache, J.-M. Lamarre, A. Lasenby, C. R. Lawrence, R. Leonardi, F. Levrier, M. Liguori, P. B. Lilje, M. Linden-Vørnle, M. López-Caniego, P. M. Lubin, J. F. Macías-Pérez, D. Maino, N. Mandolesi, M. Maris, D. J. Marshall, P. G. Martin, E. Martínez-González, S. Masi, S. Matarrese, P. Mazzotta, A. Melchiorri, L. Mendes, A. Mennella, M. Migliaccio, M.-A. Miville-Deschênes, A. Moneti, L. Montier, G. Morgante, D. Mortlock, D. Munshi, J. A. Murphy, P. Naselsky, F. Nati, P. Natoli, C. B. Netterfield, F. Noviello, D. Novikov, I. Novikov, C. A. Oxborrow, L. Pagano, F. Pajot, D. Paoletti, F. Pasian, V.-M. Pelkonen, O. Perdereau, L. Perotto, F. Perrotta, F. Piacentini, M. Piat, D. Pietrobon, S. Plaszczynski, E. Pointecouteau, G. Polenta, L. Popa, G. W. Pratt, S. Prunet, J.-L. Puget, J. P. Rachen, M. Reinecke, M. Remazeilles, C. Renault, S. Ricciardi, T. Riller, I. Ristorcelli, G. Rocha, C. Rosset, G. Roudier, B. Rusholme, M. Sandri, D. Scott, J. D. Soler, L. D. Spencer, V. Stolyarov, R. Stompor, R. Sudiwala, D. Sutton, A.-S. Suur-Uski, J.-F. Sygnet, J. A. Tauber, L. Terenzi, L. Toffolatti, M. Tomasi, M. Tristram, M. Tucci, G. Umana, L. Valenziano, J. Valiviita, B. Van Tent, P. Vielva, F. Villa, L. A. Wade, B. D. Wandelt and A. Zonca, "Planck intermediate results. XX. Comparison of polarized thermal emission from Galactic dust with simulations of MHD turbulence", A&A**576**, A105 (2015a).

Planck Collaboration, P. A. R. Ade, N. Aghanim, D. Alina, M. I. R. Alves, C. Armitage-Caplan, M. Arnaud, D. Arzoumanian, M. Ashdown, F. Atrio-Barandela and et al., "Planck intermediate results. XIX. An overview of the polarized thermal emission from Galactic dust", A&A**576**, A104 (2015b).

Planck Collaboration, P. A. R. Ade, N. Aghanim, M. I. R. Alves, M. Arnaud, M. Ashdown, J. Aumont, C. Baccigalupi, A. J. Banday, R. B. Barreiro and et al., "Planck 2015 results. XXV. Diffuse low-frequency Galactic foregrounds", A&A**594**, A25 (2016c).

Planck Collaboration, P. A. R. Ade, N. Aghanim, M. Arnaud, F. Arroja, M. Ashdown, J. Aumont, C. Baccigalupi, M. Ballardini, A. J. Banday and et al., "Planck 2015 results. XIX. Constraints on primordial magnetic fields", A&A**594**, A19 (2016d).

Planck Collaboration, P. A. R. Ade, N. Aghanim, M. Arnaud, M. Ashdown, J. Aumont, C. Baccigalupi, A. J. Banday, R. B. Barreiro, J. G. Bartlett and et al., "Planck 2015 results. XIII. Cosmological parameters", A&A**594**, A13 (2016e).

Pober, J. C., Z. S. Ali, A. R. Parsons, M. McQuinn, J. E. Aguirre, G. Bernardi, R. F. Bradley, C. L. Carilli, C. Cheng, D. R. DeBoer, M. R. Dexter, S. R. Furlanetto, J. Grobbelaar, J. Horrell, D. C. Jacobs, P. J. Klima, S. A. Kohn, A. Liu, D. H. E. MacMahon, M. Maree, A. Mesinger, D. F. Moore, N. Razavi-Ghods, I. I. Stefan, W. P. Walbrugh, A. Walker and H. Zheng, "PAPER-64 Constraints On Reionization. II. The Temperature of the z =8.4 Intergalactic Medium", ApJ**809**, 62 (2015).

Pober, J. C., B. J. Hazelton, A. P. Beardsley, N. A. Barry, Z. E. Martinot, I. S. Sullivan, M. F. Morales, M. E. Bell, G. Bernardi, N. D. R. Bhat, J. D. Bowman, F. Briggs, R. J. Cappallo, P. Carroll, B. E. Corey, A. de Oliveira-Costa, A. A. Deshpande, J. S. Dillon, D. Emrich, A. M. Ewall-Wice, L. Feng, R. Goeke, L. J. Greenhill, J. N. Hewitt, L. Hindson, N. Hurley-Walker, D. C. Jacobs, M. Johnston-Hollitt, D. L. Kaplan, J. C. Kasper, H.-S. Kim, P. Kittiwisit, E. Kratzenberg, N. Kudryavtseva, E. Lenc, J. Line, A. Loeb, C. J. Lonsdale, M. J. Lynch, B. McKinley, S. R. McWhirter, D. A. Mitchell, E. Morgan, A. R. Neben, D. Oberoi, A. R. Offringa, S. M. Ord, S. Paul, B. Pindor, T. Prabu, P. Procopio, J. Riding, A. E. E. Rogers, A. Roshi, S. K. Sethi, N. Udaya Shankar, K. S. Srivani, R. Subrahmanyan, M. Tegmark, N. Thyagarajan, S. J. Tingay, C. M. Trott, M. Waterson, R. B. Wayth, R. L. Webster, A. R. Whitney, A. Williams, C. L. Williams and J. S. B. Wyithe, "The Importance of Wide-field Foreground Removal for 21 cm Cosmology: A Demonstration with Early MWA Epoch of Reionization Observations", ApJ**819**, 8 (2016).

Pober, J. C., A. Liu, J. S. Dillon, J. E. Aguirre, J. D. Bowman, R. F. Bradley, C. L. Carilli, D. R. DeBoer, J. N. Hewitt, D. C. Jacobs, M. McQuinn, M. F. Morales, A. R. Parsons, M. Tegmark and D. J. Werthimer, "What Next-generation 21 cm Power Spectrum Measurements can Teach us About the Epoch of Reionization", ApJ**782**, 66 (2014).

Pober, J. C., A. R. Parsons, J. E. Aguirre, Z. Ali, R. F. Bradley, C. L. Carilli, D. DeBoer, M. Dexter, N. E. Gugliucci, D. C. Jacobs, P. J. Klima, D. MacMahon, J. Manley, D. F. Moore, I. I. Stefan and W. P. Walbrugh, "Opening the 21cm Epoch of Reionization Window: Measurements of Foreground Isolation with PAPER", ApJ**768**, L36 (2013).

Pogosian, L., "Searching for primordial magnetism with multifrequency cosmic microwave background experiments", MNRAS **438**, 2508–2512 (2014).

Polenta, G., D. Marinucci, A. Balbi, P. de Bernardis, E. Hivon, S. Masi, P. Natoli and N. Vittorio, "Unbiased estimation of an angular power spectrum", JCAP **11**, 001 (2005).

Presley, M., A. Liu and A. Parsons, "Measuring the Cosmological 21 cm Monopole with an Interferometer", ArXiv e-prints: 1501.01633 (2015).

Pritchard, J. R. and A. Loeb, "Constraining the unexplored period between the dark ages and reionization with observations of the global 21 cm signal", Phys. Rev. D**82**, 2, 023006 (2010).

Pritchard, J. R. and A. Loeb, "21 cm cosmology in the 21st century", Reports on Progress in Physics **75**, 8, 086901 (2012).

Quashnock, J. M., A. Loeb and D. N. Spergel, "Magnetic field generation during the cosmological QCD phase transition", ApJ**344**, L49–L51 (1989).

Ranalli, P., A. Comastri and G. Setti, "The 2-10 keV luminosity as a Star Formation Rate indicator", A&A**399**, 39–50 (2003).

Ratra, B., "Cosmological 'seed' magnetic field from inflation", ApJ**391**, L1–L4 (1992).

Reichardt, C. L., "Observing the Epoch of Reionization with the Cosmic Microwave Background", (2015).

Ryu, D., D. R. G. Schleicher, R. A. Treumann, C. G. Tsagas and L. M. Widrow, "Magnetic Fields in the Large-Scale Structure of the Universe", Space Sci. Rev.**166**, 1–35 (2012).

Sachs, R. K. and A. M. Wolfe, "Perturbations of a Cosmological Model and Angular Variations of the Microwave Background", ApJ**147**, 73 (1967).

Santos, M. G., A. Amblard, J. Pritchard, H. Trac, R. Cen and A. Cooray, "Cosmic Reionization and the 21 cm Signal: Comparison between an Analytical Model and a Simulation", ApJ**689**, 1–16 (2008).

Santos, M. G., A. Cooray and L. Knox, "Multifrequency Analysis of 21 Centimeter Fluctuations from the Era of Reionization", ApJ**625**, 575–587 (2005).

Scóccola, C., D. Harari and S. Mollerach, "B polarization of the CMB from Faraday rotation", Phys. Rev. D**70**, 6, 063003 (2004).

Seager, S., D. D. Sasselov and D. Scott, "A new calculation of the recombination epoch", Astrophys. J. **523**, L1–L5 (1999).

Shibusawa, Y., K. Ichiki and K. Kadota, "The influence of primordial magnetic fields on the spherical collapse model in cosmology", Journal of Cosmology and Astroparticle Physics **8**, 017 (2014).

Shin, M.-S., H. Trac and R. Cen, "Cosmological H II Bubble Growth during Reionization", ApJ**681**, 756–770 (2008).

Shull, J. M. and M. E. van Steenberg, "X-ray secondary heating and ionization in quasar emission-line clouds", ApJ**298**, 268–274 (1985).

Sokolowski, M., S. E. Tremblay, R. B. Wayth, S. J. Tingay, N. Clarke, P. Roberts, M. Waterson, R. D. Ekers, P. Hall, M. Lewis, M. Mossammaparast, S. Padhi, F. Schlagenhaufer, A. Sutinjo and J. Tickner, "BIGHORNS - Broadband Instrument for Global HydrOgen ReioNisation Signal", PASA **32**, 4 (2015).

Sotomayor-Beltran, C., C. Sobey, J. W. T. Hessels, G. de Bruyn, A. Noutsos, A. Alexov, J. Anderson, A. Asgekar, I. M. Avruch, R. Beck, M. E. Bell, M. R. Bell, M. J. Bentum, G. Bernardi, P. Best, L. Birzan, A. Bonafede, F. Breitling, J. Broderick, W. N. Brouw, M. Brüggen, B. Ciardi, F. de Gasperin, R.-J. Dettmar, A. van Duin, S. Duscha, J. Eislöffel, H. Falcke, R. A. Fallows, R. Fender, C. Ferrari, W. Frieswijk, M. A. Garrett, J. Grießmeier, T. Grit, A. W. Gunst, T. E. Hassall, G. Heald, M. Hoeft, A. Horneffer, M. Iacobelli, E. Juette, A. Karastergiou, E. Keane, J. Kohler, M. Kramer, V. I. Kondratiev, L. V. E. Koopmans, M. Kuniyoshi, G. Kuper, J. van Leeuwen, P. Maat, G. Macario, S. Markoff, J. P. McKean, D. D. Mulcahy, H. Munk, E. Orru, H. Paas, M. Pandey-Pommier, M. Pilia, R. Pizzo, A. G. Polatidis, W. Reich, H. Röttgering, M. Serylak, J. Sluman, B. W. Stappers, M. Tagger, Y. Tang, C. Tasse, S. ter Veen, R. Vermeulen, R. J. van Weeren, R. A. M. J. Wijers, S. J. Wijnholds, M. W. Wise, O. Wucknitz, S. Yatawatta and P. Zarka, "Calibrating high-precision Faraday rotation measurements for LOFAR and the next generation of low-frequency radio telescopes", A&A**552**, A58 (2013).

Sotomayor-Beltran, C., C. Sobey, J. W. T. Hessels, G. de Bruyn, A. Noutsos, A. Alexov, J. Anderson, A. Asgekar, I. M. Avruch, R. Beck, M. E. Bell, M. R. Bell, M. J. Bentum, G. Bernardi, P. Best, L. Birzan, A. Bonafede, F. Breitling, J. Broderick, W. N. Brouw, M. Brüggen, B. Ciardi, F. de Gasperin, R.-J. Dettmar, A. van Duin, S. Duscha, J. Eislöffel, H. Falcke, R. A. Fallows, R. Fender, C. Ferrari, W. Frieswijk, M. A. Garrett, J. Grießmeier, T. Grit, A. W. Gunst, T. E. Hassall, G. Heald, M. Hoeft, A. Horneffer, M. Iacobelli, E. Juette, A. Karastergiou, E. Keane, J. Kohler, M. Kramer, V. I. Kondratiev, L. V. E. Koopmans, M. Kuniyoshi, G. Kuper, J. van Leeuwen, P. Maat, G. Macario, S. Markoff, J. P. McKean, D. D. Mulcahy, H. Munk, E. Orru, H. Paas, M. Pandey-Pommier, M. Pilia, R. Pizzo, A. G. Polatidis, W. Reich, H. Röttgering, M. Serylak, J. Sluman, B. W. Stappers, M. Tagger, Y. Tang, C. Tasse, S. ter Veen, R. Vermeulen, R. J. van Weeren, R. A. M. J. Wijers, S. J. Wijnholds, M. W. Wise, O. Wucknitz, S. Yatawatta and P. Zarka, "Calibrating high-precision faraday rotation measurements for LOFAR and the next generation of low-frequency radio telescopes (corrigendum)", Astronomy & Astrophysics **581**, C4 (2015).

Stompor, R. *et al.*, "Cosmological implications of the MAXIMA-I high resolution cosmic microwave background anisotropy measurement", Astrophys. J. **561**, L7–L10 (2001).

Sullivan, I. S., M. F. Morales, B. J. Hazelton, W. Arcus, D. Barnes, G. Bernardi, F. H. Briggs, J. D. Bowman, J. D. Bunton, R. J. Cappallo, B. E. Corey, A. Deshpande,

L. deSouza, D. Emrich, B. M. Gaensler, R. Goeke, L. J. Greenhill, D. Herne, J. N. Hewitt, M. Johnston-Hollitt, D. L. Kaplan, J. C. Kasper, B. B. Kincaid, R. Koenig, E. Kratzenberg, C. J. Lonsdale, M. J. Lynch, S. R. McWhirter, D. A. Mitchell, E. Morgan, D. Oberoi, S. M. Ord, J. Pathikulangara, T. Prabu, R. A. Remillard, A. E. E. Rogers, A. Roshi, J. E. Salah, R. J. Sault, N. Udaya Shankar, K. S. Srivani, J. Stevens, R. Subrahmanyan, S. J. Tingay, R. B. Wayth, M. Waterson, R. L. Webster, A. R. Whitney, A. Williams, C. L. Williams and J. S. B. Wyithe, "Fast Holographic Deconvolution: A New Technique for Precision Radio Interferometry", ApJ**759**, 17 (2012).

Sunyaev, R. A. and Y. B. Zeldovich, "The Observations of Relic Radiation as a Test of the Nature of X-Ray Radiation from the Clusters of Galaxies", Comments on Astrophysics and Space Physics **4**, 173 (1972).

Switzer, E. R. and A. Liu, "Erasing the variable: Empirical foreground discovery for global 21 cm spectrum experiments", The Astrophysical Journal **793**, 2, 102, URL http://stacks.iop.org/0004-637X/793/i=2/a=102 (2014).

Tashiro, H., N. Aghanim and M. Langer, "Secondary B-mode polarization from Faraday rotation in clusters and galaxies", mnras **384**, 733–746 (2008).

Tegmark, M., "How to measure CMB power spectra without losing information", Phys. Rev. D**55**, 5895–5907 (1997).

The Polarbear Collaboration, P. A. R. Ade, Y. Akiba, A. E. Anthony, K. Arnold, M. Atlas, D. Barron, D. Boettger, J. Borrill, S. Chapman, Y. Chinone, M. Dobbs, T. Elleflot, J. Errard, G. Fabbian, C. Feng, D. Flanigan, A. Gilbert, W. Grainger, N. W. Halverson, M. Hasegawa, K. Hattori, M. Hazumi, W. L. Holzapfel, Y. Hori, J. Howard, P. Hyland, Y. Inoue, G. C. Jaehnig, A. H. Jaffe, B. Keating, Z. Kermish, R. Keskitalo, T. Kisner, M. Le Jeune, A. T. Lee, E. M. Leitch, E. Linder, M. Lungu, F. Matsuda, T. Matsumura, X. Meng, N. J. Miller, H. Morii, S. Moyerman, M. J. Myers, M. Navaroli, H. Nishino, A. Orlando, H. Paar, J. Peloton, D. Poletti, E. Quealy, G. Rebeiz, C. L. Reichardt, P. L. Richards, C. Ross, I. Schanning, D. E. Schenck, B. D. Sherwin, A. Shimizu, C. Shimmin, M. Shimon, P. Siritanasak, G. Smecher, H. Spieler, N. Stebor, B. Steinbach, R. Stompor, A. Suzuki, S. Takakura, T. Tomaru, B. Wilson, A. Yadav and O. Zahn, "A Measurement of the Cosmic Microwave Background B-mode Polarization Power Spectrum at Sub-degree Scales with POLARBEAR", ApJ**794**, 171 (2014).

Thomas, R. M., S. Zaroubi, B. Ciardi, A. H. Pawlik, P. Labropoulos, V. Jelić, G. Bernardi, M. A. Brentjens, A. G. de Bruyn, G. J. A. Harker, L. V. E. Koopmans, G. Mellema, V. N. Pandey, J. Schaye and S. Yatawatta, "Fast large-scale reionization simulations", MNRAS**393**, 32–48 (2009).

Thyagarajan, N., D. C. Jacobs, J. D. Bowman, N. Barry, A. P. Beardsley, G. Bernardi, F. Briggs, R. J. Cappallo, P. Carroll, B. E. Corey, A. de Oliveira-Costa, J. S. Dillon, D. Emrich, A. Ewall-Wice, L. Feng, R. Goeke, L. J. Greenhill, B. J. Hazelton, J. N. Hewitt, N. Hurley-Walker, M. Johnston-Hollitt, D. L. Kaplan, J. C. Kasper, H.-S. Kim, P. Kittiwisit, E. Kratzenberg, E. Lenc, J. Line, A. Loeb, C. J. Lonsdale, M. J. Lynch, B. McKinley, S. R. McWhirter, D. A. Mitchell, M. F. Morales, E. Morgan, A. R. Neben, D. Oberoi, A. R. Offringa, S. M. Ord, S. Paul, B. Pindor, J. C. Pober, T. Prabu, P. Procopio, J. Riding, A. E. E. Rogers, A. Roshi, N. Udaya Shankar, S. K. Sethi, K. S. Srivani, R. Subrahmanyan, I. S. Sullivan, M. Tegmark, S. J. Tingay, C. M. Trott, M. Waterson, R. B. Wayth, R. L. Webster, A. R. Whitney, A. Williams, C. L. Williams, C. Wu and J. S. B. Wyithe, "Foregrounds in Wide-field Redshifted 21 cm Power Spectra", ApJ**804**, 14 (2015a).

Thyagarajan, N., D. C. Jacobs, J. D. Bowman, N. Barry, A. P. Beardsley, G. Bernardi, F. Briggs, R. J. Cappallo, P. Carroll, A. A. Deshpande, A. de Oliveira-Costa, J. S. Dillon, A. Ewall-Wice, L. Feng, L. J. Greenhill, B. J. Hazelton, L. Hernquist, J. N. Hewitt, N. Hurley-Walker, M. Johnston-Hollitt, D. L. Kaplan, H.-S. Kim, P. Kittiwisit, E. Lenc, J. Line, A. Loeb, C. J. Lonsdale, B. McKinley, S. R. McWhirter, D. A. Mitchell, M. F. Morales, E. Morgan, A. R. Neben, D. Oberoi, A. R. Offringa, S. M. Ord, S. Paul, B. Pindor, J. C. Pober, T. Prabu, P. Procopio, J. Riding, N. Udaya Shankar, S. K. Sethi, K. S. Srivani, R. Subrahmanyan, I. S. Sullivan, M. Tegmark, S. J. Tingay, C. M. Trott, R. B. Wayth, R. L. Webster, A. Williams, C. L. Williams and J. S. B. Wyithe, "Confirmation of Wide-field Signatures in Redshifted 21 cm Power Spectra", ApJ**807**, L28 (2015b).

Thyagarajan, N., N. Udaya Shankar, R. Subrahmanyan, W. Arcus, G. Bernardi, J. D. Bowman, F. Briggs, J. D. Bunton, R. J. Cappallo, B. E. Corey, L. deSouza, D. Emrich, B. M. Gaensler, R. F. Goeke, L. J. Greenhill, B. J. Hazelton, D. Herne, J. N. Hewitt, M. Johnston-Hollitt, D. L. Kaplan, J. C. Kasper, B. B. Kincaid, R. Koenig, E. Kratzenberg, C. J. Lonsdale, M. J. Lynch, S. R. McWhirter, D. A. Mitchell, M. F. Morales, E. H. Morgan, D. Oberoi, S. M. Ord, J. Pathikulangara, R. A. Remillard, A. E. E. Rogers, D. Anish Roshi, J. E. Salah, R. J. Sault, K. S. Srivani, J. B. Stevens, P. Thiagaraj, S. J. Tingay, R. B. Wayth, M. Waterson, R. L. Webster, A. R. Whitney, A. J. Williams, C. L. Williams and J. S. B. Wyithe, "A Study of Fundamental Limitations to Statistical Detection of Redshifted H I from the Epoch of Reionization", ApJ**776**, 6 (2013).

Tingay, S. J., R. Goeke, J. D. Bowman, D. Emrich, S. M. Ord, D. A. Mitchell, M. F. Morales, T. Booler, B. Crosse, R. B. Wayth, C. J. Lonsdale, S. Tremblay, D. Pallot, T. Colegate, A. Wicenec, N. Kudryavtseva, W. Arcus, D. Barnes, G. Bernardi, F. Briggs, S. Burns, J. D. Bunton, R. J. Cappallo, B. E. Corey, A. Deshpande, L. Desouza, B. M. Gaensler, L. J. Greenhill, P. J. Hall, B. J. Hazelton, D. Herne, J. N. Hewitt, M. Johnston-Hollitt, D. L. Kaplan, J. C. Kasper, B. B. Kincaid, R. Koenig,

E. Kratzenberg, M. J. Lynch, B. Mckinley, S. R. Mcwhirter, E. Morgan, D. Oberoi, J. Pathikulangara, T. Prabu, R. A. Remillard, A. E. E. Rogers, A. Roshi, J. E. Salah, R. J. Sault, N. Udaya-Shankar, F. Schlagenhaufer, K. S. Srivani, J. Stevens, R. Subrahmanyan, M. Waterson, R. L. Webster, A. R. Whitney, A. Williams, C. L. Williams and J. S. B. Wyithe, "The Murchison Widefield Array: The Square Kilometre Array Precursor at Low Radio Frequencies", PASA **30**, 7 (2013).

Trott, C. M., "Comparison of Observing Modes for Statistical Estimation of the 21 cm Signal from the Epoch of Reionisation", PASA **31**, e026 (2014).

Trott, C. M., B. Pindor, P. Procopio, R. B. Wayth, D. A. Mitchell, B. McKinley, S. J. Tingay, N. Barry, A. P. Beardsley, G. Bernardi, J. D. Bowman, F. Briggs, R. J. Cappallo, P. Carroll, A. de Oliveira-Costa, J. S. Dillon, A. Ewall-Wice, L. Feng, L. J. Greenhill, B. J. Hazelton, J. N. Hewitt, N. Hurley-Walker, M. Johnston-Hollitt, D. C. Jacobs, D. L. Kaplan, H. S. Kim, E. Lenc, J. Line, A. Loeb, C. J. Lonsdale, M. F. Morales, E. Morgan, A. R. Neben, N. Thyagarajan, D. Oberoi, A. R. Offringa, S. M. Ord, S. Paul, J. C. Pober, T. Prabu, J. Riding, N. U. Shankar, S. K. Sethi, K. S. Srivani, R. Subrahmanyan, I. S. Sullivan, M. Tegmark, R. L. Webster, A. Williams, C. L. Williams, C. Wu and J. S. B. Wyithe, "Chips: The cosmological h i power spectrum estimator", The Astrophysical Journal **818**, 2, 139, URL http://stacks.iop.org/0004-637X/818/i=2/a=139 (2016).

Trott, C. M., R. B. Wayth and S. J. Tingay, "The Impact of Point-source Subtraction Residuals on 21 cm Epoch of Reionization Estimation", ApJ**757**, 101 (2012).

Vachaspati, T., "Magnetic fields from cosmological phase transitions", Physics Letters B **265**, 258–261 (1991).

van Engelen, A. *et al.*, "The Atacama Cosmology Telescope: Lensing of CMB Temperature and Polarization Derived from Cosmic Infrared Background Cross-Correlation", Astrophys. J. **808**, 1, 7 (2015).

Vansyngel, F., F. Boulanger, T. Ghosh, B. Wandelt, J. Aumont, A. Bracco, F. Levrier, P. G. Martin and L. Montier, "Statistical simulations of the dust foreground to cosmic microwave background polarization", A&A**603**, A62 (2017).

Vedantham, H., N. Udaya Shankar and R. Subrahmanyan, "Imaging the Epoch of Reionization: Limitations from Foreground Confusion and Imaging Algorithms", ApJ**745**, 176 (2012).

Voytek, T. C., A. Natarajan, J. M. Jáuregui García, J. B. Peterson and O. López-Cruz, "Probing the Dark Ages at z ~ 20: The SCI-HI 21 cm All-sky Spectrum Experiment", ApJ**782**, L9 (2014a).

Voytek, T. C., A. Natarajan, J. M. Jáuregui García, J. B. Peterson and O. López-Cruz, "Probing the Dark Ages at z ˜ 20: The SCI-HI 21 cm All-sky Spectrum Experiment", ApJ**782**, L9 (2014b).

Wasserman, I., "On the origins of galaxies, galactic angular momenta, and galactic magnetic fields", ApJ**224**, 337–343 (1978).

Wayth, R. B., E. Lenc, M. E. Bell, J. R. Callingham, K. S. Dwarakanath, T. M. O. Franzen, B.-Q. For, B. Gaensler, P. Hancock, L. Hindson, N. Hurley-Walker, C. A. Jackson, M. Johnston-Hollitt, A. D. Kapińska, B. McKinley, J. Morgan, A. R. Offringa, P. Procopio, L. Staveley-Smith, C. Wu, Q. Zheng, C. M. Trott, G. Bernardi, J. D. Bowman, F. Briggs, R. J. Cappallo, B. E. Corey, A. A. Deshpande, D. Emrich, R. Goeke, L. J. Greenhill, B. J. Hazelton, D. L. Kaplan, J. C. Kasper, E. Kratzenberg, C. J. Lonsdale, M. J. Lynch, S. R. McWhirter, D. A. Mitchell, M. F. Morales, E. Morgan, D. Oberoi, S. M. Ord, T. Prabu, A. E. E. Rogers, A. Roshi, N. U. Shankar, K. S. Srivani, R. Subrahmanyan, S. J. Tingay, M. Waterson, R. L. Webster, A. R. Whitney, A. Williams and C. L. Williams, "GLEAM: The GaLactic and Extragalactic All-Sky MWA Survey", PASA **32**, e025 (2015).

Weinberg, S., "Entropy Generation and the Survival of Protogalaxies in an Expanding Universe", ApJ**168**, 175 (1971).

Widrow, L. M., "Origin of galactic and extragalactic magnetic fields", Reviews of Modern Physics **74**, 775–823 (2002).

Wu, X., "Probing the Epoch of Reionization with 21CMA: Status and Prospects", in "American Astronomical Society Meeting Abstracts 213", vol. 41 of *Bulletin of the American Astronomical Society*, p. 226.05 (2009).

Yadav, A. P. S., R. Biswas, M. Su and M. Zaldarriaga, "Constraining a spatially dependent rotation of the cosmic microwave background polarization", Phys. Rev. D**79**, 12, 123009 (2009).

Yatawatta, S., A. G. de Bruyn, M. A. Brentjens, P. Labropoulos, V. N. Pandey, S. Kazemi, S. Zaroubi, L. V. E. Koopmans, A. R. Offringa, V. Jelić, O. Martinez Rubi, V. Veligatla, S. J. Wijnholds, W. N. Brouw, G. Bernardi, B. Ciardi, S. Daiboo, G. Harker, G. Mellema, J. Schaye, R. Thomas, H. Vedantham, E. Chapman, F. B. Abdalla, A. Alexov, J. Anderson, I. M. Avruch, F. Batejat, M. E. Bell, M. R. Bell, M. Bentum, P. Best, A. Bonafede, J. Bregman, F. Breitling, R. H. van de Brink, J. W. Broderick, M. Brüggen, J. Conway, F. de Gasperin, E. de Geus, S. Duscha, H. Falcke, R. A. Fallows, C. Ferrari, W. Frieswijk, M. A. Garrett, J. M. Griessmeier, A. W. Gunst, T. E. Hassall, J. W. T. Hessels, M. Hoeft, M. Iacobelli, E. Juette, A. Karastergiou, V. I. Kondratiev, M. Kramer, M. Kuniyoshi, G. Kuper, J. van Leeuwen, P. Maat, G. Mann, J. P. McKean, M. Mevius, J. D. Mol, H. Munk,

R. Nijboer, J. E. Noordam, M. J. Norden, E. Orru, H. Paas, M. Pandey-Pommier, R. Pizzo, A. G. Polatidis, W. Reich, H. J. A. Röttgering, J. Sluman, O. Smirnov, B. Stappers, M. Steinmetz, M. Tagger, Y. Tang, C. Tasse, S. ter Veen, R. Vermeulen, R. J. van Weeren, M. Wise, O. Wucknitz and P. Zarka, "Initial deep LOFAR observations of epoch of reionization windows. I. The north celestial pole", A&A**550**, A136 (2013).

Zahn, O., A. Lidz, M. McQuinn, S. Dutta, L. Hernquist, M. Zaldarriaga and S. R. Furlanetto, "Simulations and Analytic Calculations of Bubble Growth during Hydrogen Reionization", ApJ**654**, 12–26 (2007).

Zheng, H., M. Tegmark, V. Buza, J. S. Dillon, H. Gharibyan, J. Hickish, E. Kunz, A. Liu, J. Losh, A. Lutomirski, S. Morrison, S. Narayanan, A. Perko, D. Rosner, N. Sanchez, K. Schutz, S. M. Tribiano, M. Valdez, H. Yang, K. Z. Adami, I. Zelko, K. Zheng, R. P. Armstrong, R. F. Bradley, M. R. Dexter, A. Ewall-Wice, A. Magro, M. Matejek, E. Morgan, A. R. Neben, Q. Pan, R. F. Penna, C. M. Peterson, M. Su, J. Villasenor, C. L. Williams and Y. Zhu, "MITEoR: a scalable interferometer for precision 21 cm cosmology", MNRAS**445**, 1084–1103 (2014).

APPENDIX A

CMB ANALYSIS TOOLS

With the widespread analysis and understanding of the CMB, we must have a convention for the analysis and presentation. This convention can be understood by first considering the definition of Stokes Parameters.

An electromagnetic wave can be characterized in terms of a the time dependent electric field strength in the plane perpendicular to the direction of propagation as:

$$\begin{aligned}
E_x &= E_{x0}(t) \cos{(\omega_0 t + \phi_x)} \\
E_y &= E_{y0}(t) \cos{(\omega_0 t + \phi_y)}
\end{aligned} \tag{A.1}$$

Using this parametrization, the Stokes Parameters I,Q,U, and V can be constructed by taking the following combinations:

$$\begin{aligned}
I &= \langle E_{x0} \rangle^2 + \langle E_{y0} \rangle^2 \\
Q &= \langle E_{x0} \rangle^2 - \langle E_{y0} \rangle^2 \\
U &= 2 \langle E_{x0} E_{y0} \rangle \cos{(\phi_x - \phi_y)} \\
V &= 2 \langle E_{x0} E_{y0} \rangle \sin{(\phi_x - \phi_y)}
\end{aligned} \tag{A.2}$$

Where brackets represent a time averaged quantity. The parameter I represents the intensity of the wave, or for a perfect blackbody, the temperature. Stokes parameters Q and U represent states of linear polarization, while V is the circular component of polarization(Kosowsky, 1999).

The intensity field (Θ), and polarized components (Q and U) of the cmb, are often described by their scalar spherical harmonic decompositions:

$$\begin{aligned}
\Theta_{\ell m} &= \int d\Omega \ \Theta(\hat{\mathbf{n}}) Y_{\ell m}^*(\hat{\mathbf{n}}) \\
Q_{\ell m} &= \int d\Omega \ Q(\hat{\mathbf{n}}) Y_{\ell m}^*(\hat{\mathbf{n}}) \\
U_{\ell m} &= \int d\Omega \ U(\hat{\mathbf{n}}) Y_{\ell m}^*(\hat{\mathbf{n}})
\end{aligned} \tag{A.3}$$

where $\hat{\mathbf{n}}$ describes a position on the sky, projected onto a spherical surface and a superscript * represents the complex conjugation.

It is also convenient to define the spin 2 quantity ($Q + iU$) and the spin -2 quantity ($Q - iU$). Following the notation of Bunn $et\ al.$ (2003), these quantities are decomposed into spin-2 spherical harmonics:

$$Q + iU \quad = \sum_{\ell m} a_{2,\ell m} \ _2Y_{\ell m}(\hat{\mathbf{n}}) \tag{A.4}$$

$$Q - iU \quad = \sum_{\ell m} a_{-2,\ell m} \ _{-2}Y_{\ell m}(\hat{\mathbf{n}}) \tag{A.5}$$

From these spin ± 2 quantities, it is also possible to construct the scalar (E) and pseudo-scalar (B) fields as a basis of polarization. These fields can be constructed

from spin 0 spherical harmonics as:

$$a_{E,\ell m} = -(a_{2,\ell m} + a_{-2,\ell m})/2 \tag{A.6}$$

$$a_{B,\ell m} = 2i(a_{2,\ell m} - a_{-2,\ell m}))/2 \tag{A.7}$$

These E- and B- modes are also referred to as the "electric" and "magnetic" modes of polarization. The E-mode is a curl free field on the sphere, while the B-mode is a curl-only field on the sphere. It is also pertinent to note that the E-modes have a parity of $(-1)^{\ell}$, and B-modes have a parity of $(-1)^{\ell+1}$. In other words, under a parity transformation ($\hat{\mathbf{n}} \rightarrow -\hat{\mathbf{n}}$), E-modes remain unchanged for even multipoles while B-modes remain unchanged for odd multipoles (Hu and White, 1997a).

A powerful tool used to characterize and analyze the CMB is the power spectrum. This is the variance of the spherical harmonic coefficients:

$$\langle a_{\ell m} a^*_{\ell' m'} \rangle = \delta_{\ell \ell'} \delta_{mm'} C_\ell \tag{A.8}$$

The brackets above represent an ensemble average over an infinite number of independent observations. This is, naturally, impossible to achieve when observing a cosmologically pervasive signal. Assuming an independence of m-modes in a spherical multipole, Equation A.8 is estimated as:

$$\hat{C}_\ell = \frac{1}{2\ell + 1} \sum_{m=-\ell}^{\ell} a_{\ell,m} a^*_{\ell,m} \tag{A.9}$$

since there are only $2\ell + 1$ m-modes for each multipole, ℓ. The limitations of estimating a signal like the CMB can be written like a fractional uncertainty:

$$\frac{\Delta \hat{C}_\ell}{\hat{C}_\ell} = \sqrt{\frac{2}{2\ell + 1}} \tag{A.10}$$

This is referred to as cosmic variance, the inherent uncertainty in the power spectrum of the CMB due to our limited sample size.

It is also possible to create a cross-power spectrum or cross correlation between two spherically decomposed signals. This is achieved by replacing one of the spherical harmonic coefficients in Equation A.9 with that from another source. If there are two measurements of the CMB: map A with coefficients $a_{\ell m}$ and map B with coefficients $b_{\ell m}$ the cross power spectrum is defined as:

$$\hat{C}_\ell^{AB} = \frac{1}{2\ell + 1} \sum_{m=-\ell}^{\ell} Re\left\{ a_{\ell,m} b^*_{\ell,m} \right\} \tag{A.11}$$

where the superscript AB denotes the two maps from which the correlation is made. The real part is explicitly taken since spherical harmonics are in general complex and power must be real to be physical.

Propagating the uncertainty of this quantity is discussed in detail in Polenta *et al.* (2005). Here we present the general result for the uncertainty in a cross correlation for two maps, A and B, each with known noise power, N_ℓ^A and N_ℓ^B:

$$\Delta \hat{C}_\ell^{AB^2} = \sqrt{\frac{2}{2\ell + 1}} \left\{ \hat{C}_{\ell,th}^{AB2} + \frac{\hat{C}_{\ell,th}^{AB}}{2} \left(N_\ell^A + N_\ell^B \right) + \frac{N_\ell^A N_\ell^B}{2} \right\} \tag{A.12}$$

Here subscript *th* represents the theoretical or ideal (noiseless) correlation between two maps.

APPENDIX B

FARADAY ROTATION AND THE CMB

Here we express the mathematical formalism of E-B correlation in CMB power spectra as a result of Faraday Rotation.

Faraday Rotation results in the convolution in Fourier space of α_{RM} and the E- and B- mode spherical harmonics $E_{\ell m}, B_{\ell m}$.

This convolution is facilitated by Wigner-3j symbols The changes to the CMB power spectra take the following form under the small angle approximation:

$$E_{\ell m} = E_{\ell m,0} + \delta E_{\ell m} \tag{B.1}$$
$$B_{\ell m} = B_{\ell m,0} + \delta B_{\ell m} \tag{B.2}$$

where $E_{\ell'm',0}$ and $B_{\ell m,0}$ are the E and B-modes at the surface of last scattering. Note that in standard cosmological models, $B_{\ell m,0} \to 0$. Under the assumption the only E-modes are created during the early universe, the changes in the E- and B-mode power spectra are calculated in Gluscevic *et al.* (2009) as:

$$\delta B_{lm} = 2 \sum_{LM} \sum_{l'm'} \alpha_{LM} E_{l'm',0} \zeta^{LM}_{lml'm'} H^L_{ll'} \tag{B.3}$$
$$\delta E_{lm} = 2i \sum_{LM} \sum_{l'm'} \alpha_{LM} E_{l'm',0} \zeta^{LM}_{lml'm'} H^L_{ll'} \tag{B.4}$$

where $\zeta^{LM}_{lml'm'}$ and $H^L_{ll'}$ are defined in terms of the Wigner 3-j symbol as:

$$\zeta^{LM}_{lml'm'} \equiv (-1)^m \sqrt{\frac{(2l+1)(2L+1)(2l'+1)}{4\pi}} \times \begin{pmatrix} l & L & l' \\ -m & M & m' \end{pmatrix} \tag{B.5}$$

and

$$H^L_{ll'} \equiv \begin{pmatrix} l & L & l' \\ 2 & 0 & -2 \end{pmatrix} \tag{B.6}$$

The only non-zero sum terms being those satisfying $l + l' + L = $ even for B-modes and the only non-zero sum terms for E-modes are those satisfying $l + l' + L = $ odd.

It is possible to extend this work to include contributions where $B_{\ell m,0} \neq 0$ or for general $Q_{\ell m}$ and $U_{\ell m}$. We may investigate this possibility in future research since contributions to B-mode power from gravitational lensing, Synchrotron emission and primordial and astrophysical gravitational waves would result in non-zero $B_{\ell m,0}$.

APPENDIX C

REIONIZATION TERMINOLOGY

Here we provide a brief definition of terms important to reionization and the 21cm line. For a full list of terms, and their origin refer to Furlanetto *et al.* (2006)

Term	Definition
A_ν	Beam Response of two interferometric antennae
T_S	Spin temperature of hydrogen
T_{CMB}	Temperature of the CMB
T_b	Brightness temperature
δT_b	Differential Brightness temperature
T_α	color temperature of Lyα
k_B	The Boltzmann constant
δ	fractional matter over density
$v_\parallel$	peculiar velocity along the line of sight
t_γ	The Compton cooling time
σ_T	The Thompson Scattering cross-section
f_{HE}	Fraction of Helium
$\delta\mathrm{T}_b$	Differential brightness temperature
x_α	coupling constant of Lyα to hydrogen
x_c	collision coupling constant
x_{HI}	Fraction of neutral hydrogen
$\bar{x}_{HI}$	Globally averaged neutral fraction
x_i	Fraction of ionized of hydrogen
$\bar{x}_i$	Globally averaged ionized fraction
z_r	redshift of reionization
f_{esc}	escape fraction of ionizing photons
ζ	ionizing efficiency parameter
T_{sys}	system temperature of a radio telescope

Table 7: List and description of important HI intensity mapping and 21cm terms

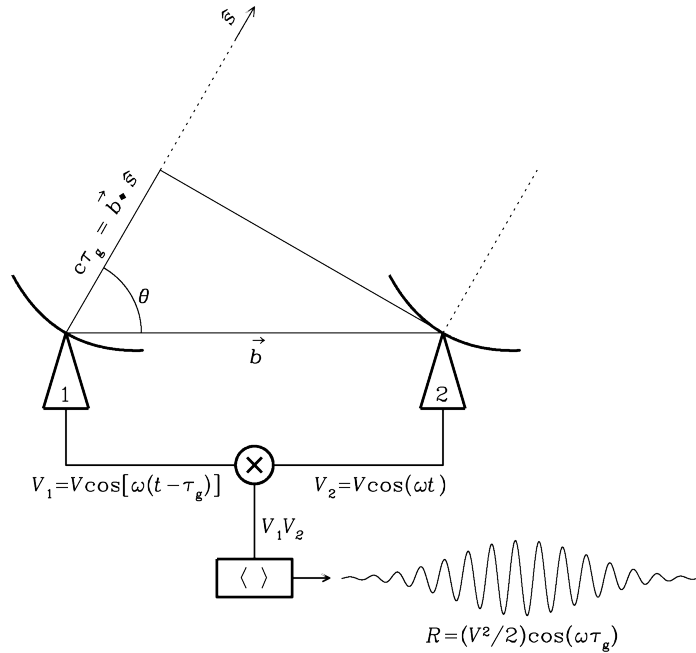APPENDIX D

RADIO INTERFEROMETRY BASICS

Figure 37: A graphical illustration of how a radio interferometer observes the sky. Two antenna are separated by a displacement vector $\overrightarrow{\mathbf{b}}$ called the baseline (for ease use of bold face will be used to indicate a vector instead of the arrow). Imagine a source located at the position on the sky denoted by the unit vector $\hat{\mathbf{s}}$. The radiation received from this source will have a delay between the two antennae: $c\tau = \mathbf{b} \cdot \hat{\mathbf{s}}$. The voltages of the two antennae are multiplied along with a correction for the phase difference and form complex visibilities. Image adapted from http: //www.cv.nrao.edu/~sransom/web/Ch3.html

The use of radio interferometers has become quite common in the search for the fluctuations of the 21cm brightness temperature from the EoR.

To briefly review how an interferometer observers the sky, consult Figure 37. Two antennae separated by a displacement vector $\mathbf{b}$ will observe the radiation from a source located at $\hat{\mathbf{s}}$ with a delay denoted by $c\tau = \mathbf{b} \cdot \hat{\mathbf{s}}$. Baselines are formed from each set of antenna in an array and are generally measured in units wavelengths for each frequency observed by the array. The components of $\mathbf{b}$ are referred to as (u, v, w). Each unique baseline observes a unique Fourier mode, k, on the on the sky whose

149

characteristic size is inversely proportional to the length of the baseline b (e.g. shorter baselines observer large spatial scales while long baselines observe small spatial scales).

This can be inferred from writing down the form of the complex visibility V_{ij} between antenna i and antenna j

$$V_{ij}(\nu) = \int I(\Omega, \nu) A_i(\Omega, \nu) A_j(\Omega, \nu) e^{-2\pi i \frac{\nu}{c} \mathbf{b} \cdot \hat{\mathbf{s}}} d\Omega \qquad \text{(D.1)}$$

where ν is the frequency of the observation, I is the inherent sky flux, A_i is the electromagnetic response pattern of antenna i and the integral is taken over the surface of the observed sphere Ω. This antenna response patterns are often combined to form a single per baseline response A, both forms of this equation are identical.

While not strictly a Fourier Transform, Equation D.1 takes the form of one over the surface of the sphere observed by a baseline. This assumption strengthens in the flat-sky approximation where $w \to 0$ and the observed sky area is small.

APPENDIX E

21CM ANALYSIS TOOLS

To understand the the power spectrum of δT_b, we need to develop the mathematical background necessary for this kind of analysis. An alternate definition to the visibility equation (Equation D.1) can be defined as follows.

Interferometric Arrays perceive the flux on the sky at the observed frequency ν, as the visibility between two antennae which form a baseline ($\mathbf{B} = \lambda(u\hat{\mathbf{i}}_0, v\hat{\mathbf{j}}_0, w\hat{\mathbf{n}}')$):

$$V_{\mathbf{B}}(\hat{\mathbf{n}}, \nu) = \frac{2k_B}{\lambda^2} \int d\Omega \; \delta T_b(\hat{\mathbf{n}}', \nu) A_\nu(\hat{\mathbf{n}}, \hat{\mathbf{n}}') e^{2\pi i \hat{\mathbf{n}}' \cdot \mathbf{B}/\lambda} \tag{E.1}$$

where $A_\nu(\hat{\mathbf{n}}, \hat{\mathbf{n}}')$ is the interferometric beam response of the antennae pair at a position on the sky $\hat{\mathbf{n}}$, whose primary beam points at $\hat{\mathbf{n}}'$. For a drift scan telescope, $\hat{\mathbf{n}}'$ can be replaced by time (or Local Sidereal Time) t which describes how the Sky above a telescope varies over the course of a night.

By defining the baseline such that the w component aligns in the direction of the center of the sky in the beam, it is possible to redefine this component of the baseline to a contribute solely to phase on the visibility.

Taking the Fourier transform over frequency, define the visibilities in Fourier and delay space, we write the visibility for a given baseline 'b': $\tilde{V}_b(\mathbf{u}, \eta)$. We note the (u, v, η) coordinate system is an interferometric Fourier space related to cosmological Fourier space as show in Parsons *et al.* (2016).

The cross power spectrum of δT_b between two identical baselines a and b is then:

$$P(\mathbf{k}) = \left(\frac{\lambda^2}{2k_B}\right) \frac{X^2 Y}{\Omega_{a,b} B} \langle \tilde{V}_a(\mathbf{k}) \tilde{V}_b^*(\mathbf{k}) \rangle \tag{E.2}$$

in units of $(mK)^2 (hMpc^{-1})^{-3}$. Here the ensemble average is over independent measurements of the δT_b (temporal, spatial, etc), the $X^2 Y$ factor converts (u, v, η) to Fourier k modes, B is the bandwidth of the array and $\Omega_{a,b}$ is a beam-power normalization constant.

Since the Fourier k modes for a given baseline b, at an observed wavelength λ, probe the spatial structure projected onto the sky-plane, Equation E.2 can be used to compute the 1-Dimensional power spectrum when the visibilities are binned in annuli of $|k|$.

It is also convenient to define the volume weighted power spectrum:

$$\Delta^2(k) = \frac{k^3}{2\pi} P(\mathbf{k}) \tag{E.3}$$

which has units of $(mK)^2$.

The error on these quantities has been explicitly dropped. Uncertainties in $P(\mathbf{k})$ can be estimated from the Fischer information matrix between constructed between different Fourier k bins as discussed in Furlanetto *et al.* (2006) and propagated into an uncertainty in Δ^2.

For a given set of parameters, Ψ, the (i, j)th component Fischer information matrix can be computed:

$$F_{ij} = tr \left[\mathbf{C}^{-1} \frac{\delta \mathbf{C}}{\delta \Psi_i} \mathbf{C}^{-1} \frac{\delta \mathbf{C}}{\delta \Psi_j} \right] \tag{E.4}$$

where $\mathbf{C}$ is the covariance matrix which describes the covariance of the data from thermal noise, signal variance, residual foreground and any remaining systematic effects.

The parameter vector Ψ could contain quantities such as the binned power spectrum estimates or even parameters in a theoretical model.

APPENDIX F

OPTIMAL QUADRATIC ESTIMATION: A REVIEW

Ideally the 21cm power spectrum (P_{21}) is defined:

$$\left\langle \tilde{T}_b(\mathbf{k})\tilde{T}_b^\star(\mathbf{k}') \right\rangle = (2\pi)^3\, \delta(\mathbf{k} - \mathbf{k}')P_{21}(\mathbf{k}) \tag{F.1}$$

where brackets denote ensemble averages, $\tilde{T}_b(\mathbf{k})$ is the Fourier transform of the 21cm brightness temperature and δ is the Dirac delta function. As described in A15 and C18, the quadratic estimation of this power spectrum begins with the un-normalized bandpowers in the α-th k-bin:

$$\begin{aligned}\hat{q}_\alpha &= \frac{1}{2}\left(\mathbf{R}_1\mathbf{x}_1\right)^\dagger \mathbf{Q}_\alpha \left(\mathbf{R}_2\mathbf{x}_2\right) \\ &= \frac{1}{2}\mathbf{x}_1\mathbf{R}_1\mathbf{Q}_\alpha\mathbf{R}_2\mathbf{x}_2\end{aligned} \tag{F.2}$$

the subscripts 1 and 2 denote independent sky measurements (e.g. odd and even Julian Dates), $\mathbf{R}_i$ is an arbitrarily chosen weighing matrix for data vector i (C18 chooses $\mathbf{R} = (\mathbf{C} + \alpha\mathrm{Tr}[\mathbf{C}]\mathbf{I})^{-1}$), and $\mathbf{Q}_\alpha$ is a matrix operator which performs the Fourier transform and bins the data into the α-th k-bin. $\mathbf{Q}_\alpha$ can formally be evaluated as $\mathbf{Q}_\alpha \equiv \frac{\delta\mathbf{C}}{\delta p_\alpha}$ or the derivative of the covariance with respect to the true bandpower in the k-bin.

The set of $\hat{q}_\alpha$ can be related to the properly normalized power spectrum estimates by a normalization matrix[20], $\mathbf{M}$.

$$\hat{\mathbf{p}} = \mathbf{M}\hat{\mathbf{q}} \tag{F.3}$$

The normalized bandpowers form our estimate of $P_{21}(\mathbf{k})$ are related to the true power spectrum $\mathbf{p}$ via a windowing matrix, $\mathbf{W}$.

---

[20]In Liu and Tegmark (2011) and Liu *et al.* (2014b) Equation F.2 is instead written as the normalized power ($\hat{p}_\alpha$) and relies on the estimation matrix $\mathbf{E}_\alpha$. We can relate the matrices $\mathbf{E}_\alpha = M_\alpha\mathbf{Q}_\alpha$ to compute the bandpowers directly.

$$\hat{\mathbf{p}} = \mathbf{W}\mathbf{p} \qquad\qquad (\text{F.4})$$

In other words, the normalized power spectrum probes a linear combination of the true power spectrum estimates in each k-bin. To compute the normalization matrix, **M**. Liu *et al.* (2014b) shows that:

$$\mathbf{W} = \mathbf{M}\mathbf{F} \qquad\qquad (\text{F.5})$$

where **F** is the Fischer information matrix and can be computed given the weighting matrix **R**:

$$\mathbf{F}_{\alpha\beta} = \frac{1}{2}\left[\mathbf{R}_1\mathbf{Q}_\alpha\mathbf{R}_2\mathbf{Q}_\beta\right] \qquad\qquad (\text{F.6})$$

In this analysis we employ the use of $\mathbf{R} = (\mathbf{C} + \alpha\mathrm{Tr}[\mathbf{C}]\mathbf{I})^{-1}$, also used in C18. We also choosing a normalization matrix $\mathbf{M} = \mathbf{I}$ and normalize the window matrix **W** so that the rows sum to one (this ensures the windowing conserves the power in **p**).